Source Apportionment of Black Carbon and PM_{10} Aerosol Using Optical Properties, Chemical Tracers and Statistical Tools

Dissertation submitted by

Saryu Garg

in partial fulfilment of
the requirements for the degree of

Doctor of Philosophy

Department of Earth and Environmental Sciences

Indian Institute of Science Education and Research (IISER) Mohali

August 2017

Declaration

I hereby declare that the work presented in this dissertation has been carried out by me, under the supervision of Dr. Baerbel Sinha, of the Department of Earth and Environmental Sciences, IISER Mohali. No unauthorized external assistance has been sought for the work contained in this thesis and all sources used, have been acknowledged as per bibliographical rules. Due acknowledgement of collaborative work and discussions has also been made. This work has not been submitted in part or full, for a degree, diploma or a fellowship, to any other university or institute. In carrying out this research, I have complied with the rules of standard scientific practice as formulated in the statutes of Indian Institute of Science Education and Reseach, Mohali.

Date:
Place: Mohali

Saryu Garg

In my capacity as the supervisor of the candidate's thesis work, I certify that the above statements by the candidate are true to the best of my knowledge.

Date:
Place: Mohali

Dr. Baerbel Sinha
(Supervisor)

Acknowledgements

First and foremost, I want to thank my PhD advisor, Dr. Baerbel Sinha for her valuable guidance, her constant support and encouragement, and for being a source of inspiration to work harder and to adapt good work and research ethics.

I want to extend gratitude to Dr. Vinayak Sinha, who has always provided valuable inputs and motivation, and has constantly guided me throughout my PhD degree. I also want to thank Dr. Abhishek Chaudhuri, for providing useful feedback and for his encouraging words.

I duly acknowledge the efforts of Mr. Inderjit Singh to train me in working with the Scanning Electron Microscope. I thank Dr. J S Bilgha for sharing with me, his prized knowledge about flora of IISER Mohali and elsewhere, and for his support and encouragement.

I also wish to thank all the fellow co-authors on my publications, and the anonymous reviewers who helped to bring the best out of my research works.

I thank Atmospheric Chemistry Facility of IISER Mohali, for making sophisticated, state- of- art measurement and analytical tools available, that allowed me to get hands- on training on working with different equipment and to get acquainted with the technical aspects, both of which are important for holistic training to carry out research in the field of Atmospheric Sciences. I also thank IISER Mohali for the Scanning Electron Microscopy (SEM) facility.

I acknowledge the Department of Earth and Environmental Sciences at IISER Mohali for well-designed coursework and setup. I also want to thank the Founding Director of IISER Mohali, Dr. N. Sathyamurthy, and the institute, IISER Mohali, for good infrastructure and administrative system, that helps one to carry out research work efficiently. I also thank the institute for providing me Junior and Senior Research Fellowships (JRF, SRF) and for providing me the opportunity to present my work in international science conferences.

I really want to thank all my colleagues, friends and members of Aerosol Research Group and Atmospheric Chemistry and Emissions Research Group- Vinod, Praphulla, Harshita, Chinmoy, Savita, Gaurav, Haseeb, Ashish, Pallavi, Tess, Abhishek, Vaishali, Nimya, Ebin, Shabin, for always extending timely help, for maintaining a healthy work environment, and for working more as a team than as competitors.

Finally, I want to thank my husband, Abhijeet Kaplish, for having faith in me, more than I have in myself, and for guiding me throughout. I really want to thank my parents, and my family for being encouraging, for having faith in my decisions, and for providing me the best atmosphere all through my life, that helped me become a reasonably good, happy and productive person. I want to thank my new family, my parents- in- law for being extremely helpful, understanding, and caring. I also thank all my friends, Tanya, Priya, Shriya, Shivani, for always being there! At last, I want to thank Nature for always treating me well and for maintaining a healthy balance in my life, while allowing me to enjoy the most important and valuable bounties of life.

Saryu Garg

List of Publications

1. **Garg S.**, Chandra B. P., Sinha V., Sarda-Esteve R., Gros V., and Sinha B.: Limitation of the Use of the Absorption Angstrom Exponent for Source Apportionment of Equivalent Black Carbon: a Case Study from the North West Indo-Gangetic Plain, Environmental Science and Technology, 50(2), 814–824, 2016.
2. **Garg S.**, Sinha B.: Determining the contribution of long-range transport, regional and local sources areas, to PM_{10} mass loading in Hessen, Germany using a novel multi-receptor based statistical approach, accepted for publication in Atmospheric Environment.
3. Pawar H., **Garg S.**, Kumar V., Sachan H., Arya R., Sarkar C., Chandra B., P. and Sinha B., Quantifying the contribution of long-range transport to Particulate Matter (PM) mass loadings at a suburban site in the North-Western Indo Gangetic Plain (IGP), Atmos. Chem. Phys., 15, 9501-9520, 2015.
4. Nandy B., Sharma G., **Garg S.**, Kumari S., George T., Sunanda Y., Sinha B.: Recovery of consumer waste in India – A mass flow analysis for paper, plastic and glass and the contribution of households and the informal sector, Resources, Conservation and Recycling, 101, 167–181, 2015.

Synopsis

Chapter 1: Introduction

Tropospheric aerosols are ubiquitous in the natural environment and play an important role in the hydrological cycle of Earth, while also affecting human health, local and global climate, and air quality. The first chapter of my thesis discusses the physical and chemical properties of aerosol particles, their role in the atmosphere, their effects on the non- living and living environment, and the atmospheric lifetimes of varied aerosol particles. Aerosols comprise of solid or liquid particles with negligible terminal fall speed, suspended in a carrier gas, which is the atmospheric air. Aerosol particles exist in a variety of shapes, sizes, with different physico-chemical properties, and originate from a variety of sources. They can be emitted from natural sources or human-influenced activities. Despite being present everywhere and being emitted from a vast number of sources, aerosol particles are termed as trace components of the atmosphere. Aerosol particles are necessary for the formation of clouds and thus, precipitation is impossible without their existence. They have complex relationship and interaction with clouds and the hydrological cycle, which directly depends on the size, the physical properties, number and the chemical properties of the particles present. However, aerosols also have the ability to enter the human body and cause disorder in the normal functioning of the cardio- vascular and pulmonary systems of the body. The concentration of aerosol particles in the air is a major determinant of its quality, and as a consequence, significant efforts are made to mitigate their number and mass concentration density in the atmosphere. Thus, research on various aspects of aerosol particles, including their sources, is an integral and important part of atmospheric sciences.

This chapter also discusses the concept of source- apportionment and the advantages and limitations of different source apportionment techniques that are commonly employed. Various methods of source-apportionment based on chemical analysis, computer simulation of wind transport dynamics and modelling of source- receptor relationships have been developed for identification of sources of aerosol particles and sometimes, also the quantification of the contribution of these sources to aerosol loadings. For development of targeted mitigation strategies, it is crucial that the potential sources and their relative strengths are determined and reported. Since aerosol particles have a multitude of different properties, certain source-apportionment techniques may not be applicable to all the aerosol particle types. For example, chemical analysis of secondary particles such as ammonium sulphate may not allow to trace the

source of the gas-phase precursors ammonia and sulphur dioxide, while isotopic techniques may be able to do so. The techniques developed for source-apportionment take time to evolve, so the results obtained from their application must be considered with caution. Often these results may be misleading, either due to application of the tools without feasibility studies within the specific local study environment or because of limitations of the tool itself. In my thesis, I test the validity and effectiveness of the application of various source- apportionment techniques, and develop a novel method for quantifying the contribution of long- range transport, and regional and local sources of PM_{10} to the aerosol loading at receptor sites. Subsequently, I apply the same to quantify their contribution at multiple receptor locations in Hessen, Germany.

Chapter 1 concludes with stating the motivation of writing this thesis and listing the questions that I have aimed to address in the thesis:

1) Can absorption angstrom exponent (α_{abs}) be used as a generic tracer for biomass burning related black carbon (BC) emissions in a complex emission environment?
2) How does α_{abs} of BC vary for different types of biomass burning sources in a complex environment?
3) What factors determine the value of α_{abs}?
4) What are the percentage contributions of long- range, regional and local sources to the total PM_{10} measured over the region of Hessen, Germany as determined by the new source apportionment models I developed in my thesis, namely, - MuSAM (Multi- receptor Source Apportionment Model) and MuReSAM (Multi- receptor Regional Source Apportionment Model)?
5) What was the effect of closing down and then subsequent repair and re-opening of a major highway (Schiersteiner Brücke) on the local PM_{10} loading?

Chapter 2: Quantitative measurement of aerosol properties and mass

Measurement of mass, size or any other property of atmospheric aerosol particles, poses several analytical challenges. These arise due to the vast heterogeneity in terms of the size, origin, composition, optical properties, and chemical and physical properties of aerosol particles. High sensitivity of the mass, size, physical dynamics and optical properties of most type of particles, to the relative humidity of the environment adds to the list of analytical challenges. Using one and the same technique and/or instrument for measuring all types of aerosol particles across the full size range is not possible and comparing results obtained by different instruments based on different physical properties in the size range where their detection capabilities overlap poses many analytical difficulties. The most fundamental property of atmospheric aerosol particles- their size, itself cannot be measured directly in real time for the full size range owing to the very small size

of the particles (typically < 100 μm) and the vast size range (5-6 orders of magnitude). Choice of a measurement technique depends on the requirement and the intended application, and users often modify existing/commercially available instruments to suit their requirements. In this chapter, I discuss the different analytical instruments like SEM (Scanning Electron Microscope), AMS (Aerosol Mass Spectrometer), Aethalometer, PM (Particulate Matter) mass analyser, OPC (Optical Particle Counter), DMA (Differential Mobility Analyser), etc., that are commonly used for measurement of aerosol mass or number concentration, particle size, optical properties, aerosol number, chemical composition, or morphology of various types of aerosol particles, and the advantages and drawbacks of the application of these instruments/ techniques. The functioning of instruments that are part of the Aerosol measurement facilities at IISER Mohali is explained in detail. PM_{10} and $PM_{2.5}$ mass analysers measure based on the technique of beta- attenuation due to absorption of beta particles by aerosol particles collected on a sampling tape. Aethalometer- an instrument that measures the mass concentration of equivalent BC (Black carbon), uses the optical attenuation due to light absorption by particles as a measurement principle. The SEM (Scanning Electron Microscope) integrated with EDS (Energy- Dispersive X-ray Spectroscopy) have been described in technical detail and provides detailed images of individual particles across the full size range after off-line sampling, as well as the chemical composition of large, electron beam-stable inorganic particles. Nuances of operating and maintaining these instruments in the environment of Mohali have also been stated, including the site- specific procedure for the correction of data from Aethalometer. Later, the basis of the development and application of the new source- apportionment techniques developed by me have been described. The new techniques are compared to different previously used statistical techniques, and spatial analysis tools.

Chapter 3: Limitation of the Use of the Absorption Angstrom Exponent for Source Apportionment of Equivalent Black Carbon: A case study from the North West Indo-Gangetic Plain

In this chapter, the commonly used source- apportionment technique of using absorption angstrom exponent (α_{abs}) for source- apportionment of black carbon has been tested. Angstrom exponent measurements of equivalent black carbon (BC_{eq}) have recently been introduced as a novel tool to apportion the contribution of biomass burning sources to the BC_{eq} mass. The BC_{eq} (equivalent mass) is the mass of ideal BC with defined optical properties, that, upon deposition on the aethalometer filter tape, would cause equal optical attenuation of light at a given wavelength, to the actual $PM_{2.5}$ aerosol deposited. The BC_{eq} mass, hence, is identical to the mass of the total light absorbing carbon (LAC) deposited on the filter tape (LAC= BC_{eq}). The technique called two-component aethalometer model has been applied to measurements made in Atmospheric

Chemistry Facility (a sub-urban site) of IISER Mohali, Punjab, and subsequently, the validity of the use of angstrom exponent (α_{abs}) for source- apportionment of black carbon in more complex environments has been verified. In this study, the variation of angstrom exponent (α_{abs}) values of BC from different sources is also determined. Simultaneously collected high time resolution data from a 7-wavelength aethalometer (AE 42, Magee Scientific, USA) and a high sensitivity Proton Transfer Reaction- Quadrupole Mass Spectrometer (PTR-MS) installed at the facility, was employed to identify a number of biomass combustion plumes during which BC_{eq} (black carbon) enhancements correlated strongly with an increase in acetonitrile mixing ratio. The identified types of biomass combustion include two different types of crop residue burning (paddy and wheat), burning of leaf-litter, and garbage burning. Traffic (fossil-fuel burning) plumes were also selected for comparison. Since the α_{abs} values did not behave as expected, the real factors that decide the value of α_{abs} have been explored. It has been observed that the combustion efficiency, rather than the fuel used, determines $\alpha_{abs,}$ and consequently, the α_{abs} can be ~1 for flaming biomass combustion and >1 for older vehicles that operate with poorly optimized engines. In this chapter, I conclude that the absorption angstrom exponent is not representative of the fuel used and therefore, cannot be used as a generic tracer to constrain source contributions. The study presented here is the first to combine real- time measurements of gas- phase VOC combustion tracers with BC measurements for specific identification of ambient combustion plumes, and the first to use high- time- resolution observations of biomass burning tracers to identify biomass burning events. It is also the first study to highlight the limitation of using two- component aethalometer model for source- apportionment of BC, thus warning about the erroneous conclusions that may be reached by incorrect application of the model.

Chapter 4: Determining the contribution of long-range transport, regional and local source areas, to PM_{10} mass loading in Hessen, Germany using a novel multi-receptor based statistical approach

This chapter deals with the development and application of two statistical source- apportionment models- MuSAM and MuReSAM, which produce graphical output in the form of gridded geographical maps, and help to quantify the contribution of long- range, regional and local source areas of PM_{10} (and other pollutant species) by the use of reverse- modelling technique. CWA (Concentration Weighted Average) values for each cell of the grid have been calculated by using in-situ measured wind and concentration data from multiple receptor sites, and back- trajectories of air masses that reach the receptor sites within a specific time period. Selection of receptor sites is different at the different scales of long- range transport, regional transport and local transport of particulate matter through wind. In a case study presented in this chapter, the two newly developed

models- MuSAM and MuReSAM have been used to perform quantitative statistical source apportionment of PM_{10} at receptor sites in South Hessen, Germany. On average, between 7.8 and 9.1 µg/m3 of PM_{10} (~50%) at receptor sites in South Hessen is contributed by long-range transport. The dominant source regions are Eastern, South Eastern, and Southern Europe. 32% of the PM_{10} at receptor sites in South Hessen is contributed by sources within the region (2.8- 9.41 µg/m3). This fraction varies from <20% at remote sites to >40% for urban stations. Local sources within 2 km of the receptor site are responsible for 7% to 20% of the total PM_{10} mass (0.7- 4.4 µg/m3). The study presented in this chapter points to the limitations of source- apportionment techniques that try to attribute all of the measured concentration of pollutant species to long range transport (which traditional CWT or PSCF models do) or all of it to the regional sources. Input data must be carefully selected and remote sites must be used to evaluate the contribution of long range transport to a region. Sites heavily impacted by local or regional sources may wrongly blame distant sources for local pollution. While evaluating the contribution of regional sources, a long-range transport correction must be performed. The MuSAM and MuReSAM model have subsequently been used to perform a study on the perturbation of the traffic flow due to the closing and reopening of a major highway, the Schiersteiner Brücke. Compared to when the bridge was closed, the contribution of the bridge to PM_{10} mass loadings at the receptor sites- Wiesbaden Süd and Raunheim, increased by approximately 120% after it reopened and became a bottleneck, obstructing traffic flow; however, in absolute terms the increase in the PM_{10} contributed by this source to the receptor sites amounted to ~0.5 µg/m3 and <0.1 µg/m3, respectively. This study presents the working of a newly- developed integrated modelling approach for source-apportionment at long- range transport and regional scale. It is the first study that uses real- time ambient data from multiple receptor sites, for quantitative statistical source apportionment of PM_{10} to both, distant and regional sources.

Chapter 5: Conclusions: Major findings and Outlook

In the final chapter, I present the major conclusions from the studies compiled in this thesis. I highlight the importance of source- apportionment for identification and quantification of source contributions to aerosol mass loadings in the atmosphere and the importance of using source-apportionment techniques customised for the environment of the study region. Giving due consideration to the underlying assumptions of the technique in view of the area of application, is an important pre- requisite for effective source-apportionment. Extrapolation of the application area without due consideration of potential artefacts due to local conditions must be avoided for all source- apportionment methods, else erroneous results are likely to be produced. Limitations of a technique should also necessarily be explored by the developer, along with its advantages, for

the prevention of misinterpretation of the results. This is crucial to provide accurate information to policy makers who need to know the role of transported versus local pollution sources for smart and focused practical mitigation efforts.

Contents

Chapter 1

Introduction

1.1 The Atmosphere

The atmosphere of Earth is composed of 78% Nitrogen, 21% Oxygen, 1% Argon, water vapor 0.0001%- 5% (Salby, 1995; Wallace and Hobbs, 2006), various solid and/or liquid particles, and numerous other gases in trace amounts, the sources of which can be traced to geologic, biological, chemical, and anthropogenic processes (Seinfeld and Pandis, 2006). Earth's atmosphere extends from the surface of the Earth to an altitude of >100 km (Jacob, 1999) and is characterized by decrease in atmospheric pressure with height and by heterogeneity in the chemical and physical properties, with respect to height. The atmosphere is stratified into layers, each having different air mass density, composition, temperature profile, and role: Depending on reversal of temperature gradient trends, the atmosphere is divided into four layers. The first layer- 'troposphere' extends from the surface to an altitude of 8-18 km (Jacob, 1999) and is characterized by having ~90% of all the air mass of the atmosphere and most of all the weather (Wallace and Hobbs, 2006), fairly homogeneous composition and high rate of vertical mixing, a decrease in temperature with altitude (lapse rate of ~6.5°C per km) (Salby, 1995), high rate of removal of aerosol particles due to deposition (dry and wet), and the strong subtropical jet streams (Finlayson-Pitts and Pitts Jr., 2000). The vertical extent of the troposphere is a function of latitude and season. Most of the emissions taking place due to activities on the surface and due to flying airplanes, end up becoming a part of the troposphere. The lowermost part of the troposphere, near the surface (upto 100 to 3000 m) is a unified layer called boundary layer, with some unique characteristics (Stull, 1988). The rest of the troposphere is called free troposphere. The boundary layer is directly influenced by and rapidly responds (within 1 hour) to frictional drag, evaporation, transpiration, heat transfer, pollutant emissions, and terrain induced flow modifications. It's thickness is variable in space and shows diurnal variation over the day (increasing in thickness with heating of the surface as the day progresses and decreasing at night as the surface cools). The boundary layer "breaks" early in the day when solar radiation reaches the surface, causing air from free troposphere to mix with the air near the surface of Earth. There is rapid and uniform mixing in this layer due to heat- induced turbulence near the surface of Earth. Most of the emissions that take place near the surface stay within the boundary layer and thus, the dynamics of this layer have high influence on all life on

Earth, including human beings. The troposphere ends in a region of no temperature gradient, which is called the tropopause.

The second layer, called 'stratosphere' extends from above the tropopause upto an altitude of ~50 km. The most remarkable feature of this layer is the presence of high amount of ozone (number density of 7 x 10^{12} molecules cm^{-3} in the lower stratosphere – 0.5 x 10^{12} molecules cm^{-3} in the upper part) (Jacob, 1999), popularly called the ozone layer. In this layer, temperature increases with altitude as absorption of solar radiation by ozone molecules causes heating. This layer is also characterized by weak vertical transport and mixing, extremely low water vapor content, limited rate of removal of particles due to loss processes, and domination of radiative processes. Plinian volcanic eruptions often result in injection of high concentrations of sulphate particles into stratosphere, which have a long lifetime due to lack of loss processes in the stratosphere. Oxidation of the long-lived carbonyl sulphide is the main source of natural stratospheric aerosol, which is made from aqueous sulfuric acid solution (Seinfeld and Pandis, 2006), although the anvil of pyrogenic clouds (Luderer et al., 2006) and the monsoon clouds at the foothills of the Himalayas can inject tropospheric gases and aerosols into the stratosphere (Randel et al., 2010).

99.9% of all the atmospheric mass is contained these first two layers. The stratosphere ends in stratopause, where the gradient in temperature ceases and the maximum temperature of the stratosphere (~2°C) is reached. The third layer 'mesosphere' extends above the stratosphere to an altitude of ~80 km and sees a decrease in temperature with height and high incidence of convective motions and radiative processes. Beyond the mesopause, lies the fourth layer- 'Ionosphere', which extends into outer space to ~500 km from Earth's surface and is marked by high temperatures. Due to photodissociation and photoionization processes in this layer due to interaction of atmospheric nitrogen and oxygen molecules with strong UV radiation, temperature increases with altitude.

In this Thesis, I limit the scope of my study of lower atmosphere, which constitutes stratosphere and primarily, the troposphere. Here is where most of the emissions from major sources happen and significantly impact the ecosphere and climate systems.

1.2 Aerosol particles in the Troposphere

In atmospheric sciences, aerosol particles are defined as a suspension of liquid or solid particles, with negligible terminal fall velocity, in a carrier gas. These solid or liquid particles are in permanent temperature and relative humidity dependent equilibrium with their carrier gas. In case of the atmosphere, most of the times this carrier gas is atmospheric air. Terminal fall velocity is defined as the velocity achieved by an aerosol particle when the gravitational force acting on the

particle moving in gas, equals the opposing drag force exerted on it by the carrier gas, resulting in negligible acceleration (Kulkarni et al., 2011). The fact that aerosol particles are in permanent temperature and relative humidity dependent equilibrium with the gas phase is particularly important while considering liquid particle, salts that undergo deliquescence at less than 100% RH and display hysteresis in efflorescence behavior and, semi volatile species such as ammonium nitrate and ammonium sulfate. The equilibrium constraint in combination with the constantly changing temperature, absolute and relative humidity of the carrier gas makes it extremely challenging to design reproducible, accurate and precise methods for determining the total aerosol burden and collecting artefact- free off-line samples for chemical analysis.

Aerosol particles are ubiquitous in the natural environment and aerosol particle sizes typically ranges from 1 nm to 100 μm (Kulkarni et al., 2011). Aerosols are an important component of the atmosphere, and the hydrological cycle by helping in the formation of clouds (Andreae, 2009; Gunthe et al., 2009; Ramanathan et al., 2001; Rosenfeld et al., 2014; Spracklen et al., 2008).

Aerosols may be emitted directly as particles (primary aerosol particles) or formed in the atmosphere by gas-to-particles conversion processes (secondary aerosol processes) (Seinfeld and Pandis, 2006). Primary aerosol particles usually result from the disintegration of liquid or solid agglomerates or from resuspension of particles (Friedlander, 2000). Examples of primary aerosol particles include sea salt from sea spray evaporation, suspended mineral dust, volcanic ash, pollen and other biogenic particles, soot and fly ash from combustion processes, etc. Secondary aerosol particles are formed from gaseous emissions in the atmosphere through gas- to- particle conversion mechanisms. Gases with low volatility (and thus, unstable) participate in such processes and result in the formation of ultra-fine particles (<100 nm diameter) via heterogeneous homomolecular or heteromolecular nucleation followed by condensational growth. Low volatility gases may be formed directly or through a chain of chemical reactions acting on high volatility gases (Junninen et al., 2014). Sometimes, existing particles may also grow due to gas adsorption (heterogeneous heteromolecular condensation) (Friedlander, 2000). The widely studied aerosol particle type- Secondary organic aerosols (SOA) are formed from organic precursors through gas-to-particle conversion processes, with biogenic VOCs precursors dominating over the anthropogenic VOCs (Moise et al., 2015).

Once in the atmosphere, all aerosol particles undergo “aging”, i.e., changes in their properties due to action of physical and chemical processes on them. Aging also results in blurring of the above mentioned categories as all primary particles age and acquire secondary coatings which are made up of the same constituents as secondary organic aerosol (SOA) and secondary inorganic aerosol (SIA).

Aerosol particles found in the troposphere can be of natural or anthropogenic origins. There is great spatial-temporal variability in characteristics of aerosol particles as a result of varied types of sources, the complexity of the formation processes of these particles, and the chemical and physical processes acting on the particles during their lifetime in the atmosphere (Kondratyev et al., 2006). Some aerosol particles are transported far and have atmospheric lifetimes of weeks to months (accumulation mode aerosol) while other are highly localized and have a short lifetime (coarse mode aerosol), resulting in a large spatial and temporal variability in their atmospheric concentrations. The gas phase and aqueous phase involved in modifying their surface properties too, are spatially heterogeneous, which makes it difficult to study aerosols ubiquitously and extrapolate their characteristics to places where, e.g. the aerosol aqueous phase has a different pH and consequently favors different chemical reactions.

Although the negative effects of aerosols on human health were highlighted by a prominent physician, Moses Maimonides in the 12th century, research in order to understand the importance and role of atmospheric particles in climate perturbation and on human health, picked up pace only in the early 90s of the 20th century (Xie et al., 2008). Till IPCC's Assessment Report 2 in 1995 (Anon, 1995), only one dimension of the role of atmospheric aerosol particles in perturbation of radiative forcing of Earth's, i.e., negative RF, had been explored. Since then, a lot of research continues to be done in order to study the properties and effects of these particles on climate and on human health. It was in 2001 when IPCC's Third Assessment Report (Penner et al., 2001) was published, that a possibility of positive radiative forcing by aerosol particles was highlighted and by the Fourth Assessment Report in 2007 (Solomon et al., 2007), positive radiative forcing due to black carbon had been established. Despite high intensity of aerosol emissions, aerosols are trace species in the atmosphere thanks to their short lifetime. Aerosol particles have a short lifetime of about few days to weeks, unlike most greenhouse gases and are termed as SLCP (Short- Lived Climate Pollutant). Thus, although, both- greenhouse gases and black carbon aerosol have the ability to cause global warming, control of black carbon emissions has the benefit of quick and effective mitigation to global warming, while control of acid aerosol precursor emissions (most notably SO_2 emissions) has severely amplified global warming in downwind regions (Shindell and Faluvegi, 2009).

1.2.1 Annual global budget and emissions:

With increase in anthropogenic activity, the amount of aerosol that gets emitted into the atmosphere has increased manifold. Emission of various types of aerosols varies with the environment- pristine environments are dominated by mineral dust, sea salt, or SOA from BVOC emissions whereas urban environments are dominated by combustion- generated aerosols and

suspended dust and other material. Latest reported emissions of aerosol particles in IPCC's Assessment Report 5 are provided in Table 1.1.

Aerosol	**Emissions (Tg yr^{-1})**
ANTHROPOGENIC	
Anthropogenic primary aerosol	
Biomass burning aerosol	29 - 85.3
Black Carbon	3.6 - 6.0
POA	6.3 - 15.3
Anthropogenic secondary aerosol precursors	
SO_2 (TgS)	43.3 - 77.9
NO_x (TgN)	37.5
NH_3 (TgN)	34.5 - 49.6
Anthropogenic NMVOCs	98.2 - 157.9
NATURAL	
Natural primary aerosol	
Sea spray including marine POA	1400 - 6800
Mineral dust	1000 - 4000
Terrestrial PBAPs including spores	50 - 1000
Secondary aerosol from natural precursors	
DMS (TgS yr^{-1})	10 - 40
NO_x (TgN)	11.3
NH_3 (TgN)	10.6
Monoterpenes (TgC yr^{-1})	30 - 120
Isoprene (TgC yr^{-1})	410 - 600
SOA production from all BVOCs	20 - 380

Table 1.1: Global anthropogenic and natural emissions of aerosols and aerosol precursors, obtained from available inventories. Table compiled from Table 7.1 (a) and (b) of Boucher et al (Clouds and Aerosols, in Climate Change 2013: The Physical Science Basis. Contribution of Working Group I to the Fifth Assessment Report of the Intergovernmental Panel on Climate Change, edited by T. F. Stocker, D. Qin, G.-K. Plattner, M. Tignor, S. K. Allen, J. Boschung, A. Nauels, Y. Xia, V. Bex, and P. M. Midgley, Cambridge University Press, Cambridge, United

Kingdom and New york, NY, USA., 2013) and Table 6.9 of Ciais et al (Carbon and Other Biogeochemical Cycles, in In: Climate Change 2013: The Physical Science Basis. Contribution of Working Group I to the Fifth Assessment Report of the Intergovernmental Panel on Climate Change, edited by T. F. Stocker, D. Qin, G.-K. Plattner, M. Tignor, S. K. Allen, J. Boschung, A. Nauels, Y. Xia, V. Bex, and P. M. Midgley, Cambridge University Press, Cambridge, United Kingdom and New york, NY, USA., 2013), with permission.

1.2.2 Atmospheric lifetimes of aerosol, transport and sinks:

Once aerosol particles enter the atmosphere, they are transported, and acted upon by their surrounding environment, that modifies them physically and chemically (aging). These particles are transported with air over scales as large as intercontinental and global (Wallace and Hobbs, 2006). With time, small particles get converted to larger particles through coagulation. During their air transport, particles get coated with other aerosol which makes them more prone to becoming CCN (Harris et al., 2013; Henning et al., 2014). Atmospheric lifetime of aerosol particles is mainly controlled by wet deposition (incorporation of particles in cloud droplets and rain) and dry deposition (under the influence of gravitational force). Thus, their atmospheric lifetimes are fairly short: few days to few weeks. Denser, coarser particles have higher settling velocities, thus having shorter lifetimes than finer particles and water soluble salts in general have shorter lifetimes than particles which are initially hydrophobic. Primary sinks and atmospheric lifetimes of important aerosol types is given in Table 1.2.

Aerosol Species	Size Distribution	Main Sources	Main Sinks	Tropospheric Lifetime	Key Climate Relevant Properties
Sulphate	Primary: Aitken, accumulation and coarse modes Secondary: Nucleation, Aitken, and accumulation modes	Primary: marine and volcanic emissions. Secondary: oxidation of SO2 and other S gases from natural and anthropogenic sources	Wet deposition Dry deposition	~ 1 week	Light scattering. Very hygroscopic. Enhances absorption when deposited as a coating on black carbon. Cloud condensation nuclei (CCN) active.

Nitrate	Accumulation and coarse modes	Oxidation of NOx	Wet deposition Dry deposition	~ 1 week	Light scattering. Hygroscopic. CCN active.
Black carbon	Freshly emitted: occasionally <100 nm typically accumulation mode Aged: accumulation mode	Combustion of fossil fuels, biofuels and biomass	Wet deposition Dry deposition	1 week to 10 days	Large mass absorption efficiency in the shortwave. CCN active when coated. May be ice nuclei (IN) active.
Organic aerosol	POA: Aitken and accumulation modes. SOA: nucleation, aitken and accumulation modes. Coatings occur even on coarse mode primary aerosol	Combustion of fossil fuel, biofuel and biomass. Continental and marine ecosystems. Some anthropogenic and biogenic non-combustion sources	Wet deposition Dry deposition	~ 1 week	Light scattering. Enhances absorption when deposited as a coating on black carbon. CCN active (depending on aging time and size).
... of which brown carbon	Fresh and aged : typically 100–400 nm and as coating on larger particles	Combustion of biofuels and biomass. Natural humic-like substances from the biosphere	Wet deposition Dry deposition	~ 1 week	Medium mass absorption efficiency in the UV and visible. Light scattering.
... of which terrestrial PBAP	Mostly accumulation and coarse mode	Terrestrial ecosystems	Sedimentation Wet deposition Dry deposition	1 day to 1 week depending on size	May be IN active. May form giant CCN

Mineral dust	Coarse and super-coarse modes, with a small accumulation mode	Wind erosion, soil resuspension. Some agricultural practices and industrial activities (cement)	Sedimentation Dry deposition Wet deposition	1 day to 1 week depending on size	IN active. Light scattering and absorption. Greenhouse effect.
Sea spray	Coarse and accumulation modes	Breaking of air bubbles induced e.g., by wave breaking. Wind erosion.	Sedimentation Wet deposition Dry deposition	1 day to 1 week depending on size	Light scattering. Very hygroscopic. CCN active. Can include primary organic compounds in smaller size range
... of which marine POA	Preferentially Aitken and accumulation modes	Emitted with sea spray in biologically active oceanic regions	Sedimentation Wet deposition Dry deposition	~ 1 week	CCN active

Table 1.2: Key aerosol properties of the main aerosol species in the troposphere. Compiled from Table 7.2 of Boucher et al (Clouds and Aerosols, in Climate Change 2013: The Physical Science Basis. Contribution of Working Group I to the Fifth Assessment Report of the Intergovernmental Panel on Climate Change, edited by T. F. Stocker, D. Qin, G.-K. Plattner, M. Tignor, S. K. Allen, J. Boschung, A. Nauels, Y. Xia, V. Bex, and P. M. Midgley, Cambridge University Press, Cambridge, United Kingdom and New york, NY, USA., 2013), with permission, with additional input from (Pöhlker et al., 2012) and (Harris et al., 2013).

1.2.3 Particle size and aerosol size distribution:

The range of size of different aerosol particles is as wide as the type of aerosol particles that can be found in the atmosphere- from 1 nm-sized freshly nucleated particles to 100μm- sized suspended biological particles (Table 1.3). Moreover, all aerosol particles are not spherical in size- they may be elongated, fiber-like, chain-structured, agglomerated, crystal-shaped or irregularly shaped, depending on their mode of formation, source and atmospheric age. Also, an aerosol particle may not necessarily be a single chemical or mineralogical unit. In the natural environment, an aerosol particle often consists of two or more unit structures held together by inter-particle adhesive forces such that the particle behaves as a single unit in suspension or on deposition. Such aerosol is called internally mixed aerosol (Finlayson-Pitts and Pitts Jr., 2000). The mixing state of

aerosol is a concept introduced at a time when single particle analysis was rare, largely to facilitate aerosol treatment in large scale chemistry-climate models. When two chemically different unit structures with different sources are present only in separate particles, then the aerosol is called externally mixed. When two chemically different unit structures coming from different sources are present in one and the same particle, then the aerosol is internally mixed.

Aerosol type	**Physical diameter in μm**
Wind-raised soil dust	1 - 100
Seeds, fragments of animals and plants	1 - 250
Pollen	10 – 30
Viruses	0.05 – 0.15
Bacteria	0.1 – 4
Fungal spores	0.5 – 15
Cigarette smoke	~ 0.1
Black carbon, fumed silica	0.01 – 0.1
Stable nuclei formed due to homogeneous nucleation; Fullerenes	$10^{-3} – 10^{-2}$
SOA formed from SO_2, NO_2 precursors	$10^{-4} – 10^{-3}$

Table 1.3: Aerosol particle types and their approximate sizes. Compiled from Friedlander, S. K. (Smoke,Dust, and Haze-Fundamentals of Aerosol Dynamics, Second., Oxford University Press., 2000), Kokhanovsky, A. A. (Aerosol Optics: Light Absorption and Scattering by Particles in the Atmosphere, Praxis Publishing Ltd., 2008) and Wallace, J. M. and Hobbs, P. V. (Atmospheric Science, Second., edited by R. Dmowska, D. Hartmen, and H. T. Rossby, Academic Press., 2006), with permission.

Due to such extensive heterogeneity in the physical characteristics of particles, multitude of constraints exist in the path of using a single method to quantify the size of all the aerosol particles. In general, particle size refers to the "diameter" of the particle (Friedlander, 2000), but the meaning of the term "diameter" itself is often defined in relation to the measurement tool (physical property) use to estimate the diameter. For particles other than spherical particles, of unit density, with no imaginary term in the refractive index, different measurement techniques do not result in the same diameter estimate for one and the same particle. Therefore, the diameter reported is often an

"equivalent diameter" (Kulkarni et al., 2011). A number of frequently used equivalent diameters is discussed below.

Area equivalent diameter: It is the diameter of a circle that has the same area as the cross-sectional area as projected on a plane, of the particle under consideration. Alternately, it is the diameter of a circle that occupies the same number of pixels in a microscopic image as the 2D projection of the particle being measured.

Volume equivalent diameter: It is the diameter of a spherical particle of the same volume as the particle under consideration.

Aerodynamic equivalent diameter: In atmospheric sciences, the study of the behavior of a particle as it descends down in the air is crucial. Therefore, the aerodynamic diameter (d_a) of the particle is one of the most commonly used parameter for defining particle size and particle size distributions. It is defined as the diameter of a spherical particle of unit density, having the same terminal settling velocity as that of the particle whose diameter is to be measured (Kulkarni et al., 2011). Aerodynamic diameter (d_a) can be related to the volume equivalent diameter of the particle (d_p) through particle densities of the particle (ρ_a) and the reference particle (ρ_0) and shape factors of the reference particles (χ_o) and the actual particle under consideration (χ_a):

$$d_a = d_p \sqrt{\frac{\rho_a \chi_0}{\rho_0 \chi_a}} \quad (1)$$

The aerodynamic equivalent diameter is very commonly used in health studies and for health related legislation and exposure limits, as the aerodynamic behavior determines particle deposition and transport in the respiratory system. PM_{10} i.e. particles with $d_a <= 10\mu m$, are called respirable aerosol fraction or alveolar fraction based on their penetration depth into the lung. Legislation for coarse mode ($d_a > 2.5\mu m$) particular matter exposure, typically regulates only PM_{10} and not total suspended particulate matter with a da <=100 μm due to the larger health impacts of the respirable aerosol fraction. , $PM_{2.5}$ i.e. particles with $d_a <= 2.5\mu m$, called fine mode or accumulation mode particles are treated separately primarily due to their much larger atmospheric residence time. $PM_{0.1}$ i.e. particles with $d_a <= 0.1\mu m$ are called ultrafine mode particles and have recently received much attention due to their potential capability to cross the lung-blood barrier.

Optical equivalent diameter: It is defined as the diameter of a spherical polystyrene latex particle that has the same light- scattering properties as the particle being studied.

Mobility diameter: The electrical mobility diameter is frequently used as an alternative equivalent diameter for particles of <= 1.0 μm which have a small inertia and much higher mobility within the gas phase.

Measuring and reporting the concentration of aerosol particles in the air is an important role of atmospheric scientists. Particles of different sizes affect their environment differently and therefore, end-users demand size-based reporting of aerosol concentrations. Atmospheric aerosol varies in composition with space and time. Monodisperse aerosols (in which all particles have the same size) are rarely found in the atmosphere. Most of the time, aerosol populations are polydisperse, i.e., composed of particles with different sizes present in several different modes. Size distribution functions are therefore used to report the size-wise number concentrations of aerosol particles. Aerosol number distributions from many different sources have been found to fit the log-normal distribution (Kulkarni et al., 2011).

Number distribution of aerosol particles [$n_N(D_P)$], which is characterized as the number of particles per cm^3, is often described in the following mathematical form:

$$N = \int_0^\infty n_N\,(D_P) dD_P\ [cm^{-3}] \quad (2)$$

where $n_N(D_P)$ is the number of particles per cm^3 of air having diameters in the range D_P to (D_P + dD_P).

The corresponding surface area distribution [$n_S(D_P)$] is described as:

$$S = \pi \int_0^\infty D_P^2 n_N\,(D_P) dD_P = \int_0^\infty n_S\,(D_P) dD_P\ [\mu m^2 cm^{-3}] \quad (3)$$

The corresponding volume distribution [$n_S(D_P)$] is written as:

$$V = \frac{\pi}{6} \int_0^\infty D_P^3 n_N\,(D_P) dD_P = \int_0^\infty n_V\,(D_P) dD_P\ [\mu m^3 cm^{-3}] \quad (4)$$

The corresponding mass distribution function is written as:

$$M = \rho_P \int_0^\infty n_V\,(D_P) dD_P\ [\mu g\ m^{-3}] \quad (5)$$

where ρ is the density of the particles. All the above distribution functions typically fit log- normal distribution.

Atmospheric aerosol mass distribution is characterized by the following modes:

(1) **Accumulation mode** [~0.1 μm to ~2.5 μm] which may consist of two overlapping sub-modes: the condensation mode which occasionally results from primary emissions (Poehker et al. 2012) but primarily from new particle formation followed by condensation of secondary sulphates, nitrates, organics from gas phase; and the droplet mode which results from cloud processing of some of the accumulation mode particles. The two modes are frequently separated by the Hoppel gap (Hoppel et al., 1989, 1994).

(2) **Coarse mode** [>2.5 μm to ~50 μm] particles are produced by mechanical processes like wind or erosion and may consist of primary or secondary aerosol particles (Seinfeld and Pandis, 2006). Mass distributions are a poor proxy for the number concentration in case of aerosol particles. In most environments, particles greater than 0.1 μm diameter make up most of the mass of the bulk aerosol but their number is very less as compared to ultrafine particles. Aerosol number

distribution trend can provide insight into the same. Aerosol number distribution is usually made up of Nucleation mode [< 10 nm in size] and Aitken mode [10 – 100 nm in size]. Nucleation mode consists of particles that are freshly created by nucleation from gas phase. Aitken mode consists of particles that have further grow through condensational growth although Aitken mode particles can occasionally be emitted as primary particles. Characteristic number distribution of aerosol particles found in various environments is provided in Table 1.4, with lognormal distribution based mode- wise split-up.

Model Aerosol distribution	Mode I		Mode II		Mode III	
	$N(cm^{-3})$	$D_p(\mu m)$	$N(cm^{-3})$	$D_p(\mu m)$	$N(cm^{-3})$	$D_p(\mu m)$
Urban	$9.93x10^4$	0.013	$1.11x10^3$	0.014	$3.64x10^4$	0.05
Marine	133	0.008	66.6	0.266	3.1	0.58
Rural	6650	0.015	147	0.054	1990	0.084
Remote continental	3200	0.02	2900	0.116	0.3	1.8
Free troposphere	129	0.007	59.7	0.250	63.5	0.52
Polar	21.7	0.138	0.186	0.75	3×10^{-4}	8.6
Desert	726	0.002	114	0.038	0.178	21.6

Table 1.4: Characteristic number concentration (N) and particle diameter (D) of model distributions of aerosols found in various environments. Reproduced with kind permission from Seinfeld, J. P. and Pandis, S. N.: Atmospheric Chemistry and Physics: From Air Pollution to Climate Change, Second., John Wiley and Sons, Inc., 2006.

1.3 Importance of studying aerosol particles

1.3.1 Health effects of atmospheric aerosol particles:

Particulate matter (PM) is often cited as a major cause of health problems (respiratory, carcinogenic, and cardiovascular in nature) and premature deaths in human population due to pollution. The WHO has ranked PM air pollution as 13^{th} leading cause of mortality worldwide, estimating that it contributes to approximately 800,000 premature deaths each year (Anderson et al., 2012). Elevated PM levels in cities and smoke due to indoor solid fuel use, together rival "overweight and obesity" as causes of premature death (Russell and Brunekereef, 2009). The classification of PM (coarse, fine and ultrafine) on the basis of the aerodynamic diameter of the particles, is directly related to the sites of deposition and the way these particles interact with the respiratory and cardiovascular system of the human body. Coarse particles ($d_a > 10$) is the fraction

of particles that cause irritation and local damage on contact with nasopharynx. Respirable/ thoracic fraction of particles ($2.5 > d_a < 10$) that passes the larynx and enters the lungs. These particles can rise on the mucociliary ladder to be expelled by coughing or to be swallowed (Dockery and Pope, 1994). $PM_{2.5}$ ($d_a < 2.5$, fine particles) get deposited in the small airways (bronchioles) of the lungs and interfere with the normal working of lungs, thus causing breathing problems (asthma, chronic cough, and cold). The involuntary cleansing mechanisms can help to remove these particles from the body to some extent. $PM_{0.1}$ ($d_a < 0.1$, ultrafine particles) can seriously damage lung functionality as they get deposited into alveoli (Bai et al., 2015) and may even pass the lung blood barrier (Brown et al., 2002; Geiser et al., 2005; Nemmar et al., 2002). Alveoli don't have self-cleansing mechanisms. Thus, many respiratory diseases and problems (smoker's lungs, lung cancer) may be caused. These particles can also diffuse through the membranes of alveoli and enter the blood circulation. This can result in serious cardiovascular problems such as heart attacks and strokes. Lung macrophages can only slowly remove these small particles by transporting them to the mucociliary ladder or into the lymphatic system.

Although aerosols emitted from natural sources have a higher global budget than the ones emitted from anthropogenic sources (Table 1.1), but they are benign in their impact on human health as opposed to anthropogenic-origin aerosols. The extent of health risks posed by the increase in anthropogenic aerosols in the atmosphere has led to numerous studies trying to find links between PM pollution and health of populations. Many epidemiological studies have shown anti-correlation between PM levels in the air and average life expectancy, health of human populations (Gauderman et al., 2004; Peters et al., 2000; Pope et al., 2009; Raaschou-nielsen et al., 2016; Strak et al., 2012; Tang et al., 2014), and consequently, the national- level economic losses that are incurred. There is limited knowledge about the precise quantification of the health effects of individual PM components from different sources (Strak et al., 2012), but Ni and S containing aerosol particles (Raaschou-nielsen et al., 2016) and combustion- generated particles like black carbon (Janssen et al., 2011) have known to cause serious damage to health.

1.3.2 Optical properties of atmospheric aerosols and their effect on climate:

Atmospheric aerosol particles of separate origins differ in their chemical and physical properties. The shape, size, and color of the particles determine their optical properties, and thus, their impact on the climate. Optical properties of particles will govern whether the particles will be absorbing or scattering in nature and the extent of it, the albedo of the surface on which they get deposited, their ability to act as cloud condensation nuclei (CCN) and their interaction with clouds. In the atmosphere, the presence of aerosol particles causes reduction in visibility as the particles are scattering in nature. Without aerosol particles, it would be possible for the human eye to see 300

km (Seinfeld and Pandis, 2006). Overall, atmospheric aerosol particles cause global dimming by scattering sunlight and reducing the global solar radiation intensity (Wild, 2009). They can also cause "brightening", i.e., increase in the intensity of solar radiation reaching Earth's surface. Aerosol particles cause these two phenomenon by directly modifying the SSR (surface solar radiation) through scattering or by getting incorporated in clouds. Dimming and brightening can therefore result in decrease or increase in the surface temperature, respectively, which can further contribute to global cooling or warming, can modify the intensity of the global hydrological and carbon cycles, and can impact the melting or formation of glaciers and snow cover (Wild, 2009). Thus, presence of aerosol particles disrupts the radiative budget of Earth, enforcing positive or negative radiative forcing (RF). The largest uncertainty in the total RF estimate of Earth is due to aerosol particles (Figure 1.1). Due to the complexity of mechanisms involved in aerosol- radiation interaction, a new term called effective radiative forcing (ERF), which includes rapid adjustments after perturbation, was introduced in IPCC's assessment report 5 (Boucher et al., 2013). In case of aerosol particles, it is further distinguished into: ERF-ari (forcing processes arising due to aerosol-radiation interactions and ERF-aci (due to aerosol-cloud interaction). The ERF of the total aerosol effect in the atmosphere is -0.9 [-1.9 to -0.1] Wm^{-2}. Whereas most aerosol particles contribute negative radiative forcing (i.e., cooling), black carbon (BC) particles cause warming, i.e., positive radiative forcing, due to absorption of solar radiation. Figure 1.1 points to the fact that aerosols of natural origin are mostly cooling in nature whereas particles emitted from anthropogenic activities can also cause warming. Bond and co-workers (Bond et al., 2013) explain the ways in which BC causes positive RF. Being dark in color, black carbon particles increase the albedo (ratio of the amount of incident radiation absorbed to the amount of total incident radiation) of the surface on which they get deposited, also causing ice blocks and snow cover to melt rapidly. When BC particles get incorporated into clouds, they cause "burning" of clouds due to absorption of solar radiation by the darkened cloud water droplets. Brown carbon can also cause similar effects due to its light-absorbing nature (Alexander et al., 2008).

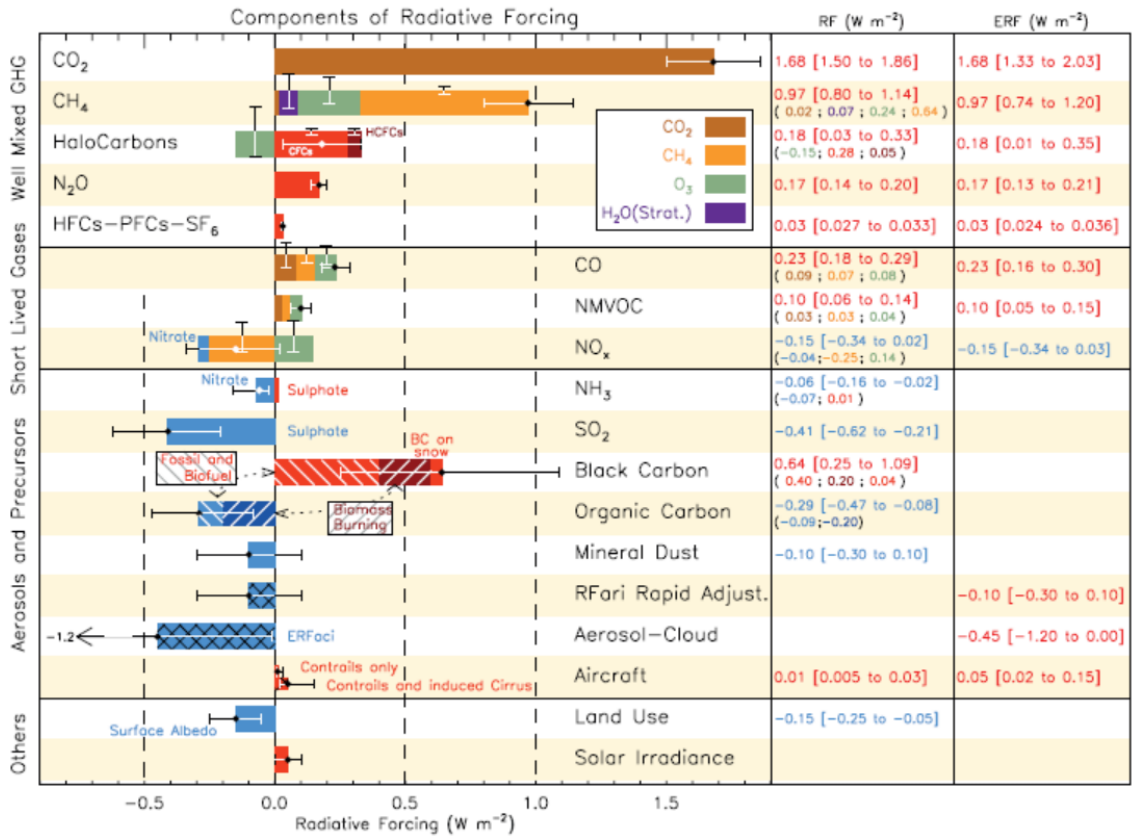

Figure 1.1: Radiative forcing (RF) of climate change during the Industrial Era shown by emitted components from 1750 to 2011. The horizontal bars indicate the overall uncertainty, while the vertical bars are for the individual components (vertical bar lengths proportional to the relative uncertainty, with a total length equal to the bar width for a ±50% uncertainty). Best estimates for the totals and individual components (from left to right) of the response are given in the right column. Values are RF except for the effective radiative forcing (ERF) due to aerosol–cloud interactions (ERFaci) and rapid adjustment associated with the RF due to aerosol-radiation interaction (RFari Rapid Adjust.). Note that the total RF due to aerosol-radiation interaction (–0.35 Wm^{-2}) is slightly different from the sum of the RF of the individual components (–0.33 Wm^{-2}). The total RF due to aerosol-radiation interaction is the basis for Figure SPM.5. Secondary organic aerosol has not been included since the formation depends on a variety of factors not currently sufficiently quantified. The ERF of contrails includes contrail induced cirrus. Combining ERFaci –0.45 [–1.2 to 0.0] Wm^{-2} and rapid adjustment of ari –0.1 [–0.3 to +0.1] Wm^{-2} results in an integrated component of adjustment due to aerosols of –0.55 [–1.33 to –0.06] Wm^{-2}. CFCs = chlorofluorocarbons, HCFCs = hydrochlorofluorocarbons, HFCs = hydrofluorocarbons, PFCs = perfluorocarbons, NMVOC = Non-Methane Volatile Organic Compounds, BC = black carbon. Reproduced with permission from Stocker et. al. (Stocker, T. F., Qin, D., Plattner, G. K., Alexander, L. V., Allen, S. K., Bindoff, N. L., Breon, F.-M., Church, J. A., Cubasch, U., Emori, S., Forster, P., Friedlingstein, P., Gillett, N., Gregory, J. M., Hartmann, D. L., Jansen, E., Kirtman,

B., Knutti, R., Krishna Kumar, K., Lemke, P., Marotzke, J., Masson-Delmotte, V., Meehl, G. A., Mokhov, I. I., Piao, S., Ramaswamy, V., Randall, D., Rhein, M., Rojas, M., Sabine, C., Shindell, D., Talley, L. D., Vaughan, D. G. and Xie, S.-P.: Technical Summary, in In: Climate Change 2013: The Physical Science Basis. Contribution of Working Group I to the Fifth Assessment Report of the Intergovernmental Panel on Climate Change, edited by T. F. Stocker, D. Qin, G. K. Plattner, M. Tignor, S. K. Allen, J. Boschung, Y. Nauels, Y. Xia, V. Bex, and P. M. Midgley, Cambridge University Press, Cambridge, United Kingdom and New york, NY, USA., 2013.), Figure TS.7.

Aerosol particles have complex interaction with clouds that can also impact global climate. Hygroscopicity and size of the particles determine their ability to act as CCN (cloud condensation nuclei) and to initiate ice nucleation. Aerosol particles are necessary for the formation of clouds. Rosenfeld and co-workers (Rosenfeld et al., 2014) explain the role of nucleating aerosols. In polluted environments, a large number of particles get nucleated to form smaller cloud drops. Smaller drops tend to evaporate faster and also prevent break- up of the cloud, which results in the formation of longer-lasting clouds. Delay in precipitation also causes invigoration of deep convective clouds that emit less thermal radiation from their colder tops. The intensity of rainfall due to such clouds is also very high and sometimes, destructive in nature.

In view of the significance of the impact of aerosol particles on climate and on human health, national ambient air quality standards (NAAQS) are laid down for PM_{10} and $PM_{2.5}$ concentrations, in most countries. Central Pollution Control Board, Government of India, has fixed the exposure limit at 60 $\mu g/m^3$ (annual) and 100 $\mu g/m^3$ (24-hours) for PM_{10}, and 40 $\mu g/m^3$ (annual) and 60 $\mu g/m^3$ (24-hours) for $PM_{2.5}$.

1.4 Source Apportionment

In atmospheric sciences, to attribute (and possibly quantify) an air pollutant's measured concentration to it's different sources, is termed as Source apportionment. Thus, it is an important effort that can provide insight into the different types (and/ or locations) of sources of a pollutant, their contribution to the overall concentration of the pollutant in air, any modification that the specie undergoes during transport and provide cues about mitigation measures that can be taken in order to control emissions of the pollutant. While formulating policies for combating pollution, governments refer to findings of source- apportionment studies. Chemical analysis, study of air transport patterns, a-priori knowledge of sources, measurement of pollutant concentration at receptor site or in-situ at the source, simulating dynamics of airmass transport in the atmosphere, are some essential steps involved in source- apportionment studies. Many studies carried out in

the past have employed various techniques of source-apportionment, in order to identify the sources of various air pollutants, including PM_{10}, $PM_{2.5}$ or specific aerosol particles. This has also lead to the development of many computer models that perform or assist the respective task. Fleming and co-workers (Fleming et al., 2012) review the different methods of source-apportionment that are used in the field of atmospheric sciences, and the advantages and limitations of each. Source apportionment has been discussed in detail in Chapter 3.

1.5 Short review of source apportionment methods for black carbon and bulk aerosol

1.5.1 Optical method vs. C-14

The optical method of source- apportionment is generally applied to light absorbing aerosol particles like Black carbon. In this method, a characteristic of aerosol, which is based on the extent of absorption of light by the particles, generally the absorption angstrom exponent, is determined with the help of instruments like Aethalometer, that measure mass loading of aerosol particles based on the principle of optical absorption. Absorption angstrom exponent (α_{abs}) is a measurement of the spectral dependence of light absorption by aerosol. Large α_{abs} means higher spectral dependence, i.e., aerosol is more favored towards absorbing light of some specific wavelength(s). Due to difference in the absorption properties of black carbon (BC) from different sources, their α_{abs} is different. E.g., BC from fossil- fuel combustion typically has an $\alpha_{abs} = 1 \pm 0.1$, whereas BC from combustion of biomass has $\alpha_{abs} > 1$, due to presence of UV light absorbing materials, like HULIS (HUmic- LIke Substances), PAHs (Poly- Aromatic Hydrocarbons), which are also combustion products, in BC. Based on this property of α_{abs}, the two- component Aethalometer model was developed by Sandradewi and co-workers (Sandradewi et al., 2008c). , which apportions total BC into BC from wood burning (BC_{wb}) and BC from fossil fuel combustion (BC_{ff}). They recommended using $\alpha_{ff} = 1.1$ for traffic BC and $\alpha_{wb} = 1.8\text{-}1.9$ for wood burning BC and validated the method and parameterization with data collected in the Swiss Alps, where wood burnt in stoves for domestic heating purposes and traffic dominate BC emissions. For the validation, a set of independent wood burning tracers such as C-14, levoglucosan and potassium were employed (Sandradewi et al., 2008b). The model showed good agreement with results from CMB (Chemical Mass Balance) model applied to data from the Alpine region (Favez et al., 2010). Since then, the two- component aethalometer model has been employed by many source-apportionment studies based in the London (Crilley et al., 2014), Alpine region (Herich et al.,

2011), and in India (at a remote village site (Gadhavi and Jayaraman, 2010) and in New Delhi (Tiwari et al., 2014)).

C-14 (a radioactive isotope of carbon), found naturally in organic material, has been widely used in many fields for radiocarbon dating, i.e., for determining the age of an object, and for determining the presence of organic material in an object (Boersema and Reijnders, 2009). Carbon- 14 is produced in the atmosphere when neutrons in cosmic rays bombard atmospheric Nitrogen (Libby, 1967).

$$^{14}_{7}N + n \rightarrow {}^{14}_{6}C + p \quad (6)$$

where, n is neutron and p is a proton. It is abundant in the atmosphere (for every 10^{12} parts of ^{12}C, there are 1.5 parts of ^{14}C) and gets incorporated into living cells when organisms take up carbon dioxide that contains radioactive carbon. C-14 undergoes a beta- minus decay to become stable, via the following reaction:

$$^{14}_{6}C \rightarrow {}^{14}_{7}N + p + e + antineutrino \quad (7)$$

where, p is a proton and e is an electron (i.e., beta particle). The half- life of C-14 is about 5,730 years (Currie, 2000). Therefore, the determination of the amount of C-14 in organic material provides clue to it's age. Beta counters and currently, AMS (Accelerator Mass Spectrometers) are instruments that are used to determine the level of radioactivity or relative amount of C-14 in the sample.

Clayton and co-workers (Clayton et al., 1955) were the first to apply radiocarbon dating method in aerosol science, for source- apportionment of carbonaceous aerosols derived from fossil- fuel combustion and biomass combustion. Source- apportionment of aerosol particles, based on C-14 analysis has become only more reliable since then, and is being applied widely in many studies (Currie et al., 1997; Gelencser et al., 2007; Hodzic et al., 2010; Lewis et al., 2004; Simoneit, 2002; Weber et al., 2007). In case of atmospheric aerosol samples, fraction of modern carbon, f_M (Currie, 2000) is used to calculate a radiocarbon age from AMS's data.

$$f_m = \frac{{}^{14}C/_{12}C \; ratio \; for \; the \; sample}{{}^{14}C/_{12}C \; ratio \; for \; modern \; carbon} \quad (8)$$

Therefore,

$$Biomass \; fraction \; in \; sample = f_m \times Biomass \; fraction \; in \; modern \; carbon \; (SRM) \quad (9)$$

Various SRM (standard reference material) values have been used in the past, including a NIST Urban Particle SRM as an aerosol organic chemical standard, a diesel soot SRM, wood from the 1950s, NIST 2000, etc.

For fossil- fuel derived aerosol, value of f_m is a direct indication of the amount of biomass. Whereas in case of biomass- combustion derived aerosol, two corrections are required to reach the value the amount of biomass. First is the correction for ^{14}C decay from sampling date to reference date of f_m, which is not very significant considering the long half- life of ^{14}C. Second is the correction for the time- dependent enhancement of biospheric ^{14}C due to atmospheric nuclear testing, which can be significant because $^{14}C/^{12}C$ ratio in the atmospheric CO_2 almost doubled during the mid-1960s (Currie, 2000).

Overall, C-14 analysis is considered to be highly reliable in all fields of science, including aerosol science.

Based on observations made during studies from India, it has been observed that the two component Aethalometer model doesn't conform with the results from the reliable C-14 analysis. Gadhavi and Jayaraman (Gadhavi and Jayaraman, 2010) used the two-component Aethalometer source-apportionment model to calculate the contribution of biomass burning to total BC in morning and evening times in a remote village site and estimated that only 20-40% of the BC originates from biomass combustion. Similarly, Tiwari et al. (Tiwari et al., 2014), using the Magee Scientific Aethalometer model (AE 31), found that α_{abs} of BC varied from 0.63 to 1.29 (with a mean value of 1.09±0.11) during winter 2011-12 in New Delhi and concluded that ~94% of the BC originated from fossil fuel combustion and only ~6% of the BC was contributed by biomass burning. Both findings are unexpected, considering the rampant use of biomass for domestic cooking and heating purposes, particularly in rural India, and during wintertime in the IGP. These facts, based on activity observation were also confirmed using C-14 analysis of black carbon aerosol. Gustafsson and co-workers (Gustafsson et al., 2009) found that biomass combustion in India contributed between half and two thirds to the total BC over India. Currently used emission inventories attribute 55%-88% of the BC emissions over South Asia to biomass combustion (Dickerson et al., 2002; Reddy and Venkataraman, 2002a, 2002b; Venkataraman et al., 2005). The contrast between the findings based on the two-component Aethalometer source-apportionment model and other estimates based on independent tracers such as C-14 or aerosol chemical composition suggest that this approach has its limitations over regions where more complex set of biofuels are encountered. Moreover, the fact that α_{abs} of BC for individual measurement points dropped to values as low as 0.63 during fog episodes in New Delhi, i.e. well below $\alpha_{abs} = 0.9$, (which is considered to be the lowest possible value for calculations employing the two-component Aethalometer model) seems to suggest that aerosol mixing state or coatings acquired during aqueous phase processing may affect α_{abs}. It should also be noted that in current literature, reported α_{abs} values vary from 1.3 to 6.5 (Chakrabarty et al., 2010; Clarke et al., 2007; Herich et al., 2011; Hoffer et al., 2006; Kirchstetter et al., 2004; Lewis et al., 2008; Reid et al., 2005;

Sandradewi et al., 2008b; Schmid et al., 2006; Yang et al., 2009) for wood burning, and from 0.9 to 1.1 (Bond, 2001; Kirchstetter et al., 2004; Lewis et al., 2008) for fossil fuel burning. Values lower than 0.9 have not been discussed so far but have been observed experimentally in India (Gadhavi and Jayaraman, 2010; Tiwari et al., 2014). The large range of literature-reported values results in large uncertainties of the reported fraction of biomass combustion BC, whenever the method is used in a new environment where it has not been validated by simultaneous independent measurements of BC_{bb} (e.g. C-14) and my results discussed in Chapter 3 show, that it may be altogether unreliable because the α_{abs} of BC may depend on combustion efficiency rather than fuel type.

1.5.2 Trajectory cluster analysis

Cluster analysis is a commonly used source- apportionment tool, which is used to trace back the origin of air masses carrying aerosol particles, thus providing clue to the source of aerosol particles reaching a receptor site. Back- trajectories derived from online trajectory models or determined through other methods, are often employed for this purpose. These back- trajectories are produced in the form of co- ordinates of trajectory segments at equal time steps. Depending upon the scale of trajectory transport, the scale of aerosol transport is determined by this method, e.g., application of cluster analysis to long, trans- national back- trajectories will determine the long-range sources of aerosol particles. Cluster analysis involving back- trajectory data is more suitable for long- term studies due to bigger databases and thus provide more statistically robust results. Cluster analysis is a statistical method used to group data in large data sets into a small number of clusters. Clusters are groups with similar distributions, in the case of back trajectories, similar directions and lengths or a combination of trajectory pathways and composition (Fleming et al., 2012). Cluster analysis is often performed using statistical tools like PAST (PAleontological STatistics), MS Excel, Igor Pro, etc. This method can be applied on air masses' trajectory coordinates (time steps) as the clustering variables. Hierarchical and non- hierarchical algorithms of doing clustering exist. A non-hierarchical method known as the k- means procedure is commonly used (Pawar et al., 2015). The air mass back trajectories are subjected to k- means clustering using statistical software and The number of clusters "k" is to be specified by the user prior to clustering. The assignment of back- trajectories to clusters is initially random. In an iterative procedure, trajectories are then moved to the cluster which has the closest cluster mean in Euclidean distance, and the cluster means are updated accordingly. This process continues until the process of hopping from one cluster to another, ceases. As a normal artefact of the k- means clustering algorithm, the result is dependent upon the seed used for clustering. Clustering result with the lowest root mean square

difference for each predefined number of clusters is selected. The root mean square difference for an individual latitude and longitude value is given by

$$RMSD = \sqrt{(x_i - \bar{x})^2} + \sqrt{(y_i - \bar{y})^2} \quad (10)$$

where, x_i and y_i stand for the latitude and longitude of the individual trajectory for a given hour and $\bar{x}$ and $\bar{y}$ for the cluster mean latitude and longitude of the same hour for the cluster to which that trajectory belongs. The total root mean square difference t-RMSD is the sum over all the RMSD values for a given set of back trajectories. The optimal number of clusters that best describe the different air-flow patterns to the measurement site by computing the change in the minimum t-RMSD while increasing the number of clusters from n to n+1, are selected. This change in the minimum t-RMSD decreases abruptly as clusters of trajectories which are significantly different in terms of wind directions and speeds are separated from each other.

Aerosol mass loadings are associated with these clusters to determine their source of origin. The limitation of this method is that it cannot be effectively applied for studies that are based on short periods of time as it needs a large statistical base. Moreover, cluster analysis of the trajectory data (Baker, 2010; Li et al., 2012) groups air masses into groups of similar origin and associates elevated PM_{10} mass loadings or exceedance events with certain large scale atmospheric transport situations and broad regions upwind, but does not attribute them to specific sources with spatially fixed coordinates.

1.5.3 CWT

Back- trajectory data can be attributed to sectored geographical area (e.g., cells of a superimposed grid) based on residence time analysis (RTA) (Lee and Ashbaugh, 2007; Stohl, 1998). Such RTA includes the CWT (Seibert et al., 1994) (Concentration weighted trajectory) maps, which are produced by calculating weighted concentration averages for cells of a spatial grid over which the back-trajectories of air masses passed prior to reaching receptor sites. Such an approach seeks to attribute all of the aerosol mass loading observed at a receptor site to spatially distant sources under the assumption that each grid cell over which the air mass passed in the hours prior to reaching the receptor site has an equal probability of being the source of the aerosol measured at the receptor site. For each cell i, the following relationship is used to calculate the concentration weighted average (CWA) value that signifies the contribution of the cell to the aerosol mass loading observed at the receptor site:

$$CWA_i = \frac{\Sigma\,(\text{Aerosol concentrations associated with the contributing air mass trajectories})}{\text{No.of contributing air mass trajectories}} \quad (11)$$

It has been demonstrated that this approach is mathematically robust only when multiple receptor sites are used to drive the model (Keeler and Samson, 1989; Lee and Ashbaugh, 2007), although

most studies employ single-site datasets only (Fleming et al., 2012). Similarly, back-trajectory analysis can involve calculating residence time weighted concentration (RTWC) (Stohl, 1996) for the geographical sectors. Generally, the result is produced in the form of contour map over a gridded array of cells and helps to identify the spatial location of sources. However, the meteorological grids behind back- trajectory models have a limited resolution (typically 1° x 1°) and hence back- trajectory analysis is not suitable to pinpoint sources on a regional scale, where the required pixel resolution would be of a few kilometers at the most.

1.5.4 Conditional probabilities

Conditional probabilities can be integrated with many source- apportionment techniques to add to their ability and usefulness. Gridded maps with residence time analysis function values (that use trajectory data) and the conventional source- locator tools like wind roses and pollution roses (that use wind data), are often modified to show conditional probability function values of different kinds. Conditional probability functions help to indicate the relative potential strength of sources. They are calculated as:

$$Conditional\ Probability\ value = \frac{No.of\ air\ masses\ that\ satisfy\ a\ condition}{Total\ number\ of\ air\ masses} \qquad (12)$$

This condition is generally defined in terms of exceedance of pollutant concentration associated with an air mass, beyond a pre- decided threshold level (Fleming et al., 2012). The conditional probability value associated with a grid cell or a wind direction will therefore provide probability of it being a potential source of a pollutant. Thus, this technique is purely a statistical tool and depends on the size and quality of database.

PSCF (Potential Source Contribution Function) is a kind of Conditional Probability which is applied to segmented trajectory data for attributing source contribution value to grid cells of a gridded spatial map. In this, for each grid cell, the ratio of the number of trajectory segments arriving on a day which had source contribution factor greater than a criterion value, that lie in the cell, to the total number of trajectory segments falling in the cell, is used to calculate the PSCF value of the cells.

1.5.5 PMF

US EPA's PMF (Positive Matrix Factorisation) Model is a multivariate mathematical model that helps to determine primary sources of pollutants measured at a receptor site using factor analysis. PMF analyses are used in regulatory studies to assess pollution sources (Fleming et al., 2012). From a data matrix of certain number of dependent or independent pollutants in a given number of samples, the PMF model helps to determine the contribution of pollutant source factors, the

chemical fingerprint (source profile) for each factor, the contribution of each factor to each sample, and the residuals of the dataset using the following equation (Paatero and Tapper, 1994):

$$X_{ij} = \sum_{k=1}^{p} g_{ik} f_{kj} + e_{ij} \quad (13)$$

where, X_{ij} is the pollutant data matrix with *i* number of samples and *j* number of measured pollutants which is resolved by the PMF model to provide *p* number of possible source factors with the source profile *f* of each source and mass g contributed by each factor to each individual sample, leaving the residuals *e* for each sample. In order to obtain the solution of the above equation 13, sum of squared residuals (e^2) and variation of data points (σ^2) is inversely weighted in PMF. PMF produces a parameter called explained variability which indicates the contribution of each source factor to the individual compound, and this is most useful to policy makers for planning mitigation strategies. It is a very commonly used tool but requires expertise to run the model (as the number of factors have to be pre-decided by the user and there is no simple way of estimating the correct p) and for interpretation of results. In comparison to other commonly used receptor models based on principal component analysis and absolute principal component scores, PMF provides more robust results as it does not permit negative source contributions or source fingerprints. This model can be used to perform comprehensive regional source apportionment of multivariate chemical data. PMF can attribute the pollutant concentrations to different sectors or chemical processes (e.g. transport, industry, windblown dust, gas-to-particle conversion), but it is not useful for identifying (pin-pointing) individual sources in a spatial context and requires chemical information, which is available for a limited number of air quality monitoring stations. An additional limitation is that the number of sources that can theoretically be resolved is limited by the number of chemical species in the input data and the ratio between the number of species and the number of factors should typically not be less than 3 (Paatero and Tapper, 1994).

1.5.6 PCA

Principal component analysis (PCA) is applicable in the same way and in the same situations as PMF, but with comparatively limited effect and usefulness. It is used to reduce the complexity of atmospheric data and explain the total variance of atmospheric species (Fleming et al., 2012), and to find the components or factors that contribute to pollutant concentrations measured at a receptor site. It finds hypothetical variables (components) accounting for as much as possible of the variance in multivariate data (Jolliffe, 2002). These new variables are linear combinations of the original variables in the input data. The input data is a matrix of multivariate data, with items in rows and variates in columns. PCA requires input data variables to be normally distributed for the analysis (Pinxteren et al., 2010), but normally distributed ambient datasets are rare. Eigen analysis is then performed to find eigenvalues and eigenvectors of the variance-covariance matrix or the

correlation matrix, whichever was input. The eigenvalues give a measure of the variance accounted for by the corresponding eigenvectors (i.e., the components). The percentage of variance accounted for by these components are also given. These components are the factors or the sources that contributed to the chemical dataset. PCA allows negative factor loading, i.e., negative emissions of a given specie from a source, and negative factor contribution, i.e., existence of negative sources, which is physically unreasonable except in cases of species that are in a reversible equilibrium (e.g. $NH_3 + HNO_3 \leftrightarrow NH_4NO_3$). So, PCA is becoming less suitable in view of the availability of better models like PMF and CMB (Chemical Mass Balance).

It should be noted that all simple source apportionment models relying on chemical data (including PMF, CMB and PCA) have trouble dealing with chemical reactions or loss processes that result in aging of aerosol particles and/or may change source fingerprints between the source and the receptor site. For example, when the abundance of crucial signature compounds such as levoglucosan (typically considered as the best biomass burning tracer) changes due to photochemical aging (the lifetime with respect to OH is less than a day), this can severely impact the estimated biomass burning contribution. On the other hand, potassium is a conserved biomass burning tracer unless wet deposition occurs, but K containing aerosol particles may activate at sub-saturation RH and will form salts with several different acidic components from the gas phase (mostly sulfate and nitrate) through aqueous phase reactions which again can compromise the fingerprint. Moreover, several natural processes such as fungal spore discharge can add to the K loading. As a consequence, models frequently give a large number of factors representing preferred salts (ammonium sulfate, ammonium nitrate, ammonium chloride, calcium sulfate, potassium sulfate and/or nitrate (depending on the SO_2 and NOx mixing ratios in the gas phase) and sodium chloride, sulfate and nitrate (depending on pH and gas phase composition)) and few if any factors representing primary aerosol other than as broad classes such as dust, seas salt and black carbon. The individual combustion sources resulting e.g. in black carbon emissions are rarely resolved in factorization models relying on chemical tracers unless the aerosol has been freshly emitted from nearby sources.

1.6 Research motivation and thesis outline

The importance of the development and suitable application of source- apportionment tools in order to identify sources of various aerosol particles and to determine their contribution to aerosol mass loadings in specific environments has been highlighted in the previous sections. Correct employment of these techniques provide clues for the formulation of effective mitigation

strategies, which are crucial to combat the problem of various forms of air pollution worldwide. But many times, the results of source- apportionment studies have been misleading, either due to application of the tools without customization to suit the dynamics of the specific study environment or because of limitations of the tool itself (because complete understanding of the strengths and weaknesses of techniques happens gradually over time, with every ensuing study).

The main motivation of this thesis was to perform source- apportionment of equivalent BC at a sub-urban site in Mohali and of PM_{10} in Hessen, Germany, by the application of existing and newly- developed source – apportionment tools, while testing the validity and effectiveness of the application of these techniques. Chapter 2 of the thesis discusses advantages and limitations of the different analytical techniques that are used for measurement of aerosol particles and of the various tools for their source- apportionment. The subsequent chapters then aim to address the following six questions:

1) Can absorption angstrom exponent (α_{abs}) be used as a generic tracer for biomass burning emissions in a complex environment?
2) How does α_{abs} of BC vary for different types of biomass burning sources in a complex environment?
3) What factors determine the value of α_{abs}?
4) How efficiently can our newly- developed models- MuSAM (Multi- receptor Source Apportionment Model) and MuReSAM (Multi- receptor Regional Source Apportionment Model) work, to find the long- range and regional sources of PM_{10} over Hessen, Germany?
5) What is the percentage contribution of long- range, regional and local sources to the total PM_{10} measured over Hessen during the time of study?
6) What was the effect of closing down and then subsequent repair and re-opening of Schiersteiner Brücke on the local PM_{10} loading?

The first three questions have been addressed in Chapter 3, where the application of the two-component aethalometer model to measurements made in a sub-urban site in Mohali, Punjab was tested, and subsequently, the validity of the use of angstrom exponent (α_{abs}) for source-apportionment of black carbon in more complex environments was verified. In this study, the variation of angstrom exponent (α_{abs}) values of BC from different sources were also determined. Since the α_{abs} values did not behave as expected, the real factors that decide the value of α_{abs} were explored. The study presented in this chapter is the first to combine real- time measurements of gas- phase VOC combustion tracers with BC measurements for specific identification of ambient combustion plumes, and the first to use high- time- resolution observations of biomass burning tracers to identify biomass burning events. It is also the first study to highlight the limitation of

using two- component aethalometer model for source- apportionment of BC, thus warning about the erroneous results that may be reached by incorrect application of the model.

Questions 4- 6 were addressed in Chapter 4 of the thesis which deals with the development and application of two statistical source- apportionment models- MuSAM and MuReSAM, which produce graphical output in the form of gridded geographical maps, and help to quantify the contribution of long- range, regional and local sources of PM_{10} (and other pollutant species) by the use of reverse- modelling technique. The study presented in this chapter points to the limitations of source- apportionment techniques that try to attribute all of the measured concentration of pollutant species to long range transport and all of it to the regional sources, alike. This study presents the working of a newly- developed integrated modelling approach for source-apportionment at long- range transport and regional scale. It is the first study that uses real- time ambient data from multiple receptor sites, for quantitative statistical source apportionment of PM_{10} to both, distant and regional sources.

Chapter 2

Quantitative Measurement of Aerosol Properties and Mass

2.1 Analytical considerations and Challenges

Taking accurate and precise measurements of something as simple as aerosol mass becomes a huge analytical challenge due to the fact that aerosol particles are defined as a suspension of liquid or solid particles, with negligible terminal fall velocity, in a carrier gas. Measurements are complicated by the fact that the solid or liquid particles are in permanent chemical equilibrium with their carrier gas. As a consequence, aerosol mass and optical attenuation can change drastically when the relative humidity increases from 20% to 100%. Salt containing particles undergo hygroscopic growth at RH values much below 100% RH. Typically, deliquescence occurs between 70% and 85% RH for most salts. At 100% RH the hygroscopic growth factor, defined as the ratio of the wet diameter under ambient conditions and the dry diameter of the same particle can be as large as 3 for common salts (e.g. sea salt) responsible for a significant fraction of the global aerosol burden. Hence the aerosol mass can change with a factor of $\sim 3^3$ with a simple change in RH. To complicate matters further, most aerosol particles display significant hysteresis with efflorescence occurring at much lower RH (typically < 40%) than deliquescence. If the initial dry diameter is within the regime where Rayleigh scattering dominates then for the same change in ambient RH the scattering cross section can change by $\sim 3^6$ i.e. almost three orders of magnitude. This means, that despite changing ambient conditions, measurements conditions and the reported mass must be standardized and normalized.

An additional complication is poised by the vast heterogeneity associated with the size, origin, composition, optical properties, and chemical and physical properties of aerosol particles. Due to the vast size range (5-6 orders of magnitude), it becomes challenging to measure and quantify size and number distributions for the whole range using one and the same technique and instrument. There is also large spatio-temporal variability in characteristics of atmospheric aerosols. As a consequence, measurements taken at one place, cannot be generalized to other environment, where dominant sources, the technological level (e.g. emission standards for cars) and/or the chemical environment in which the particles are aged differ. Figure 2.1 exhibits the degree of variability in

the chemical composition of the volatile fraction of the PM_1 aerosol in the Northern Hemisphere. All measurements presented in the figure were obtained using an Aerosol Mass Spectrometer (AMS), which does not permit particles with an aerodynamic diameter above 1 μm to enter, and which does not detect refractory particles (particles that do not vaporize at 600°C). As a consequence, mineral dust, black carbon and certain salts (e.g. sea salt) are not included in the aerosol mass of the pie charts, although they are known to contribute to PM_1 aerosol, based on results obtained from scanning electron microscopic single particle analysis (Ebert et al., 2000; Harris et al., 2013; Pöschl et al., 2010). Remote background sites with low mass loadings and Aitken mode particulate due to their small contribution to aerosol mass, also present analytical challenges. All this adds to the list of analytical challenges related with measurement of aerosol particles. A variety of sophisticated techniques exist that are mostly able to measure only two or three properties of the sampled particles at one time. These techniques may depend on off-line collected sample or may allow near real-time measurement of aerosols by in-situ, online data collection (Kulkarni et al., 2011). In atmospheric sciences, the amount of aerosol, the aerodynamic behavior of the particles, their optical properties- and their behavior in the presence of water vapor are the four most important subjects of interest. Whereas aerodynamic behavior depends on the size, density and shape of the particle, optical properties depend upon the colour, size and shape and the interaction with water vapor depends on chemical composition of the particle. Since hygroscopic growth changes the size and the scattering cross section drastically, chemical composition becomes an important parameter even while predicting optical properties.

US EPA (Environment Protection Agency) gives a list of reference and equivalent methods for measuring ambient concentrations of certain air pollutants, including PM. Each process of measurement has multiple options of techniques that can be used. Choice of a measurement technique depends on the requirement and intended application, and users often modify existing/commercially available instruments to suit their requirements. Like all measurement techniques, PM measurement techniques make use of one or more physical or chemical properties of particles, that helps in unique identification of distinct particles. Since particle behavior is very sensitive to impact on surfaces, the aerodynamic flow regime, pressure changes and momentum changes and high losses occur if the nature of material in contact with the sample air flow permits charge buildup, the design and material of instruments and transport channels/ sampling lines, are based on due scientific analysis such as to avoid losing particles of the target size range in the inlet or in lines.

Size is the most fundamental property with regard to aerosol particles. So, most instruments (that may study single particle at one time or a group of similar particles together) that are used for aerosol measurements involve sizing, i.e., segregating the particles into size-based bins and it is

generally done on the basis of aerodynamic or optical diameter of the particles for coarse mode particulate and based on the mobility diameter or vacuum aerodynamic diameter for smaller particles. Inertial separation, gravitational sedimentation, electrostatic precipitation are techniques that are used for segregating particles with a specific size from rest of the particles. Upon segregation, particles are mostly collected on fibrous, membrane or capillary pore filters or transmission electron microscopy grids. Inertial separation based devices- impactors and cyclones are most widely used.

For measuring the size of particles in real time, instruments like APS (Aerodynamic Particle Sizer), DMA (Differential Mobility Analyzer), OPC (Optical Particle Counter) are used. Each instrument is limited in function by the method on which it is based, e.g., OPC, which uses light scattering to detect the particles, works only for particles > ~0.5 μm since the wavelength of light becomes large relative to the particle diameter for particles smaller than 0.5 μm. Techniques which are based on inertia like the APS do not perform well for aerodynamic diameters below 1 μm while techniques based on the electric mobility of particles can only be applied to specific ranges (e.g. 1-300 nm or 10 to 1000 nm) and display a drop in their detection efficiency at both ends of their dynamic range.

For measurement of mass concentration of particles in real time, methods like BAM (beta-attenuation method), TEOM (Tapered- Element Oscillating Microbalance), CAMM (Continuous Ambient Mass Monitor), DMM (Dekati Mass Monitor), etc. are used. However, the reference method for mass detection is offline sampling followed by 24 hours conditioning at <40% RH in a desiccator containing anhydrous calcium sulfate under laboratory conditions (25°C) followed by gravitational determination of the aerosol mass.

For determining the chemical composition of aerosol particles, off-line sampling is the more commonly deployed method of collection. Techniques like ion chromatography, FTIR (Fourier Transform Infrared Spectroscopy), Thermal- Optical methods, TD- GC- MS (Thermal Desorption-Gas Chromatography – Mass Spectroscopy), HPLC (High- Performance Liquid Chromatography) are employed for determination of chemical composition.

Microscopy techniques like SEM (Scanning Electron Microscope), TEM (Transmission Electron Microscope), in combination with EDS (Energy Dispersive X-ray Spectroscopy) are widely used to study individual particles for their elementary composition, size and morphology, although occasionally the chemical or isotopic composition is measured on similar scaled using Nano Secondary Ion Mass Spectrometry (NanoSIMS). Microscope imaging and chemical analyses provide insightful information about physical and chemical properties of particles and aid in visualizing their scale and shapes (Pósfai and Buseck, 2010). There are instruments called CCN counters, that determine the fraction of particles that grow into cloud droplets upon exposure to

supersaturation, thus providing information about the ability of the mix of particles to enable cloud seeding. HDMA instruments (composite instrument employing two DMA analyzers in tandem to measure the wet and dry diameter of aerosol in a certain size range) provide information about hygroscopic growth factors at sub saturation relative humidity.

Aerosol Mass Spectrometer (AMS) is a versatile instrument that sizes a group of particles and analyses them in real- time to determine aerosol mass loading, particle mass distributions, and their chemical composition. It produces a multitude of spectra which have to be interpreted by the user for meaningful information. Instruments specialized for the analysis of non-refractory PM_1 give accurate quantitative data with the rider, that the refractory fraction of the aerosol is completely missing. Laser ablation aerosol mass spectrometers cover all particle types and provide mixing state information on a single particle scale in real time, but accurate quantification of the mass of any element or compound (e.g. carbon, silicon or oxygen) in the particle is challenging, as ionization efficiency can vary over ~5 orders of magnitude depending on the chemical bonding within the particle.

Nephelometer is used to measure scattering of light be aerosols. Optical light absorption is measured using instruments like Aethalometer, PAS (Photo- Acoustic Spectrometer), MAAP (Multi Angle Absorption Photometer) and UV-visible spectrometer to determine the mass concentration of light-absorbing particles and the extent to which they absorb light. This further helps to determine parameters associated with optical interaction of particles, like Angstrom exponent complex refractive index, SSA, absorption coefficient, mass absorption efficiency, etc.

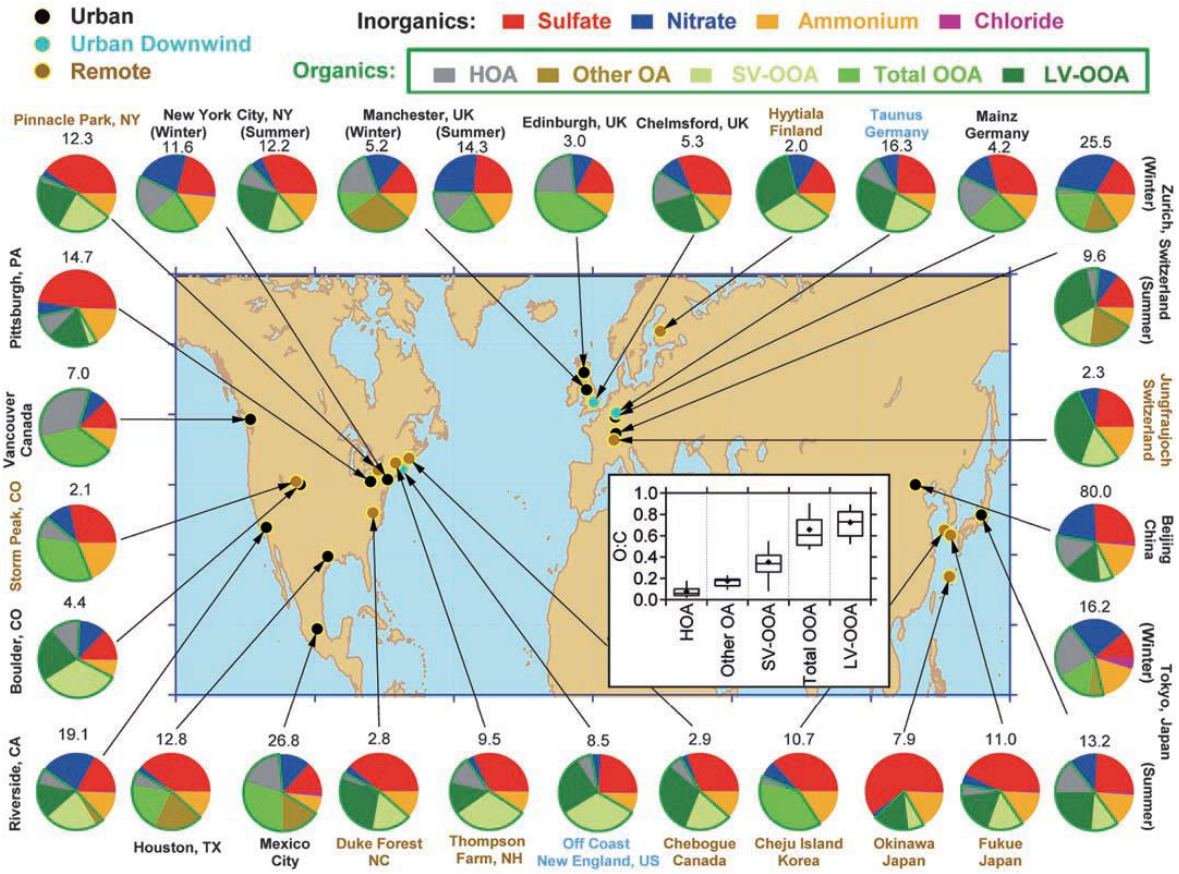

Figure 2.1: Total mass concentrations (in μg/m^3) and mass fractions of inorganic species and organic components in submicrometer aerosols measured at multiple surface locations in the Northern Hemisphere. From Jimenez, J.L. Canagaratna, M.R. Donahue, N. M., Prevot, A. S. H., Zhang, Q., Kroll, J. H., DeCarlo, P. F., Allan, J. D., Coe, H., Ng, N. L. and Aiken, A. C.: Evolution of Organic Aerosols in the Atmosphere, Science, 326(5959), 1525–1529, doi:10.1126/science.1180353, 2009. Reprinted with permission from AAAS.

2.2 Aerosol measurement facilities at IISER Mohali

Central Atmospheric Chemistry Facility (30.667^o N, 76.729^o E, 310 m a.m.s.l.) located inside the residential campus of IISER Mohali, Punjab, India houses instruments for measurement of ambient PM_{10}, $PM_{2.5}$ and Black carbon, along with many gaseous species and meteorological parameters. Sinha and co-workers (Sinha et al., 2014) describe the facility and the quality assurance procedures followed. IISER Mohali also provides the central Scanning Electron Microscopy facility, along with Energy- Dispersive X-ray Spectroscopy.

2.2.1 PM analyzers:

There are two separate instruments for measurement of mass concentration of ambient PM_{10} and $PM_{2.5}$. These instruments are collocated at a height of ~20 m agl along with other instruments in the monitoring station, called the Ambient Air Quality Station. They take continuous measurements 24x7, all year round. Both the instruments have been measuring and recording data since November 2011, with little history of down time. Both the instruments are based on the same radiometric principle of working, which is beta attenuation. A PM instrument consists of two parts- the inlet and the analyser. The analysers of both the PM instruments are identical – the Thermo Scientific Model 5014i Beta Continuous Particulate Monitor. The primary difference in the two instruments lies with the inlets.

Inlet: Both the instruments use cyclone and impactor combination- type inlets that segregate the particles based on the aerodynamic diameter (d_a) of the particles, using the principle of inertial separation (Figure 2.2). These inlets are made up of an alloy of aluminum, which is strong and chemically inert. The inlets are mounted at a height of ~20 m agl, on the roof top of the monitoring station. The inlets of both the instruments are same, with an additional part called PM2.5 sharp cut cyclone fitted in the PM2.5 inlet. Air is sucked in through two parallel horizontal plates at a flowrate of 16.67 litres per min (1000 litres per hour), with the help of a heavy- duty vacuum pump. As the air enters the inlet at an angle of ~ 30 degrees, only particles which have $d_a <= 15$ μm are able to enter with the air stream. The design of the next part is such that as the carrier gas with particles enters it, a cyclone is formed. Due to this action, particles with a $d_a >= 12$ μm stick to the walls of the cyclone cell and rest of the particles pass on to the next part through a wide orifice. Upon entering through the orifice, the particles encounter an impaction plate. Particles small enough, ($d_a <= 10$ μm) follow the streamlines of the airstream upwards and back down through three wide orifices into the next part, while larger particles collide with the impaction plate and are lost. If large water droplets are present in the sample, they will collide with the impaction plate and will be guided towards a glass bottle attached at the outside of the inlet at this stage. In case of inlet for PM_{10} monitor, sizing process ends here. In case of inlet for $PM_{2.5}$ monitor, there is an additional part for sizing, called $PM_{2.5}$ sharp cut cyclone, that separates $PM_{2.5}$ from PM_{10} particles. Upon segregation, PM_{10} and $PM_{2.5}$ particles pass onto their respective analysers, after passing through a heated segment of the inlet line. This helps to remove excess moisture from the particles and maintain the pre-set sample RH (generally ~40%). The analyser can control the sample RH by heating the inlet, depending upon the measured ambient RH and ambient temperature.

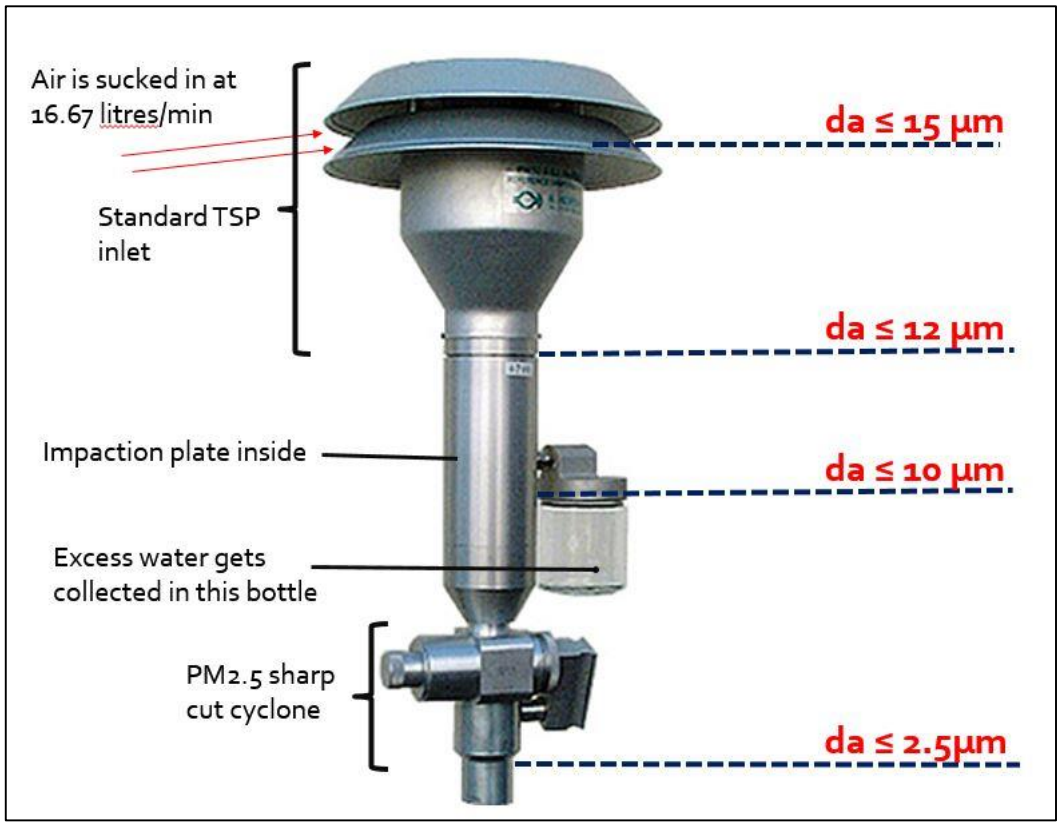

Figure 2.2: Basic mode of working of the impactor- type inlet for PM2.5 instrument

Analyser: Mass concentration of PM particles is measured using the radiometric principle of beta attenuation through a known area on a fibrous filter tape on which sample is collected. Thermo Scientific Model 5014i Beta Continuous Particulate Monitor is the model of analysers employed by the PM instruments at IISER Mohali Atmospheric Chemistry Facility. It has a detection limit of < 4µg/m^3, resolution of 0.1 µg/m^3, precision of 2.0 µg/m^3, accuracy of +- 5% and a data output rate of 1 second. Detection limit and uncertainty reduce if the data is recorded with a frequency of one minute. The uncertainty associated with the measured mass loading is < 8%. The key components of the analyser include:

(i) Proportional detector

(ii) Glass fibre filter tape

(iii) A vertical moving vacuum chamber plate

(iv) C-14 beta source with radioactivity < 100 µCi (or < 3.7 Mbq, which means 3.7 x 10^6 events of radiation emission per second)

After getting sized and passing through heated inlet, the particles enter the analyser through a radially insulated tube that joins the sampling tube to the collection chamber. The particles then get collected on a glass- fibre filter tape inside the analyser's combined sampling and detection

chamber (Figure 2.3) and form a circular spot on the tape. The filter tape spot is secured in place inside an optical bench, by the application of vacuum pressure. The mass signal for the spot is set to zero before the first measurement. C-14 beta source emits measured amount of beta particles and projects them through the spot from below. Upon passing through the spot, the intensity of beta rays decreases due to absorption of beta particles by the empty filter tape or the combination of the filter tape and the sample particles. This absorption is proportional to the mass of the sample. The proportional detector on the other side of the tape detects the change in intensity between two subsequent measurements and relays this signal to the electronic circuitry of the analyser, which applies fixed conversion formulae to determine the mass concentration of the sample deposited within this time span and convert the result to microgram per meter cube using the known flow rate through the system. This data is displayed on the analyser's display screen and stored in the instrument, and in computer hard drive. Mass deposited on the filter tape is calculated from a continuously integrated count rate. The sample keeps accumulating on the same spot for some time and continuous measurements are made. A fresh spot is introduced by an automatic filter change mechanism at least every 24 hours but more often when needed. Generally, the settings in these analysers at IISER Mohali is such that fresh spot is introduced every 8 hours or when the total mass concentration on the spot reaches 1500 $\mu g/m^3$, whichever happens earlier. The analyser's user console allows for changing these settings within certain limitations. The limit of mass concentration is set at 1500 $\mu g/m^3$ to reduce the damping effect on the beta ray intensity, due to accumulation of excess sample on the spot.

Since the EPA reference method 201A is standardized towards measuring dry aerosol mass, the aerosol is dried to 40% RH. However, drying involves certain trade-offs. In the Thermo Scientific Model 5014i Beta Continuous Particulate Monitor, drying is accomplished by heating the sample inlet, which reduces the positive artifact due to the water in liquid aerosol particles adding to the mass but heating does introduce negative artifacts (loss of ammonium nitrate and potentially other semi-volatile particles) as a consequence of the temperature change. All drying methods other than conditioning in a desiccator containing anhydrous calcium sulfate at <40% RH and 25°C for 24 hours come with certain tradeoffs. For single Nafion dryers, losses of particles are minor and volatile particles are conserved, but flow rate constraints do not allow operation at >1 lpm flow rate. Moreover, dry particle free purge air with a low dew point (-20°C) for the other side of the membrane must be available 24/7. Nafion dryer bundles allow higher flow rates but have high losses for Aitken mode PM due to diffusion and for PM >1 μm particles due to impaction losses. Silica gel dryers have low losses and are artefact free, but are difficult to maintain under the prevalent climatic conditions. Firstly, two dryers are needed. One that dries the aerosol to <40% outside at ambient temperature (which can reach 45°C) to prevent condensation inside the line

which would otherwise happen as soon as the air enters the container. A second dryer would have to be mounted inside the container to again dry the air after it cooled to 25°C, because after a temperature drop of ~10-20°C the air again has an RH >>40%. For flow rates of 16.7 lpm, silica gel dryers need to be changed multiple times per day in monsoon season and it is impossible to regenerate the gel fast enough without an unreasonable number of ovens, so approximately 1-2 months' worth of silica gel must be stocked to keep the dryers operational. Continuous in-line regeneration of silica gel dryers requires at least double the number of dryers and large quantities of dry particle free air with -20°C to -40°C dewpoint. It is not even clear whether the column can be regenerated fast enough under the prevalent climatic conditions during monsoon season. While heating above ambient can cause negative artefacts for volatile species, cooling the air to container conditions without removing the gas phaseNH_3, HCl and HNO_3 could introduce negative artefacts for the same species. Therefore, considering various practical constraint, and cost effectiveness drying by heating is the most feasible compromise. However, it must be understood that the PM_{10} and $PM_{2.5}$ mass reported presents the upper limit to the true mass and negative artefacts are possible.

Additionally, in order to avoid negative mass artifacts from natural radiation, the proportional detector is sensitive to natural alpha activity of the aerosol passing through the sampling system. An additional alpha count rate is measured to detect the presence of Radon gas and to infer the daughter nuclides of Radon gas. The potential error from Radon gas interference may be as high as actual particle concentrations. The daughter nuclides create a small beta emission, which can interfere with the actual beta signal and make the detector believe that the beta count rate is higher, apparently causing less sample mass to be detected. Therefore, by measuring the natural alpha activity due to Radon gas, the proportional beta interference from the daughter nuclide emissions are subtracted from the count rate to provide a refined mass measurement. This procedure further allows the analyser to provide a more stable reading at lower ambient particulate concentrations compared to other similar methods.

The PM instruments require regular maintenance and service, which is done by members of the Aerosol Research Group of IISER Mohali. This includes: Inlet system cleaning every one month, mass calibration every six months, new filter tape installation, and some unforeseen service requirements. Calibration is done using Thermo- Fisher provided mass foil calibration kits, which are NIST- traceable and highly accurate.

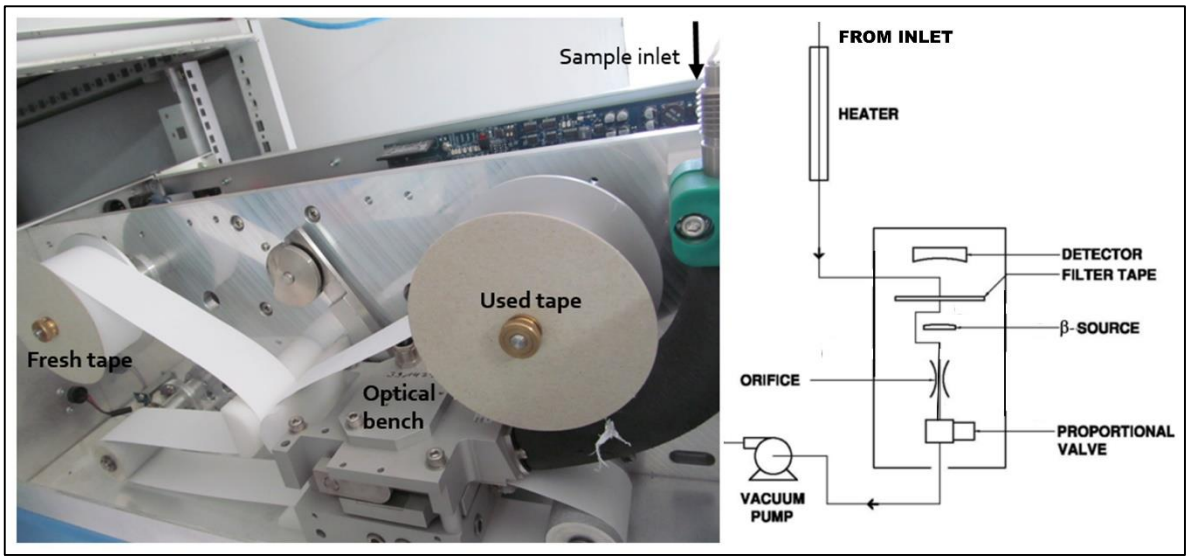

Figure 2.3: Left: Inside view of PM analyser's collection and measurement chamber. Right: Schematic of sample flow and key components of PM analyser (Source: Thermo Fisher Scientific Model 5014i User's manual).

2.2.2 Aethalometer:

Ambient BC is measured using an Aethalometer (AE 42, Magee Scientific), a portable seven-wavelength version, at IISER Mohali. It measures at wavelengths of 370, 470, 520, 590, 660, 880, and 950 nm to calculate absorption Angstrom exponent (α_{abs}) and BC mass loading. The instrument has been functional since April 2013 till date, with little downtime. An Aethalometer measures concentration of optically absorbing black carbon present in the ambient air, in real-time, using the method of optical attenuation due to broad- spectrum absorption of light by BC. The AE- 42 measures and outputs the BC mass loading value every 5 minutes. Input to the Aethalometer is attached to an inlet line, which carries a stream of air containing ambient $PM_{2.5}$ particles, which have been filtered using a $PM_{2.5}$ cut-off impactor- type inlet. Ambient air is sucked in at a flowrate of 4 litres per min through the inlet and is dried using two silica gel scrubbers- one fitted outside and the other fitted inside the air- conditioned container. The particles in the air stream get collected on a quartz fibre filter tape and form a spot. Vacuum pressure applied under the tape keeps it secure in a position inside the optical head. Light of seven different wavelengths is shone on the tape one by one, from above (Figure 2.4). A beam splitter splits the incoming beam of light into two beams- Reference beam, which falls on the clean part of the tape and Sample Beam, which falls on the sample spot. Reference beam accounts for changes in the light intensity of the lamps and sensing beam accounts for the change in sample loading on the spot. A measurement of the intensity of light passing through the two areas of the filter is made once before the sample gets collected on the spot, at time t0, and then after the sample gets accumulated, at

times t, t+1, t+2, and so on till a new spot is introduced. Change in attenuation (ATN) of light signal (SB) transmitted through the sample is measured by two photodetectors [RZ (Reference zero) and SZ (Sensing Zero) measurements are also done when lamps are off, to account for any 'dark response signal' of the detectors.] Attenuation is the change in intensity of light signal due to absorption + scattering by the sample. According to the measurement principle of this instrument, this quantity is linearly proportional to the mass of BC in the filter deposit:

$$ATN = \sigma * [BC] \quad (14)$$

where, σ is wavelength- dependent absorption cross- section. Aethalometer assumes that all changes in attenuation between times t and t+1 is only due to absorption by sample. According to Beer- Lambert's law:

$$\text{Absorption} = \ln(I_t/I_{t+1}) \quad (15)$$

In reality, it is the absorption plus scattering by the particles that causes change in attenuation. In addition to this, attenuation may also be caused by wet aerosols present in the sample. In Aethalometer, a significant part of the attenuation is caused by scattering due to fibers of the filter, which the SB helps to account for. Spot change (consumes 15 minutes) occurs whenever absolute value of attenuation $\ln(I_{\text{empty filter}}/I_t)$= 1.50.

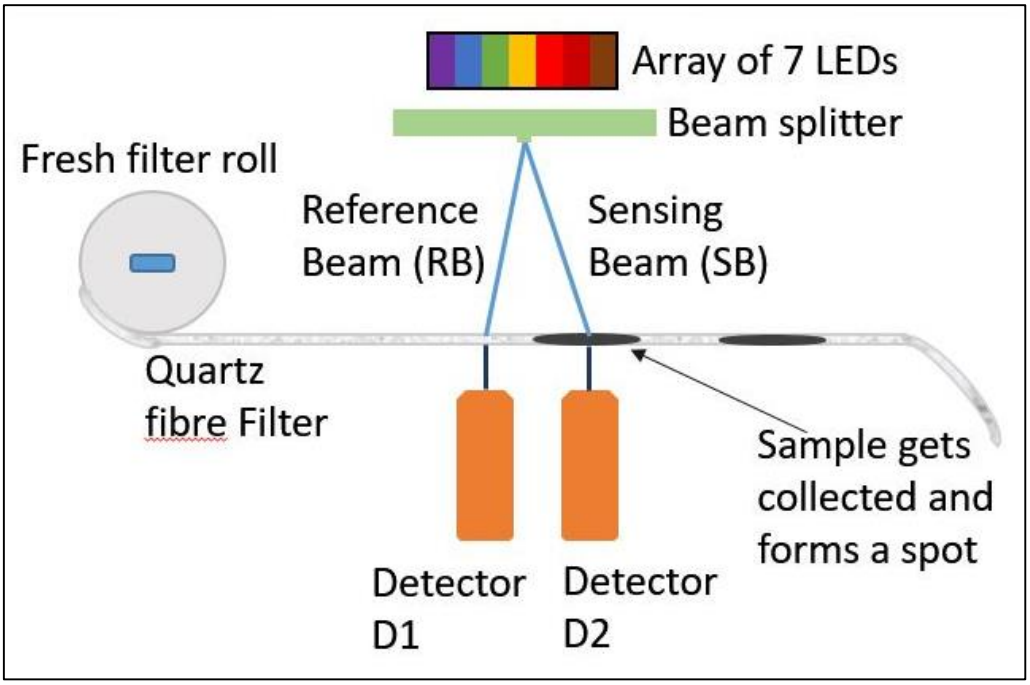

Figure 2.4: Schematic of Magee Scientific Aethalometer Model AE- 42

In Aethalometer, light extinction is converted to mass loading using mass absorption cross section (MAC), which is optical cross section per mass in m^2/g. A fixed MAC (wavelength, λ - dependent) is used for this conversion, although in the atmosphere, MAC of BC varies. This model uses either

the Standard Magee BC calibration (MAC = 14625/λ) or Harvard TOR- EC calibration (MAC = 11115/ λ) for calculating the BC mass loading. Finally, BC mass loading at 7 different wavelengths of light is output on the display screen and relayed to the computer for storage.

Although the electronics are very stable, the instrument's measurement depends on determining extremely small changes in intensity of the optical signals. As a precaution, the electronics area is thermally insulated and its temperature is actively stabilized by a thermistor-controlled circuit. This minimizes any possible effects of ambient temperature fluctuations. Maintenance of the instrument includes regular cleaning of inlet and inlet lines, installation of fresh tape, changing of hydrated silica gel, timely checks on flowrate, cleaning of optical head.

In case of this instrument, the following three things are important to point out:

Data correction: Data from optical instruments that use filter- based measurements like Aethalometer, need to be corrected by application of site- specific corrections as the attenuation of light is not caused purely due to absorption by sample particles, and factors like scattering due to aerosol particles, absorption and scattering due to wet particles, scattering due to fibres of the filter tape have significant influence on the measurement. In particular, 'scattering correction', which accounts for change in attenuation due to scattering aerosols embedded in the filter and 'filter- loading correction', which decreases the discrepancy caused by increase in attenuation due to increased optical path length as a result of multiple scattering by filter fibers, are applied. Chapter 3 provides detail regarding the correction procedures applied to data from the Aethalometer installed at IISER Mohali.

Weingartner and co- workers (Weingartner et al., 2003), Arnott and co-workers (Arnott et al., 2005), Schmid and co- workers (Schmid et al., 2006), Virkkula and co-workers (Virkkula et al., 2007), and Collaud Coen and co-workers (Collaud Coen et al., 2010) have proposed methods for correction of BC data from Aethalometer to rid the data of artifacts of one or all kinds. These published correction methods have taken into account either results of chamber experiments involving extinction and scattering coefficient measurements, or comparison with PAS (Collaud Coen et al., 2010). Most of the correction procedures have been built upon the previously existing correction methods. With regard to the choice of procedures applied to correct data from the Aethalometer installed at IISER Mohali, there have been certain considerations. The Weingartner correction with fixed coefficients is poorly suited for the type of environment witnessed in Mohali, where the correction algorithm needs to accommodate events as diverse as massive biomass-burning plumes (BC_{eq} > 50 μg/m3), dust storms ($PM_{2.5}$ > 1500 μg/m3), and high-mass loadings of mixed organic and inorganic aerosol ($PM_{2.5}$ > 200 μg/m3). Weingartner and co- workers had proposed an empirical correction R_W for the attenuation effect due to the filter-loading and determined the calibration constant C_{ref} for different aerosol types produced in the AIDA aerosol

chamber (at FZ Karlsruhe, Germany) to correct for the multiple scattering in the filter matrix. The resulting nth absorption coefficient $b_{abs,n}$ is given by:

$$b_{abs,n}(\lambda) = \frac{b_{ATN,n}}{C_{ref} \cdot R_{\omega,n}} = \frac{b_{ATN,n}}{(C_{ref}) \cdot \left[\left(\frac{1}{f} - 1\right) \cdot \frac{\ln(ATN_n) - \ln(10)}{\ln(50) - \ln(10)} + 1\right]} \quad (16)$$

where C_{ref} is determined by first correcting b_{ATN} for the filter-loading correction and then comparing it with the absorption coefficient measured simultaneously with a reference instrument ($b_{abs,ref}$). Since the Weingartner filter- loading correction R_W takes ATN=10% as a reference point, C_{ref} relates in this case to ATN=10%:

$$C_{ref} = \frac{b_{ATN}}{R_W . b_{abs,ref}} \quad (17)$$

The parameter f(λ) characterizes the slope between $b_{ATN,n}$ and $\ln(ATN_n)$ and parameterizes the filter-loading correction R_w. Weingartner and co- workers also determined f values for different aerosol types.

Arnott and co-workers had proposed a correction procedure, which includes an explicit scattering correction factor ($-\alpha \cdot b_{scat}$). The scattering coefficient b_{scat} weighted by the α values is subtracted from b_{ATN} to correct for the scattering artifact. The Arnott filter-loading correction R_A is derived from multiple scattering theory, which shows that the exponential behavior of light absorption in the strong multiple scattering limit scales as the square root of the total absorption optical depth. The corrected $b_{abs,n}$ is given by:

$$b_{abs,n}(\lambda) = \frac{b_{ATN,n} - \alpha \cdot b_{scat,n}}{C_{ref} \cdot R_{A,n}} = \frac{b_{ATN,n} - \alpha \cdot b_{scat,n}}{(C_{ref})} \sqrt{1 + \frac{\left(\frac{V.\Delta t}{A}\right) \cdot \sum_{i=1}^{n-1} b_{abs,i}}{\tau_{a,fx}}} \quad (18)$$

$$\alpha(\lambda) = \beta_{scat,non-abs}^{d-1} \cdot c \cdot \lambda^{-\alpha_{scat,non-abs} \cdot (d-1)} \quad (19)$$

where, V is the volumetric flow rate, A is the area of the sample spot, Δt is the time interval during which particles get embedded in the filter, n is the nth measure of the aerosol attenuation coefficient of the filtered aerosol particles, $\tau_{a,fx}(\lambda)$ is the filter absorption optical depth for the filter fraction x that as particles embedded in it. C_{ref} can be obtained by comparison between aethalometer and PAS absorption coefficients. c and d are obtained from the measured non- zero b_{ATN} in the presence of a non-absorbing aerosol and correspond the following relation:

$$b_{ATN} = c \cdot b_{scat,non-abs}^{d} \quad (20)$$

$b_{scat,non-abs}$ and $\alpha_{scat,non-abs}$ can be calculated as:

$$b_{scat,non-abs} = \beta_{scat,non-abs}^{d-1} \cdot \lambda^{-\alpha_{scat,non-abs} \cdot (d-1)} \quad (21)$$

The correction algorithm proposed by Virkkula and co- workers, which assumes that the last three attenuation values measured on the filter spot, i, and the first three attenuation values measured on the next filter spot, i+1, should be equal, fails during biomass-burning plumes when large changes of BC_{eq} mass loadings can occur during spot changes, as observed in Mohali. It also assumes that the values measured on lightly loaded filters represents the closest to the real concentrations. Following is their proposed correction R_v:

$$b_{ATN,R\_corrected,n} = \frac{b_{ATN,n}}{R_V} = (1 + k_i . ATN) . \mathrm{b}_{ATN,n} \tag{22}$$

$$k_i = \frac{BC_0(t_{i+1,first}) - BC_0(t_{i,last})}{ATN(t_{i,last}).BC_0(t_{i,last}) - ATN(t_{i+1,first}).BC_0(t_{i+1,first})} \tag{23}$$

where $t_{i,last}$ is the time of the last measurement on the filter spot i and $t_{i+1,first}$ is the time of the first measurement on the next filter spot i+1. A k_i value is therefore determined for each filter spot and applied to all n measurements on the ith filter spot. The scattering correction has been set to zero for this method and multiple scattering correction has been omitted completely.

The correction algorithm proposed by Schmid and co-workers, for the SMOCC campaign in the Amazon basin, which includes filter loading correction, multiple scattering correction and a scattering correction term that depends on the single scattering albedo of the aerosol, has been found to be most suitable in Mohali's complex environment. The precision error is calculated using the reference beam stability on a single spot for calculated angstrom exponent values. For BC_{eq} mass values, the total uncertainty is a composite of uncertainty associated with the measurement of attenuation at different wavelengths and the uncertainty of the flow controller (2%). The systematic uncertainty arising from the choice of the appropriate MAC values in the uncertainty calculation is not considered. The following has been accepted as the standard procedure for correction of BC data from the aethalometer installed at IISER Mohali:

Schmid correction is applied to the 5- minute time resolution aethalometer raw data to calculate BC_{eq}.

$$\mathrm{BC}_{eq} = \frac{b_{abs,n}\,(880nm)}{MAC(880nm)} \tag{24}$$

where, $b_{abs}(880)$ is absorption coefficient and MAC_{880} is mass absorption cross-section, both measured at 880 nm wavelength.

$b_{abs,n}(\lambda)$ is calculated as:

$$b_{abs,n}(\lambda) = \frac{b_{ATN,n}}{(C_{ref}+C_{scat,n})\cdot R_{\omega,n}} = \frac{b_{ATN,n}}{\left(C_{ref}+a_n\cdot\frac{\omega_{0,n}}{1-\omega_{0,n}}\right)\cdot\left[\left(\frac{1}{m\cdot(1-\omega_{0,n})+1}-1\right)\cdot\frac{\ln(ATN_n)-\ln(10)}{\ln(50)-\ln(10)}+1\right]} \quad (25)$$

with

$$a_n = \beta_{scat,n}^{d-1}\cdot c\cdot\lambda^{-\alpha_{scat,n}\cdot(d-1)} \quad (26)$$

where, d=0.564, c = 0.32910^{-3} [m^{-1}] and $\beta_{scat,n}^{d-1}$=0.4471^{-1} [m^{-1}] have been taken from Arnott and co-workers (Arnott et al., 2005), and m=0.92 and C_{ref} =5.2 have been determined such that the slope of the corrected b_{abs} as a function of the ATN is in the range of 0 ± 2 x 10^{-8} for all wavelengths. (Figure 2.5 left & Figure 2.6). Note that C_{ref} =5.2 is similar to the value reported by Schmid and co-workers (Schmid et al., 2006) for deforestation fires during the SMOCC campaign in the AMAZON basin. Figure 2.7 shows a sequence of filter spot changes at times of relatively stable BC_{eq} mass loadings for each of the biomass burning types to illustrate that the correction algorithm works well in all cases.

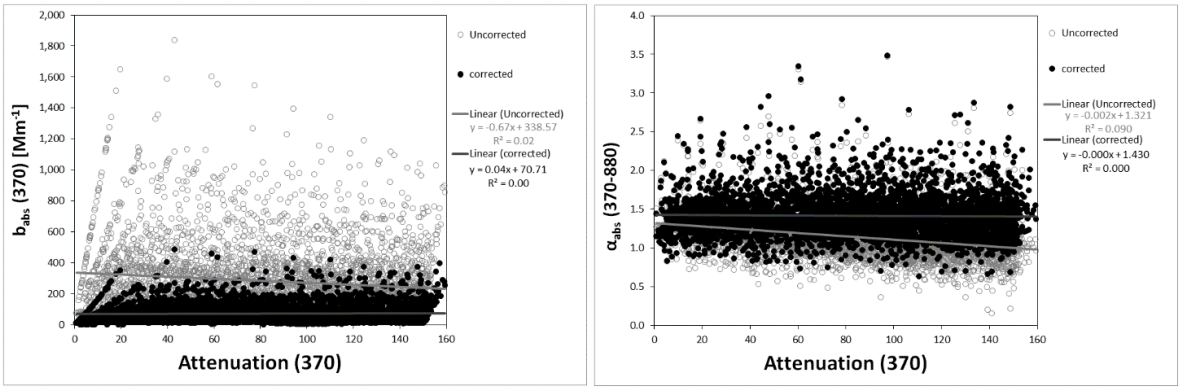

Figure 2.5: Left panel: absorption coefficient ($b_{abs}370$) values before applying correction (gray circles) and after applying correction (black dots) plotted against optical attenuation signal at the 370 nm channel. Linear fit equations and R2 values for b_{abs370} vs ATN_{370} are shown in gray for uncorrected and in black for corrected. Right panel: angstrom exponent ($\alpha_{abs}370-880$) before applying correction (gray circles) and after applying correction (black dots) against the optical attenuation signal of the 370 nm channel. Linear-fit equations and R^2 values for $\alpha_{abs}370-880$ vs attenuation at 370 nm are shown in gray for uncorrected and in black for corrected. Corrected absorption coefficient values and corrected angstrom exponent values do not exhibit any dependence on the optical attenuation values, unlike the uncorrected ones.

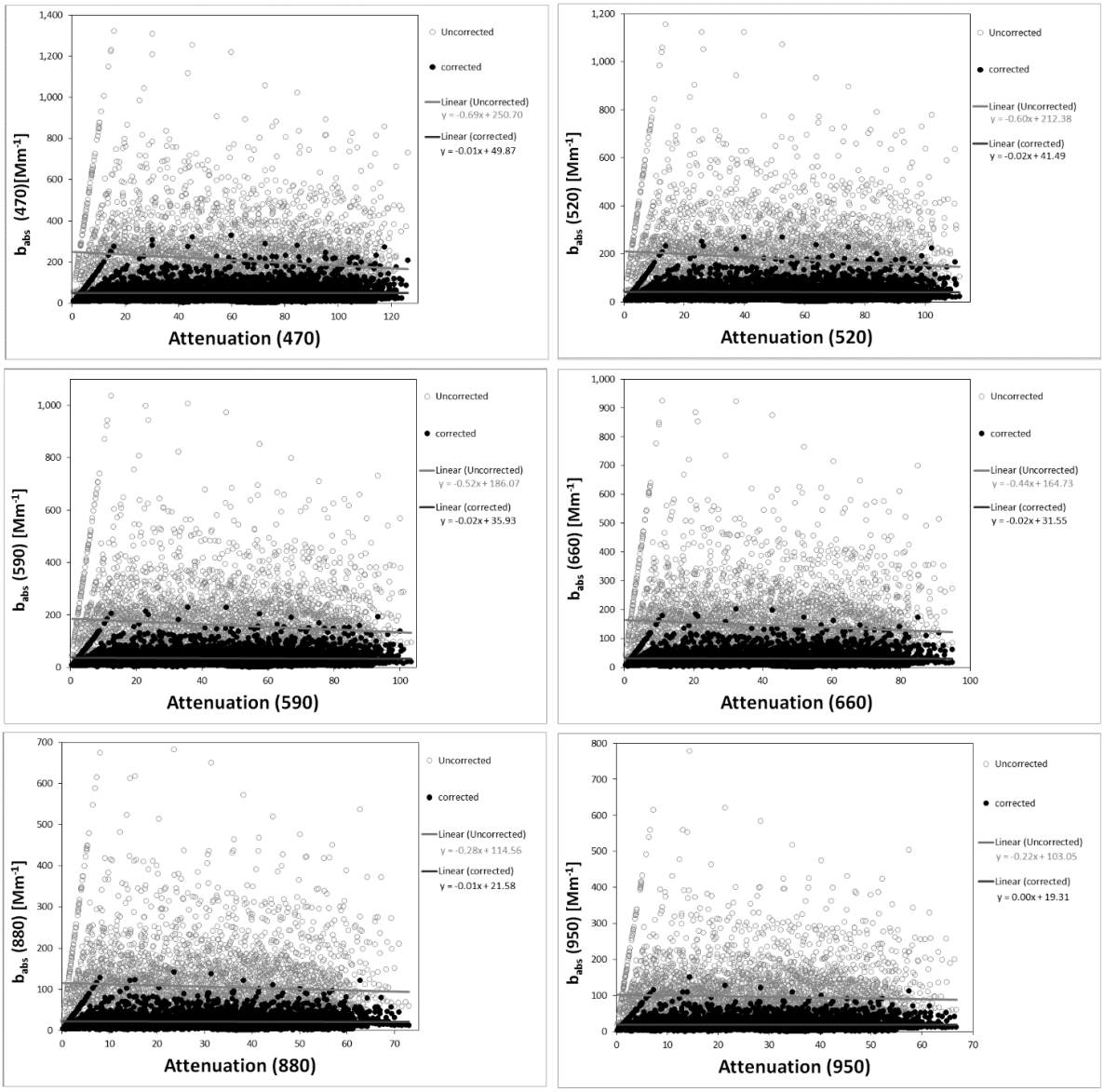

Figure 2.6: Scatter plots showing absorption coefficient (b_{abs}) values before applying correction (grey circles) and after applying correction (black dots) plotted against optical attenuation signal for 6 different wavelength channels- 470nm, 520nm, 590nm, 660nm, 880nm, 950nm . For each plot, linear fit equations and R^2 values for b_{abs} vs. attenuation are shown in grey for uncorrected and in black for corrected.

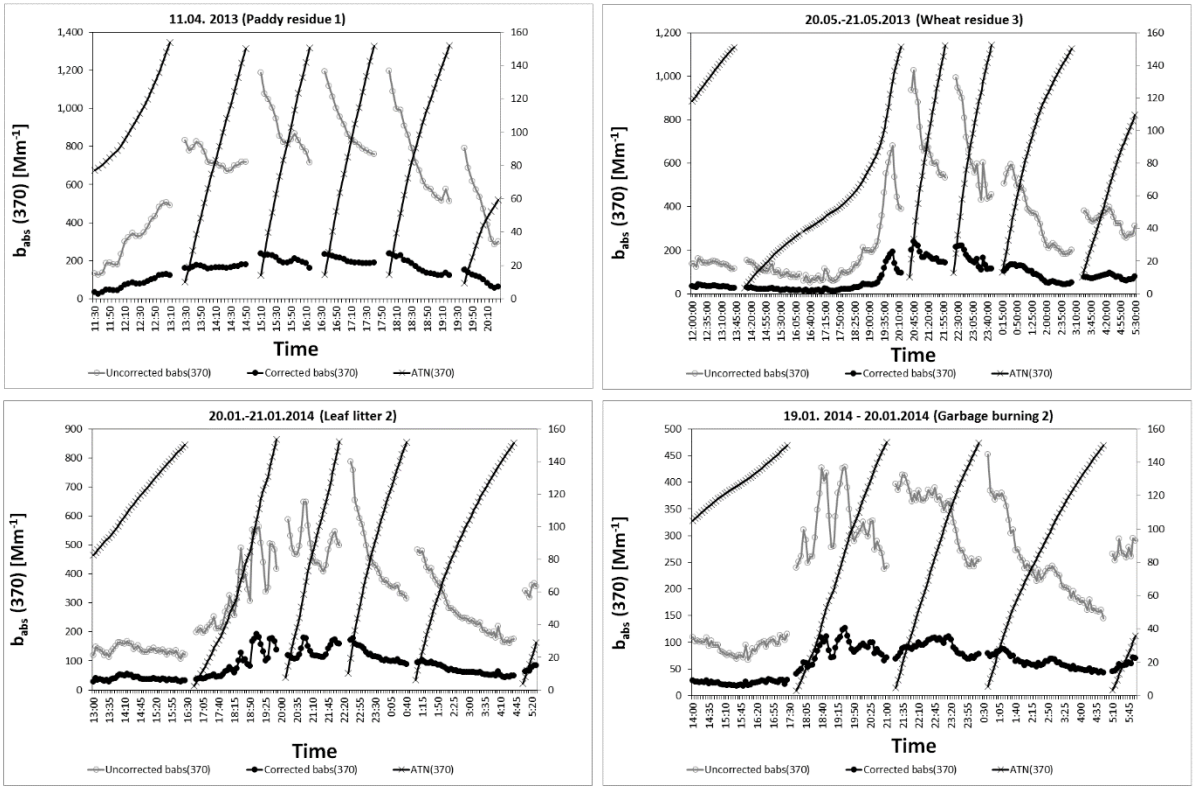

Figure 2.7: Variation of attenuation ATN (diagonal crosses), absorption coefficients b_{abs}(370 nm)-uncorrected (grey circles) and corrected (black dots) with consecutive spot changes over time for a paddy- residue burning event (top left panel), a wheat- residue burning event (top right panel), a leaf-litter burning event (bottom left panel) and a garbage burning event (bottom right panel).

In the absence of simultaneous scattering measurements, the single scattering albedo $\omega_{0,n}$ of aerosol for each data point has been estimated using the measured aerosol mass ($PM_{2.5}$) and the uncorrected $BC_{eq\text{-}880}$ as a first order estimate of the BC_{eq} mass. SEM investigation of the used aethalometer filter tapes for a few diverse plumes recorded in Mohali (Figure 2.8) revealed that in the fresh plumes, only two to three types of aerosol particles dominate the PM2.5 mass loadings: black carbon, primary organic matter (POA), and tar balls. This is typical for biomass-burning plumes that are fresh or moderately aged (Pósfai et al., 2003). Therefore, the single scattering albedo $\omega_{0,n}$ is calculated using the following set of optical properties: for the non- BC $PM_{2.5}$ aerosol, a mass scattering cross section (MSC) of 6 m²/g at 550 nm is used, which has been reported for times when tar ball from biomass combustion dominated aerosol plumes during the Yosemite aerosol characterization experiment (Hand et al., 2005). For black carbon, a mass scattering cross section (MSC_{BC}) of 2 m²/g is applied to the uncorrected $BC_{eq\text{-}880}$ black carbon (Bond et al., 2013; Pósfai and Buseck, 2010) and the mass absorption cross section (MAC) from the Harvard TOR-

EC calibration is applied to the uncorrected $BC_{eq\text{-}880}$ to estimate the single- scattering albedo of the aerosol. An effective radius of 300 nm for the aerosol size distribution is applied while determining the MSC for each wavelength on the basis of scanning electron microscopy (SEM) images of the used aethalometer tape (Figure 2.8). A refractive index of m = 1.84 – 0.21i for tar balls and m= 1.95 – 0.79i for black carbon has been used to calculate the MSC for each of the seven aethalometer wavelengths. The resulting coefficients then amount to MSC_{370} = 4.7 m^2/g and MSC_{880} = 8.7 m^2/g for tar balls and MSC_{370} = 2.0 m^2/g and MSC_{880} = 1.8 m^2/g for black carbon, respectively.

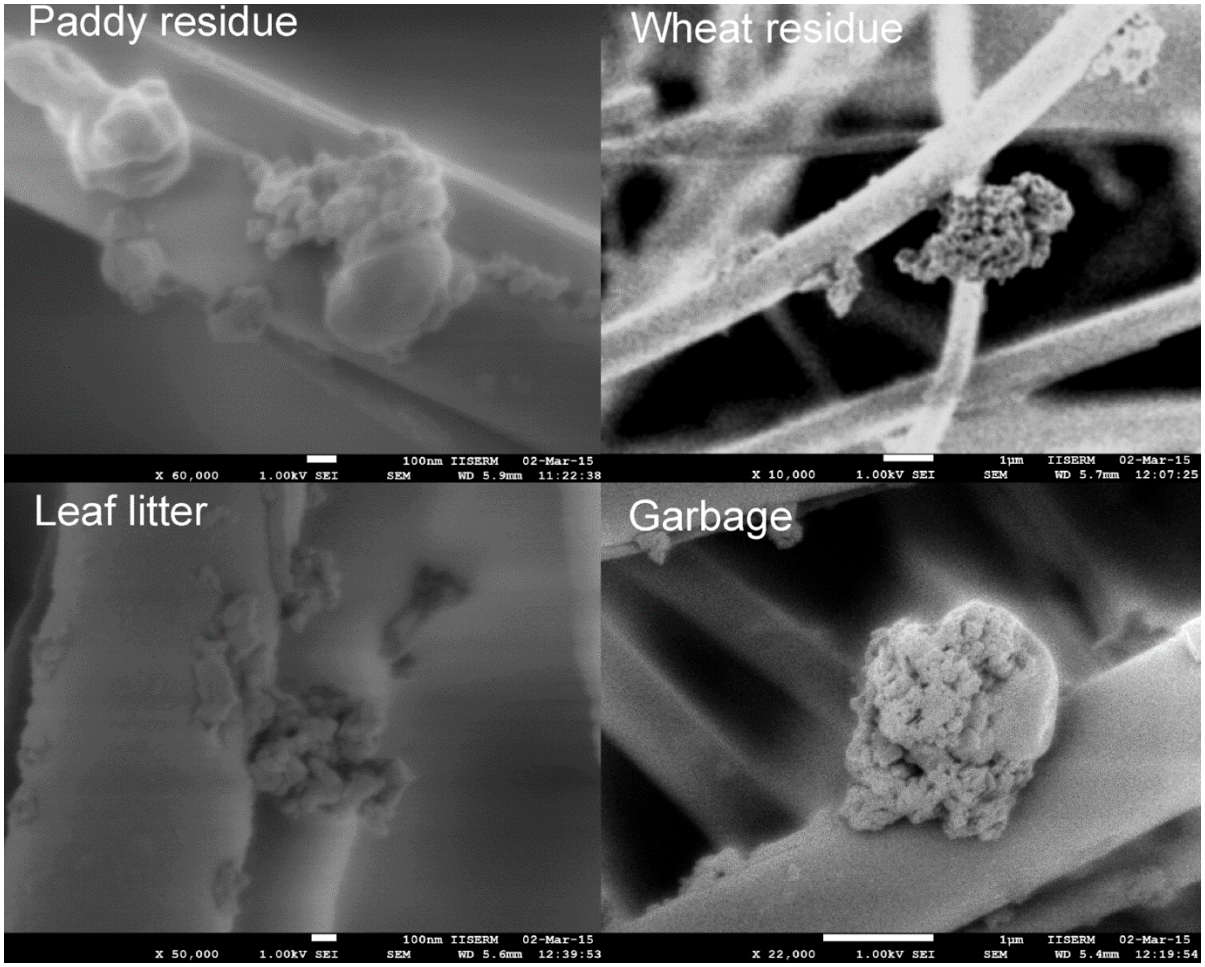

Figure 2.8: SEM images of particles collected on Aethalometer filter tape during a paddy-residue-burning event (top left), a wheat-residue- burning event (top right), a leaf-litter-burning event (bottom left), and a garbage-burning event (bottom right). All scale bars are 1 µm.

The angstrom exponent of the absorbing fraction after filter loading and scattering correction is calculated as:

$$\alpha_{abs(370-880)} = -\frac{ln\frac{babs\,(370nm)}{babs\,(880nm)}}{ln\frac{370}{880}} \quad (27)$$

After correction, the angstrom exponent no longer varies as a function of filter loading (Figure 2.5 right). The angstrom exponent calculated using the wavelength pair 370 and 880 nm: $\alpha_{abs(370-880)}$ correlates linearly with the angstrom exponent calculated using the wavelength pairs 370 and 950 nm ($\alpha_{abs(370-950)}$), and 470 and 950 nm ($\alpha_{abs(470-950)}$), respectively with a slope of 1.00 and 1.04 and R^2 of 0.8 and 0.6 respectively, indicating that there is no systematic bias introduced by any of the lamps.

Concept of Equivalent BC: In reality, Aethalometer measures equivalent BC mass, and not purely BC mass, due to the following reasons. Firstly, the sample analysed by Aethalometer does not include only BC. It includes all $PM_{2.5}$ that could make it through the inlet. Secondly, there are not only purely absorbing particles in the sample, there may be particles which are primarily scattering in nature. Both the above points mean that it isn't entirely the absorbing BC that is being measured; along with it, other absorbing and scattering $PM_{2.5}$ particles are being analysed too, without any discretion. The concept of equivalent BC (BC_{eq}) becomes significant here. BC_{eq} is the mass of ideal (graphitic) BC (elemental carbon EC) with defined optical properties (MAC = 11115/λ for the Harvard TOR-EC calibration) that, upon deposition on the Aethalometer filter tape, would cause equal optical attenuation of light at a given wavelength as the actual PM2.5 aerosol deposited (Garg et al., 2016).

It is also more justifiable to use the term BC_{eq} for radiative transfer modelling, as it is important to know how much absorption is taking place in the atmosphere, not how much BC in terms of true mass is present. Climate models need b_{abs} and b_{sca} (absorption and scattering coefficients, respectively, in m^{-1}), which signify the amount of particulate absorption and scattering in the atmosphere. These b_{abs} and b_{sca} coefficients are calculated by these models with the help of modelled mass loading (obtained from the emission inventories) and MAC (Mass Absorption Cross-section), MSC (Mass Scattering Cross- section). BC MAC_{550} values used in global models range from: 2.3 to 18 m^2g^{-1} (Jacobson, 2012; Koch et al., 2009), however, each model uses a fixed MAC due to computational constraints. In the real world MAC changes as a function of BC source, mixing state and aging. Validation of the model parameterization requires simultaneous measurements of BC_{eq} and EC, yet any single MAC can never adequately represent the complex real world situation. While some recent models have already bifurcated carbonaceous aerosol from fossil fuel and from biomass burning (Figure 1.1 and Figure 2.9) and consequently can assign different MAC to both, MAC changes associated with changes in mixing state or aging are still not represented. If BC_{eq}, instead of "accurate" EC mass is used for validating the emission inventories, then by using the same MAC_{550} value as was used for estimating the BC_{eq} mass in the

source sampling in the model for calculating the radiative forcing due to the BC_{eq}, results in a situation where errors cancel out. This means that the model need not treat a large number different sources and/or technology levels separately just because the BC emitted from different sources in the real world has different MAC's.

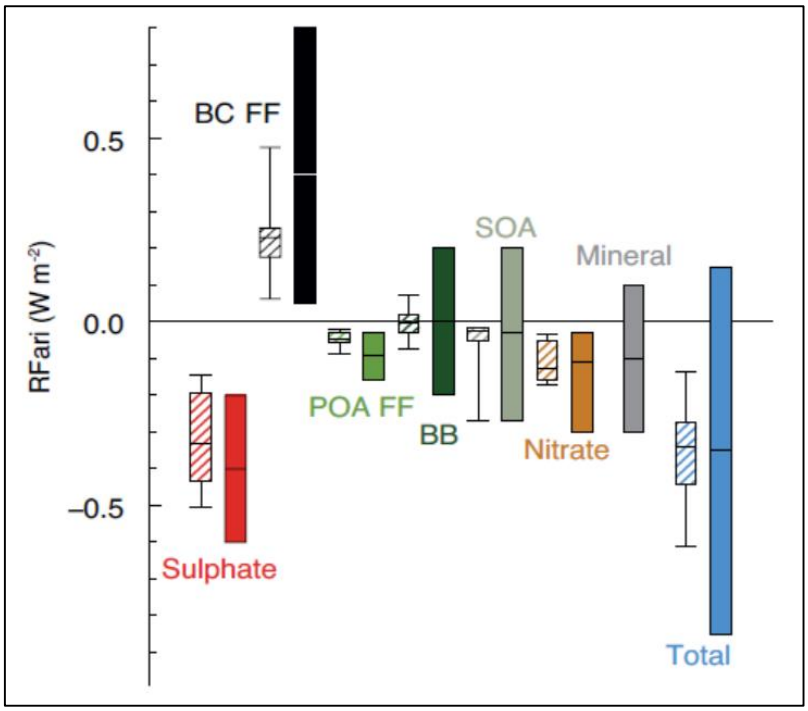

Figure 2.9: Annual mean top of the atmosphere radiative forcing due to aerosol– radiation interactions (RFari, in W m^{-2}) due to different anthropogenic aerosol types, for the 1750–2010 period. Hatched whisker boxes show median (line), 5th to 95th percentile ranges (box) and min/max values (whiskers) from AeroCom II models (Myhre et al., 2013) corrected for the 1750–2010 period. Solid coloured boxes show the AR5 best estimates and 90% uncertainty ranges. BC FF is for black carbon from fossil fuel and biofuel, POA FF is for primary organic aerosol from fossil fuel and biofuel, BB is for biomass burning aerosols and SOA is for secondary organic aerosols. Reproduced with permission from Boucher et al. (Boucher, O., Randall, D., Artaxo, P., Bretherton, C., Feingold, G., Forster, P., Kerminen, V.-M., Kondo, Y., Liao, H., Lohmann, U., Rasch, P., Satheesh, S. K., Sherwood, S., Stevens, B. and Zhang, X.-Y.: Clouds and Aerosols, in Climate Change 2013: The Physical Science Basis. Contribution of Working Group I to the Fifth Assessment Report of the Intergovernmental Panel on Climate Change, edited by T. F. Stocker, D. Qin, G.-K. Plattner, M. Tignor, S. K. Allen, J. Boschung, A. Nauels, Y. Xia, V. Bex, and P. M. Midgley, Cambridge University Press, Cambridge, United Kingdom and New york, NY, USA., 2013), Figure 7.18.

The correct BC mass loading out of the seven values: The decision of using a BC mass loading value out of the seven values, depends on the requirement and application of the data. Generally, while talking of purely BC mass loading, the minimum value out of the seven values is used, which is the BC_{880} value most of the times. As an example: If sample has BC + water + PAHs only, then UV channel shows higher BC due to absorption by PAHs, IR channels (950 nm) show higher BC due to absorption by water and other channels will show similar-to-each other values of BC, which will be less than BC(UV) and BC(IR). In such a case, the nearly correct BC mass loading will be output at the channels other than the UV and IR, as that would be the maximum mass equivalent of BC that is present in the mixture of particles in the sample. It is true that in an ideal world water should not be present in aerosol dried to ~10% RH, however, it is known that mixtures of organic aerosols and inorganic aerosols display delayed drying behaviour (Martin et al. 2012).

2.2.3 Scanning Electron Microscope and Energy- Dispersive X-ray Spectrosopy

Scanning Electron Microscopy (SEM) technique is used to obtain images of a sample at a magnification of several thousand times, by scanning the specimen with a high-energy beam of electrons in a raster pattern. It enables one to clearly observe even small specimen of nanometer-scale sizes, which cannot be observed under optical microscopes. The SEM at IISER Mohali is a JSM 7600F Field Emission Scanning Electron Microscope manufactured by Jeol Ltd., Japan. In SEM, the electrons interact with the atoms in the sample, producing signals that contain information about the sample's surface topography, composition, and morphology. Many signals, like secondary electrons, backscattered electrons, cathodoluminescence, characteristic x-ray radiation, phonons (heat) are produced upon this interaction. Following signals are the most important of these:

(i) **Secondary electrons**: Detection of these electrons provides information about the topography of the specimen being observed. Secondary electrons are produced when an incident electron excites an electron in the sample and loses some of its energy in the process. The excited electron moves towards the surface of the sample undergoing elastic and inelastic collisions until it reaches the surface. Here it can escape if its energy exceeds the amount of energy needed to remove electrons from the surface of a material. To increase the number of secondary electrons that will be emitted from the sample, a non-conductive specimen is often coated with a conductive material. The mean free path length of secondary electrons in many heavy, metal containing materials is ~10 nm, but in light materials it can be several 100 nm. Thus, although electrons are generated throughout the region excited by the incident beam, only those electrons that

originate at a shallow depth in the sample escape to be detected as secondary electrons. This volume of production is very small compared with BSE (Back- scattered electrons) and X-rays. Therefore, the resolution using SE is better than either of these. The shallow depth of production of detected secondary electrons makes them very sensitive to topography and they are used for scanning electron microscopy (SEM). Secondary electrons can be detected with a side mounted detector, towards which electrons are accelerated with a high acceleration potential. In this case all electrons exiting the sample are detected, even if the residual kinetic energy after passing into the vacuum is small or the momentum is into a direction away from the detector. An alternate detector can also be mounted inside or next to the lens and is operated without using a strong acceleration voltage. Such an SEI or in-lens detector detects only electrons which had sufficient momentum into the right direction upon existing the sample and may also detect some backscattered electrons. It, therefore, provides a pseudo atomic number contrast overplayed on a secondary electron image. In the context of imaging aerosol, the main advantage of the SEI detector is, that it has much less image noise compared to the BSE detector and can depict small objects << 100 nm in size.

(ii) **Backscattered electrons:** Detecting the backscattered electron (BSE) enables one to obtain a contrast image, depending on differences in the composition. BSEs are high energy primary electrons that suffer large angle (> 90°) scattering and re-emerge from the entry surface of a specimen. Chemical elements that have a high atomic number (high positive load of the atomic core) produce more back- scattered electrons than the ones that have a low atomic number. The areas of the sample with a high atomic number will thus look whiter than the ones with a low atomic number. Most BSE have energies slightly lower than that of the primary electron beam, but may have energies as low as ~50 eV (the upper cut-off for secondary electrons). Individual scattering events are generally elastic, where a negligible amount of energy is lost by the primary electron in the process. The direction of the electron may be altered, but its energy remains essentially the same. However, an electron that has undergone inelastic scattering (having excited a plasmon, phonon, caused inner shell ionization, or interacted with an electron in the valence band) may subsequently escape the sample surface as a BSE. Due to their higher momentum BSE can escape the sample from a depth of several tens of nm in heavy materials and hundreds of nm in light materials. To filter for energy, electrons are not accelerated towards the detector and only electrons with momentum

in the direction of the detector a captured, but this produces noisy images with poor spatial resolution.

(iii) **X-rays:** The number and energy of the X-rays emitted from a specimen are representative of the elemental composition of the specimen. The beam of electrons knocks a small fraction of electrons out of inner shells orbitals, in a process called inner-shell ionization. An atom remains ionized for only ~10^{-14} seconds before inner-shell vacancies are filled by outer-shell electrons, emitting a characteristic X-ray. Each atom interacts with an incident electron every ~10^{-12} seconds, thus, it is possible for a given atom to be repeatedly ionized. This process requires critical threshold energy to occur; beam electrons with lower energies cannot displace inner-shell electrons. This threshold energy is always larger than the energy of the associated X-ray. A spectrum is produced upon the detection of the X-rays. In the spectrum, X-ray lines are labelled according to the element that they represent (Si, Ca, Fe, etc). X-rays with their high energy and short wavelength escape from an excitation volume of several micrometres. The excitation volume depends on the acceleration voltage and the nature of the sample material and is much larger in lighter materials.

Energy Dispersive X-ray Spectroscopy (EDS): EDS is an analytical technique used for the elemental analysis or chemical characterization of a sample. The number and energy of the X-rays emitted from a specimen upon interaction with electron beam (as described above), can be measured by an energy-dispersive spectrometer. It is used in conjunction with the SEM to determine the elemental composition of a specimen. A typical spectrum produced by EDS analysis of a sample is shown in Figure 2.10.

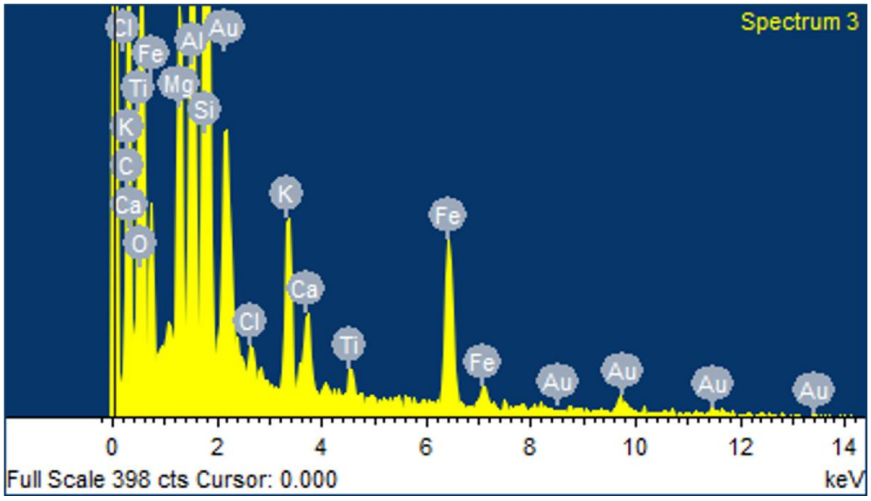

Figure 2.10: A spectrum obtained by EDS analysis of an ambient particle sample collected in Bathinda, Punjab, recorded at IISER Mohali.

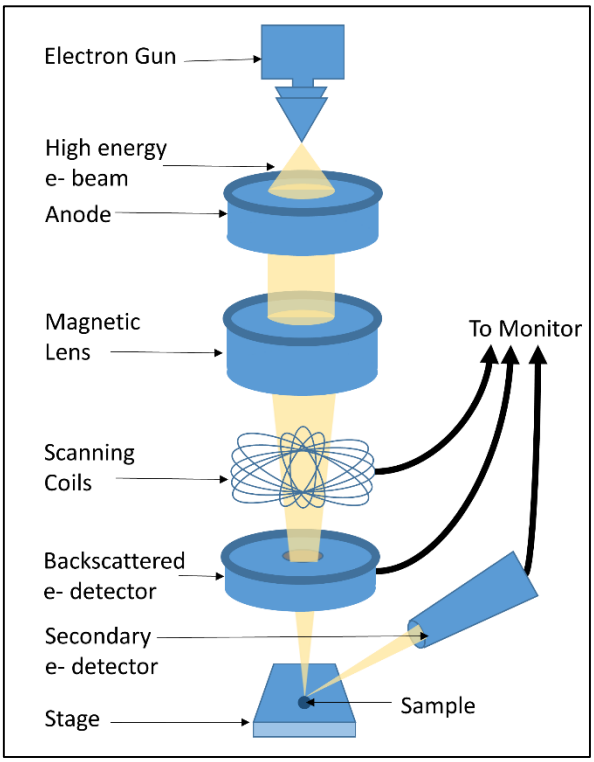

Figure 2.11: Schematic of a Scanning Electron Microscope

The structure of the instrument is shown in Fig 2.11. It consists of a vacuum system, an optical system (an electron gun, an anode, a magnetic lens and scanning coils) for generating, aligning, focussing and scanning the electron probe beam, a specimen stage for supporting the specimen, a secondary electron detector for detecting the secondary electrons, a display apparatus for displaying the image, and an operation system for performing the various operations. The space

inside the optical column and around the specimen is evacuated to vacuum to remove air molecules from the path of electrons. High-resolution SEM images can be produced when these components are used properly. Field-emission electron gun used in this model of SEM makes use of field emission that takes place from the surface of a sharp-pointed emitter made of metals, oxides or carbides when a strong electric field is present at the surface.

This model of SEM uses a Schottky field-emission electron gun that makes use of electric-field emission that takes place when zirconium oxide is supplied to the surface of tungsten to lower the work function of the tungsten. The Schottky field-emission electron gun can constantly supply the surface of the cathode with zirconium oxide by heating the surface of the cathode to 1800K. For this reason, using the Schottky field-emission electron gun, one can easily obtain stable and high probe current. The Gentle Beam method employed by this SEM slows down the electron beam just in front of the specimen, reducing the electron beam energy to diminish specimen damage while keeping the electron probe diameter small, to ensure high resolutions. Detectors in the SEM can be of multiple types, most commonly being SEI (detector for Secondary electron image, a pseudo-in-lens SE detector) and LEI (detector for Lower electron image, a regular SE detector), BEI (detector for Back-scattered electron image).

Using the SEM to take image involves the following steps:

(i) **Specimen preparation**: For studying aerosol particles, the particles are generally collected on a gold- coated filter (coated to make the medium more conducting with the help of Sputter coater) and a small part of the filter is mounted on top of a stub, secured with the help of adhesive carbon tape. This stub is attached into an appropriate specimen holder. Care must be taken to ensure that the specimen surface does not protrude through the cylinder top face, as it might cause damage to the specimen and the lens. It is also important to note the offset between the specimen and holder top surface and mention it in the operating software, if any.

(ii) **Loading a specimen**: SEM is very sensitive to any external disturbances and it is very crucial to maintain the vacuum inside the microscope all the time. Fixed procedures are therefore followed for loading a specimen in the instrument.

(iii) **Obtaining an image**: The electron beam is switched on only when the chamber vacuum pressure drops below 5×10^{-4} Pa. Before that, there are many parameters that need to be set according to requirement:

- **Accelerating voltage (AV)**: Energy of electrons in the beam. The higher the voltage, smaller is the electron probe prior to interacting with the sample. However, high AV can increase the chances of charging (when there is a build-up of e negative charge in the sample that is unable to go to ground) and

specimen damage. High AV also results in a lack of visibility of detailed structure of the specimen surface as the electrons exiting the sample come from a much larger sample volume and produces hazy pictures of overplayed structures. This happens primarily because higher AV increases the penetration depth, which in light materials is anyway already several >10 nm even at only 10 keV AV. This means part of the image signal starts coming from within the filter or worse at 30 keV even from the sticky tape underneath. Such a depth penetration is undesirable hence aerosol imaging at high acceleration voltage is not recommended. Nevertheless, chemical analysis demands that the selected acceleration voltage be higher than the excitation energy to remove inner shell electrons from the atom of interests. Hence 10 keV for lighter elements and 20 keV in sample that contain metals is required to perform simultaneous imaging and chemical analysis.

- **Lens/ Probe current**: Controls the electron probe diameter. The image smoothness, i.e., signal/ noise ratio depends of probe current. Smaller current, i.e., smaller the area of the generated beam, better the resolution and magnification. Higher the probe current, smoother the image but resolution is deteriorated and there is higher chance of damage to the specimen.
- **Beam current**: Flow rate, i.e. no. of electrons ejected per second
- **Photomultiplier voltage/ Contrast control**: Amplification level of the signal being detected
- **Working Distance (WD)**: Distance of the final lens from the sample top, measured in mm. Smaller the WD, smaller the depth of field (region of acceptable sharpness in front of and behind the point of focus) but higher resolution.
- **Detector**: Option of detectors for SEI, LEI, BEI, X-ray image. In case of SEI, since the generation region of secondary electrons is as shallow as approx. 10 nm at low AC, the diffusion of incident electrons within the specimen has little influence on the image, thus allowing the best resolution to be obtained. The contrast of secondary electron images depends mainly on the tilt angle and topography of the specimen surface. In case of BEI, the contrast of the image depends on the topography of the specimen surface and on the mean atomic number of the substances which constitute the specimen however, the image is very noise and the resolution is too poor for this detector to be of any use while

imaging aerosol samples. LEI can be used as an alternative as it only receives electrons with a high initial momentum and provides a pseudo-atomic number contrast mixed with the surface structure signal of a regular SE image.

Once the above settings are done, and the electron beam is switched on, low- level magnification mode (upto 500 times) is switched on to locate the area of study. Control knobs are also used to move the stage in horizontal direction along the x and y axes. The tilt of the specimen is also adjusted to suit the requirement. Once the area is selected, low-magnification mode is changed to high- magnification mode. Magnification in this mode can be done up to 1,20,000 times. Magnification is a function of area scanned and viewing size. Two controls adjust the magnification: the raster coils and the location of the focal point of the primary beam to the final lens. Focus is then adjusted to see the relevant points more clearly and sharply. Once the correct adjustments are done, and the right area is in focus, image is 'freezed' and photo is recorded. A sample of a Scanning Electron Micrograph is provided in Figure 2.12.

It must be noted that if the electron beam is allowed to observe an area for a long period of time, it can cause electrons to accumulate and charge to build up on the sample (charging). It can also result in removal of volatile species from the sample, etch the sample through beam induced damage or result in changes of surface structure due to deposition of elemental carbon on the electron irradiated surface if the instrument is contaminated with trace amounts organic vapours.

(iv) **Optimizing an image**: In order to obtain high quality images, there are four primary parameters that can be adjusted in addition to the ones discussed above.

- **Brightness**: The value of each of the individual pixels that compose the image. The higher the overall pixel values the brighter the image. Extreme values of brightness can cause loss of information. This parameter can also be adjusted using image editing softwares, after the image has been recorded.
- **Contrast**: Contrast is the difference between two pixels. The overall contrast is the difference between the lowest pixel value and the highest pixel value. Optimum value of contrast prevents masking of any information about the specimen under study. This parameter can also be increased within certain margins after the image has been recorded, however a badly contrasted image with oversaturated black and white pixels cannot be recovered in retrospect.

Care must be taken to not over contrast images, as this can suppress information present in the image.

- **Beam alignment**: When the column is disassembled for cleaning or when the electron beam is lost, an operation called "alignment of the column" allows for the electron beam from the filament to be most effectively collected onto the specimen surface by means of mechanical and electrical alignment. If beam is not aligned, an intense 'wobbling' effect makes it difficult to capture a high-quality micrograph. In this operation, the electron beam from the gun is aligned using a tilting correction knob.
- **Astigmatism**: The aberration caused by the machining accuracy and material of the polepiece is called "astigmatism." This astigmatism can be removed by adjusting the two knobs, X and Y, of the stigmator. An image is judged as astigmatism-free if it has no unidirectional defocusing when the objective lens is changed to under or over-focus at a medium to high magnification (about x10,000-100,000).

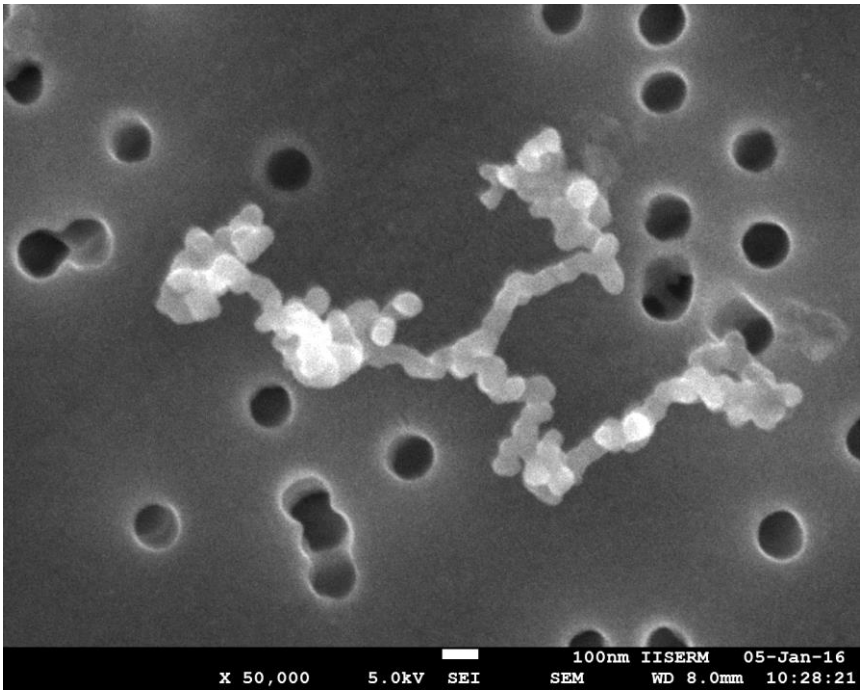

Figure 2.12: An SEM image of a soot particle collected from a garbage- burning source, recorded at IISER Mohali.

2.3 Tools for aerosol source apportionment

Aerosol source apportionment has been performed using various tools. Each tool has its advantages and limitations, with a limited scope of application to the type of aerosols. Following are some of the source apportionment techniques relevant to my study:

2.3.1 Optical method:

This method is generally applied for source apportionment of BC aerosol. It apportions BC mass loading into two or more sources, based on it's measured optical properties, particularly, the absorption angstrom exponent (α_{abs}). The absorption angstrom exponent of aerosol is a quantity that is used to characterize the spectral dependence of light absorption by the aerosol (Bond et al., 2013). The higher value of α_{abs} (>1.0) implies higher spectral dependence of light absorption by the sample. Measurements made by optical method based instruments like Aethalometer, that provide absorption coefficient values of aerosol measured over two wavelengths can be used to calculate Absorption Angstrom exponent using the following relationship:

$$\alpha_{abs\ (\lambda 1-\lambda 2)} = -\frac{ln\frac{b_{abs\ (\lambda 1)}}{b_{abs\ (\lambda 2)}}}{ln\frac{\lambda 1}{\lambda 2}} \quad (28)$$

Only recently, Sandradewi and co-workers (Sandradewi et al., 2008a) had proposed that α_{abs} can be used to constrain the contribution of biomass combustion to the total BC_{eq} mass. BC_{eq} from fossil fuel (ff) burning sources typically has an $\alpha_{abs\text{-}ff}$ of 1±0.1 (Bergstrom et al., 2002; Bond and Bergstrom, 2006; Moosmüller et al., 2009). It is believed that a larger absorption angstrom exponent value ($\alpha_{abs\text{-}bb}$ (bb= biomass burning) >1) is characteristic of biomass and biofuel burning. Wood burning and other types of biomass combustion are considered to produce a significant amount of primary organic matter, which is internally mixed with the BC emitted (Chakrabarty et al., 2010; Kirchstetter et al., 2004; Pósfai et al., 2003). Some organic carbon compounds (for example the polycyclic aromatic hydrocarbons (PAHs) and pyrolysis products of lignin) (Hoffer et al., 2006; Lack et al., 2013), exhibit a strong spectral dependence of light extinction as the $\pi \rightarrow \pi^*$ transitions of conjugated double bonds in the aromatic ring absorb in the UV, and in the lower visible range (Chakrabarty et al., 2010; Clarke et al., 2007; Herich et al., 2011; Hoffer et al., 2006; Kirchstetter et al., 2004; Lewis et al., 2008; Moosmüller et al., 2009; Reid et al., 2005; Sandradewi et al., 2008b; Schmid et al., 2006; Yang et al., 2009) ($\alpha_{abs370\text{-}880}$ as high as 6.8 (Hoffer et al., 2006)). The presence of such light absorbing organic carbon is considered to be responsible for the higher α_{abs} of biomass combustion $BC_{eq\text{-}bb}$ as compared to that of $BC_{eq\text{-}ff}$ from fossil fuel combustion. Subsequently, Sandradewi and co-worker (Sandradewi et al., 2008c) developed a method called the two-component aethalometer model, which apportions total BC_{eq} into BC_{eq} from

wood burning (BC_{eq-wb}) and BC_{eq} from fossil fuel combustion (BC_{eq-ff}). They used the terminology CM(PM)=OC+EC for their source apportionment model. Because the aethalometer, after filter loading and scattering correction, quantifies only the extinction of the light absorbing fraction of the PM (BC + BrC) and corrects for the extinction by the scattering fraction of the PM (which includes both, the inorganic aerosol and the scattering fraction of the organic carbon (OC)), their CM(PM) (Sandradewi et al., 2008c) = LAC (Andreae and Gelencser, 2006; Bond and Bergstrom, 2006) = BC_{eq} (Petzold et al., 2013). Strictly speaking, CM(PM) includes only a subset of the OC, namely the light absorbing fraction, the so called brown carbon (BrC). They recommended using α_{ff} = 1.1 for traffic BC_{eq} and α_{wb} = 1.8-1.9 for wood burning BC_{eq} and validated the method and parameterization with data collected in the Swiss Alps, where wood burnt in stoves for domestic heating purposes and traffic dominate BC_{eq} emissions. For the validation, a set of independent wood burning tracers (such as C-14, levoglucosan and potassium) were employed (Sandradewi et al., 2008b). Other authors subsequently used this methodology to constrain emission inventories in the Alpine region (Favez et al., 2010; Herich et al., 2011, 2014), and demonstrated good agreement between the two-component aethalometer source-apportionment model and Chemical Mass Balance (CMB) model results. Recently, the two-component aethalometer source-apportionment model has been applied at sites outside the Alpine region e.g., in London (BC_{eq-wb}=15±12% and 30±13% of the total BC_{eq} for two different sites) (Crilley et al., 2014). Magee Scientific has launched a new aethalometer model (AE 33) which uses this methodology to apportion the measured BC_{eq} into BC_{eq-ff} and BC_{eq-bb}. This model of aethalometer was deployed during the Klagenfurt (Austria) campaign in March 2012 (Drinovec et al., 2015).

In India, Gadhavi and Jayaraman (Gadhavi and Jayaraman, 2010) used the two-component aethalometer source-apportionment model to calculate the contribution of biomass burning to total BC_{eq} in morning and evening times in a remote village site and estimated that only 20-40% of the BC_{eq} originates from biomass combustion. Similarly, Tiwari et al. (Tiwari et al., 2014), using the Magee Scientific aethalometer model (AE 31), found that α_{abs} of BC_{eq} varied from 0.63 to 1.29 (with a mean value of 1.09±0.11) during winter 2011-12 in New Delhi and concluded that ~94% of the BC_{eq} originated from fossil fuel combustion and only ~6% of the BC_{eq} was contributed by biomass burning. Both findings are unexpected, considering the rampant use of biomass for domestic cooking and heating purposes, particularly in rural India and during winter in the IGP. These facts, based on activity observation, were recently confirmed using C-14 analysis of black carbon aerosol. Gustafsson and co-workers (Gustafsson et al., 2009) found that biomass combustion in India contributed between half and two thirds to the total BC over India. The currently used emission inventories attribute 55%-88% of the BC emissions over South Asia to

biomass combustion (Dickerson et al., 2002; Reddy and Venkataraman, 2002a, 2002b; Venkataraman et al., 2005).

There is contrast between the findings based on the two-component aethalometer source-apportionment model and other estimates based on independent tracers such as C-14 or aerosol chemical composition, which suggests that using Angstrom Exponent for BC source apportionment has its limitations. Moreover, the fact that α_{abs} of BC_{eq} for individual measurement points dropped to values as low as 0.63 during fog episodes in New Delhi, i.e. well below α_{abs} = 0.9 (which is considered to be the lowest possible value for calculations employing the two-component aethalometer model), seems to suggest that aerosol mixing state or coatings acquired during aqueous phase processing may affect α_{abs}. It should also be noted that in current literature, reported α_{abs} values vary from 0.9 (Day et al., 2006; Lewis et al., 2008) to 3.5 (Chakrabarty et al., 2010; Clarke et al., 2007; Herich et al., 2011; Hoffer et al., 2006; Kirchstetter et al., 2004; Lewis et al., 2008; Reid et al., 2005; Sandradewi et al., 2008b; Schmid et al., 2006; Yang et al., 2009) for wood burning, and from 0.9 to 1.1 (Bond, 2001; Kirchstetter et al., 2004; Lewis et al., 2008) for fossil fuel burning. Values lower than 0.9 have not been discussed so far, but have been observed experimentally in India (Gadhavi and Jayaraman, 2010; Tiwari et al., 2014). Lack et al. (Lack et al., 2013) studied brown carbon emissions from a forest fire plume and found that the variations in the angstrom exponent of absorption correlated with the ratio of levoglucosan and CO_2-measured by the aerosol mass spectrometer (AMS) as well as with the absolute levoglucosan mass. Their data seems to suggest that only a subset of the particulate organic matter emitted from the fire is responsible for the excess absorption. Two recent studies reported real time measurements of the α_{abs} and combustion efficiency for biomass burning in traditional cooking stoves (Roden and Bond, 2006) and for wood fired heating systems (Martinsson et al., 2015) and found α_{abs}=1 for flaming conditions, while α_{abs} >>1 (up to α_{abs} = 6) was reported for the same fire under smoldering conditions. According to these studies, α_{abs} varies as a function of the combustion efficiency within the flame of an individual cooking fire in traditional cook stoves. This means that the α_{abs} value is not a direct indication of the source of BC, and there are many factors other than the source, that influence the value of α_{abs}. Therefore, it is likely that application of the two-component aethalometer model in places with a variety of sources of BC (and not solely fossil fuel use and wood burning in stoves), where domestic biofuel use is a major source of black carbon and where there is rampant use of adulterated fuel in vehicles, will produce erroneous results. Thus, the optical method as a source apportionment tool has it's limitations, and must be applied carefully. Chapter 3 investigates whether the same can be applied in the Indian context.

2.3.2 Cluster analysis

Back- trajectories derived from online trajectory models or determined through other methods, are often used to trace back the origin of air masses carrying aerosol particles. These back- trajectories are produced in the form of co- ordinates of trajectory segments at equal time steps. Depending upon the scale of trajectory transport, the scale of aerosol transport is determined by this method, e.g., application of cluster analysis to long, trans- national back- trajectories will determine the long-range sources of aerosol particles. While using back- trajectories, long- term studies are often more useful and provide more statistically robust results. Cluster analysis is a statistical method used to group data in large data sets into a small number of clusters. Clusters are groups with similar distributions, in the case of back trajectories, similar directions and lengths or a combination of trajectory pathways and composition (Fleming et al., 2012). Cluster analysis is often performed using statistical tools like PAST (PAleontological STatistics), MS Excel, Igor Pro, etc. This method can be applied on air masses' trajectory coordinates (time steps) as the clustering variables. Hierarchical and non- hierarchical algorithms of doing clustering exist. A non-hierarchical method known as the k- means procedure is commonly used (Pawar et al., 2015). The air mass back trajectories are subjected to k- means clustering using statistical software and The number of clusters "k" is to be specified by the user prior to clustering. The assignment of back- trajectories to clusters is initially random. In an iterative procedure, trajectories are then moved to the cluster which has the closest cluster mean in Euclidean distance, and the cluster means are updated accordingly. This process continues until the process of hopping from one cluster to another, ceases. As a normal artefact of the k means clustering algorithm, the result is dependent upon the seed used for clustering. Clustering result with the lowest root mean square difference for each predefined number of clusters is selected. The root mean square difference for an individual latitude and longitude value is given by

$$RMSD = \sqrt{(x_i - \bar{x})^2} + \sqrt{(y_i - \bar{y})^2} \quad (29)$$

where, x_i and y_i stand for the latitude and longitude of the individual trajectory for a given hour and $\bar{x}$ and $\bar{y}$ for the cluster mean latitude and longitude of the same hour for the cluster to which that trajectory belongs. The total root mean square difference t-RMSD is the sum over all the RMSD values for a given set of back trajectories. The optimal number of clusters that best describe the different air-flow patterns to the measurement site by computing the change in the minimum t-RMSD while increasing

the number of clusters from n to n+1, are selected. This change in the minimum t-RMSD decreases abruptly as clusters of trajectories which are significantly different in terms of wind directions and speeds are separated from each other.

Aerosol mass loadings are associated with these clusters to determine their source of origin. The limitation of this method is that it cannot be effectively applied for studies that are based on short periods of time as it needs a large statistical base. Moreover, cluster analysis of the trajectory data (Baker, 2010; Li et al., 2012) groups air masses into groups of similar origin and associates elevated PM_{10} mass loadings or exceedance events with certain large scale atmospheric transport situations and broad regions upwind, but does not attribute them to specific sources with spatially fixed coordinates.

2.3.3 Concentration- weighted trajectory method (CWT):

Back- trajectory data can be attributed to sectored geographical area (e.g., cells of a superimposed grid) based on residence time analysis (RTA) (Lee and Ashbaugh, 2007; Stohl, 1998). Such RTA includes the CWT (Seibert et al., 1994) (Concentration weighted trajectory) maps, which are produced by calculating weighted concentration averages for cells of a spatial grid over which the back-trajectories of air masses passed prior to reaching receptor sites. Such an approach seeks to attribute all of the aerosol mass loading observed at a receptor site to spatially distant sources under the assumption that each grid cell over which the air mass passed in the hours prior to reaching the receptor site has an equal probability of being the source of the aerosol measured at the receptor site. For each cell i, the following relationship is used to calculate the concentration weighted average (CWA) value that signifies the contribution of the cell to the aerosol mass loading observed at the receptor site:

$$CWA_i = \frac{\Sigma\,(\text{Aerosol concentrations associated with the contributing air mass trajectories})}{\text{No.of contributing air mass trajectories}} \quad (30)$$

It has been demonstrated that this approach is mathematically robust only when multiple receptor sites are used to drive the model (Keeler and Samson, 1989; Lee and Ashbaugh, 2007), however, several studies have used single site data. Similarly, back-trajectory analysis can involve calculating residence time weighted concentration (RTWC) (Stohl, 1996) for the geographical sectors. Generally, the result is produced in the form of contour map over a gridded array of cells and helps to identify the spatial location of sources. However, the meteorological grids behind back- trajectory models have a limited resolution (typically 1° x 1°) and hence back trajectory analysis is not suitable to pinpoint sources on a regional scale, where the required pixel resolution would be of a few kilometers at the most.

2.3.4 PSCF

PSCF (Potential Source Contribution Function) is a kind of Conditional Probability which is used for locating sources of pollutant species. PSCF provides the probability that an air mass with

specified pollutant concentrations arrive at a receptor site after having been observed to reside in a specific geographical cell (Zeng and Hopke, 1989). It can be applied to segmented trajectory data for attributing source contribution value to grid cells of a gridded spatial map (Fleming et al., 2012). In this, for each grid cell, the ratio of the number of trajectory segments arriving on a day which had source contribution factor or pollutant concentration greater than a criterion value, that lie in the cell, to the total number of trajectory segments falling in the cell, is used to calculate the PSCF value of the cells.

$$Conditional\ Probability\ value\ = \frac{No.of\ traj\ segments\ in\ the\ cell\ that\ exceed\ the\ criterion\ value}{Total\ number\ of\ traj\ segments\ in\ the\ cell} \quad (31)$$

Therefore, the cells that have sources, have high PSCF value. Like any conditional probability function, this technique is purely a statistical tool and depends on the size and quality of database. Color- coding the gridded map's cells according to their PSF values enables easy comprehension of the location of the sources over the study region. For this technique, too, results are only robust when multiple receptor sites are used.

2.3.5 Conventional tools for local- scale source apportionment

Wind rose plots and Pollution roses have so far been used to attribute the observed mass concentration at the receptor site to local sources. They allow for identification of the direction from the receptor, in which a strong local source is located. However, both give insufficient amount of spatial information as the distance remains unknown. Wind roses and bivariate polar plots (Carslaw et al., 2006; Tomlin et al., 2009; Westmoreland et al., 2007) prepared using a wind speed-wind direction relationship could in principle be converted to a distance vector, provided multiple receptors are analyzed jointly. However, till date even those studies that used several pollution roses from multiple, closely- located stations, did not produce a single coherent map (Carslaw et al., 2006).

Regional source apportionment till date has mostly been attempted using models targeted at the analysis of multivariate chemical data like PCA (Principal Component analysis) (Beaver and Palazoglu, 2006; Chan and Mozurkewich, 2007; Hart et al., 2006; Song et al., 2008), PMF (Positive Matrix Factorization) (Cheng et al., 2011; Henry and Christensen, 2010; Poirot et al., 2001; Zauscher et al., 2013) and EPA's CMB (Chemical Mass Balance) (Bhave et al., 2001; Maykut et al., 2003), EPA's UNMIX (Poirot et al., 2001; Song et al., 2008) for source-apportionment of measured species. These models can attribute the PM_{10} mass to different sectors or chemical processes (e.g. transport, industry, windblown dust, gas-to-particle conversion), but they are not useful for identifying (pin-pointing) individual sources in a spatial context and require

chemical information, which is available for a much more limited number of air quality monitoring stations. Moreover, some models like CMB require a-priori information about the sources.

Identification of regional or local sources of pollutants is important in view of the intensity and sometimes, promptness of the impact of their emissions (Harrison et al., 1996), and without the spatial coordinates of the sources, mitigation continues to be a challenge.

A new model called MuReSAM (Multi- receptor site Regional Source Apportionment Model) that is based on the CWT method has been developed by me and is presented in Chapter 4. This model is applicable to regional scale transport of aerosol particles to apportion it to regional sources, while using data from multiple receptor sites, producing result in the form of a color- coded gridded map of the study region. Working of the model has been successfully demonstrated by it's application to ambient PM_{10} mass loading measured at 14 sites in the Hessen region of Germany, from 1 November 2014 to 20 July 2015. Another advantage of this model is that it allows only those grid cell values to show on the map to which three or more receptor sites have contributed input data, thus increasing the statistical robustness of the results.

Chapter 3

Limitation of the Use of the Absorption Angstrom Exponent for Source Apportionment of Equivalent Black Carbon: A case study from the North West Indo- Gangetic Plain

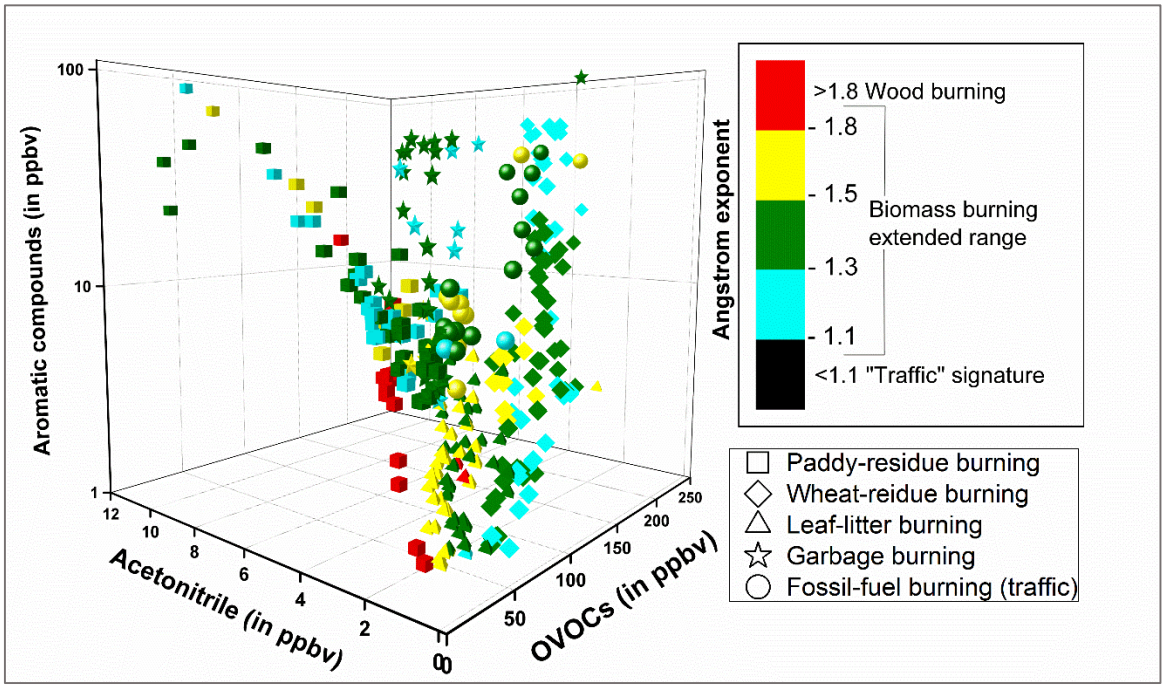

Abstract in graphical form: No correlation between absorption angstrom coefficient and the type of fuel burnt.

3.1 Abstract

Angstrom exponent measurements of equivalent black carbon (BC_{eq}) have recently been introduced as a novel tool to apportion the contribution of biomass burning sources to the BC_{eq} mass. The BC_{eq} (equivalent mass) is the mass of ideal BC with defined optical properties, that,

upon deposition on the aethalometer filter tape, would cause equal optical attenuation of light at a given wavelength, to the actual $PM_{2.5}$ aerosol deposited. The BC_{eq} mass hence is identical to the mass of the total light absorbing carbon (LAC) deposited on the filter tape (LAC= BC_{eq}). Here, we use simultaneously collected high time resolution data from a 7-wavelength aethalometer (AE 42, Magee Scientific, USA) and a high sensitivity Proton Transfer Reaction- Quadrupole Mass Spectrometer (PTR-MS) installed at a sub-urban site in Mohali (Punjab), India, to identify a number of biomass combustion plumes during which BC_{eq} (black carbon) enhancements correlated strongly with an increase in acetonitrile mixing ratio. The identified types of biomass combustion include two different types of crop residue burning (paddy and wheat), burning of leaf-litter, and garbage burning. Traffic (fossil-fuel burning) plumes were also selected for comparison. We find that the combustion efficiency, rather than the fuel used, determines $\alpha_{abs,}$ and consequently, the α_{abs} can be ~1 for flaming biomass combustion and >1 for older vehicles that operate with poorly optimized engines. Thus, the absorption angstrom exponent is not representative of the fuel used and therefore, cannot be used as a generic tracer to constrain source contributions.

3.2 Introduction

Black carbon (BC) consists of optically absorbing particles produced from incomplete combustion (Bond et al., 2013; Pósfai and Buseck, 2010). The presence of fine particulate matter, such as black carbon, in the atmosphere impairs visibility (Bond et al., 2013; Pósfai and Buseck, 2010) and human health (Grahame and Schelsinger, 2007; Peters et al., 2000). BC also alters the radiative budget of Earth through direct, semi-direct and indirect effects (Bond et al., 2013; Jacobson, 2001; Stocker et al., 2013). The direct radiative forcing term of BC includes the effects of atmospheric warming (Bond et al., 2013; Jacobson, 2001; Menon et al., 2002; Stocker et al., 2013), decrease in the albedo of ice cover due to black carbon deposited on ice (Quinn et al., 2008), and surface dimming due to scattering and absorption of incoming solar radiation (Bond et al., 2013). Semi-direct forcing effects include the impact of cloud burning and BC-induced perturbations of the atmospheric temperature structures on cloud cover (Ramanathan et al., 2001). Indirect effects comprise the modification of cloud properties and cloud cover due to perturbation of the number density, size distribution and chemical properties of the cloud condensation nuclei population (Bond et al., 2013).

Recently, black carbon has attracted a lot of attention as it combines two interesting properties. Firstly, it is the second most important climate warming agent after carbon dioxide, with a total

climate forcing of +1.1 Wm^{-2} (a range 0.17-2.1 W m^{-2}) (Bond et al., 2013; Stocker et al., 2013) and secondly, it has a short atmospheric lifetime of days to weeks (Bond et al., 2013; Mao et al., 2014; Pósfai and Buseck, 2010). Identifying black carbon sources for targeted mitigation has the potential to offset the CO_2- induced warming in the near and intermediate future as it is a short lived climate pollutant (SLCP).

The current black carbon emission inventories are highly uncertain, with a range of 2,000 – 29,000 Gg BC emissions per year (Bond et al., 2013). The largest uncertainties pertain to domestic biofuel use, open burning (which includes both wild vegetation fires and anthropogenic emissions like crop residue burning), and industrial coal use (in particular, consumption by small scale cottage industries in developing economies) (Bond et al., 2013). The contribution of open waste burning of domestic and industrial waste has been largely neglected in the black carbon emission inventories, due to lack of activity data (Bond et al., 2013).

The Indo-Gangetic Plain (IGP), being one of the most densely populated regions on the planet, is characterized by large anthropogenic BC emissions from rural households (cooking on biomass), mobile sources, thermal power plants and industries (Ramanathan and Ramana, 2005; Rehman et al., 2011). Recently, Sandradewi and co-workers (Sandradewi et al., 2008a) proposed that the absorption angstrom exponent (α_{abs}), which can be derived from multi-wavelength aethalometer measurements, can be used to constrain the contribution of biomass combustion to the total BC_{eq} mass. The BC_{eq} (Petzold et al., 2013) (equivalent mass) is the mass of ideal (graphitic) BC (elemental carbon EC) with defined optical properties (MAC = 11115/λ for the Harvard TOR-EC calibration) that, upon deposition on the aethalometer filter tape would cause equal optical attenuation of light at a given wavelength as the actual $PM_{2.5}$ aerosol deposited. The BC_{eq} mass hence is identical to the mass of the total light absorbing carbon (LAC) mass deposited on the filter tape, which includes black carbon and brown carbon (BC_{eq} = LAC (Andreae and Gelencser, 2006; Bond and Bergstrom, 2006) = BC + BrC). The absorption angstrom exponent of aerosol is a quantity that is used to characterize the spectral dependence of light absorption by the aerosol (Bond et al., 2013). The higher value of α_{abs} (>1.0) implies higher spectral dependence of light absorption by the sample. BC_{eq} from fossil fuel (ff) burning sources typically has an $\alpha_{abs\text{-}ff}$ of 1±0.1 (Bergstrom et al., 2002; Bond and Bergstrom, 2006; Moosmüller et al., 2009). This weak dependence of $\alpha_{abs\text{-}ff}$ on the wavelength of the light is due to the fact that the value of α_{abs} for small particles is usually greater than that of the bulk material. If the bulk material has no absorption-wavelength dependence (α_{abs} = 0), as does graphite (Borghesi and Guizetti, 1991), then α_{abs} = 1 for particles smaller than the wavelength of light (Moosmüller et al., 2011; Rosen et al., 1979). It

is believed that a larger absorption angstrom exponent value ($\alpha_{abs\text{-}bb}$ (bb= biomass burning) >1) is characteristic of biomass and biofuel burning. Wood burning and other types of biomass combustion are considered to produce a significant amount of primary organic matter, which is internally mixed with the BC emitted (Chakrabarty et al., 2010; Kirchstetter et al., 2004; Pósfai et al., 2003). Some organic carbon compounds (for example the polycyclic aromatic hydrocarbons (PAHs) and pyrolysis products of lignin) (Hoffer et al., 2006; Lack et al., 2013), exhibit a strong spectral dependence of light extinction as the $\pi \rightarrow \pi^*$ transitions of conjugated double bonds in the aromatic ring absorb in the UV, and in the lower visible range (Chakrabarty et al., 2010; Clarke et al., 2007; Herich et al., 2011; Hoffer et al., 2006; Kirchstetter et al., 2004; Lewis et al., 2008; Moosmüller et al., 2009; Reid et al., 2005; Sandradewi et al., 2008b; Schmid et al., 2006; Yang et al., 2009) ($\alpha_{abs370\text{-}880}$ as high as 6.8 (Hoffer et al., 2006)). The presence of such light absorbing organic carbon is considered to be responsible for the higher α_{abs} of biomass combustion $BC_{eq\text{-}bb}$ as compared to that of $BC_{eq\text{-}ff}$ from fossil fuel combustion. Subsequently, Sandradewi and co-worker (Sandradewi et al., 2008c) developed a method called the two-component aethalometer model, which apportions total BC_{eq} into BC_{eq} from wood burning ($BC_{eq\text{-}wb}$) and BC_{eq} from fossil fuel combustion ($BC_{eq\text{-}ff}$). They used the terminology CM(PM)=OC+EC for their source apportionment model. Because the aethalometer, after filter loading and scattering correction, quantifies only the extinction of the light absorbing fraction of the PM (BC + BrC) and corrects for the extinction by the scattering fraction of the PM (which includes both, the inorganic aerosol and the scattering fraction of the organic carbon (OC)), their CM(PM) (Sandradewi et al., 2008c) = LAC (Andreae and Gelencser, 2006; Bond and Bergstrom, 2006) = BC_{eq} (Petzold et al., 2013). Strictly speaking, CM(PM) includes only a subset of the OC, namely the light absorbing fraction, the so called brown carbon (BrC). They recommended using α_{ff} = 1.1 for traffic BC_{eq} and α_{wb} = 1.8-1.9 for wood burning BC_{eq} and validated the method and parameterization with data collected in the Swiss Alps, where wood burnt in stoves for domestic heating purposes and traffic dominate BC_{eq} emissions. For the validation, a set of independent wood burning tracers (such as C-14, levoglucosan and potassium) were employed (Sandradewi et al., 2008b). Other authors subsequently used this methodology to constrain emission inventories in the Alpine region (Favez et al., 2010; Herich et al., 2011, 2014), and demonstrated good agreement between the two-component aethalometer source-apportionment model and Chemical Mass Balance (CMB) model results. Recently, the two-component aethalometer source-apportionment model has been applied at sites outside the Alpine region e.g., in London ($BC_{eq\text{-}wb}$=15±12% and 30±13% of the total BC_{eq} for two different sites) (Crilley et al., 2014). Magee Scientific has launched a new aethalometer

model (AE 33) which uses this methodology to apportion the measured BC_{eq} into $BC_{eq\text{-}ff}$ and $BC_{eq\text{-}bb}$. This model of aethalometer was deployed during the Klagenfurt (Austria) campaign in March 2012 (Drinovec et al., 2015).

In India, Gadhavi and Jayaraman (Gadhavi and Jayaraman, 2010) used the two-component aethalometer source-apportionment model to calculate the contribution of biomass burning to total BC_{eq} in morning and evening times in a remote village site and estimated that only 20-40% of the BC_{eq} originates from biomass combustion. Similarly, Tiwari et al. (Tiwari et al., 2014), using the Magee Scientific aethalometer model (AE 31), found that α_{abs} of BC_{eq} varied from 0.63 to 1.29 (with a mean value of 1.09±0.11) during winter 2011-12 in New Delhi and concluded that ~94% of the BC_{eq} originated from fossil fuel combustion and only ~6% of the BC_{eq} was contributed by biomass burning. Both findings are unexpected, considering the rampant use of biomass for domestic cooking and heating purposes, particularly in rural India and during winter in the IGP. These facts, based on activity observation, were recently confirmed using C-14 analysis of black carbon aerosol. Gustafsson and co-workers (Gustafsson et al., 2009) found that biomass combustion in India contributed between half and two thirds to the total BC over India. The currently used emission inventories attribute 55%-88% of the BC emissions over South Asia to biomass combustion (Dickerson et al., 2002; Reddy and Venkataraman, 2002a, 2002b; Venkataraman et al., 2005). The contrast between the findings based on the two-component aethalometer source-apportionment model and other estimates based on independent tracers such as C-14 or aerosol chemical composition suggest that this approach may have its limitations. Moreover, the fact that α_{abs} of BC_{eq} for individual measurement points dropped to values as low as 0.63 during fog episodes in New Delhi, i.e. well below $\alpha_{abs} = 0.9$ (which is considered to be the lowest possible value for calculations employing the two- component aethalometer model), seems to suggest that aerosol mixing state or coatings acquired during aqueous phase processing may affect α_{abs}. It should also be noted that in current literature, reported α_{abs} values vary from 0.9 (Day et al., 2006; Lewis et al., 2008) to 3.5 (Chakrabarty et al., 2010; Clarke et al., 2007; Herich et al., 2011; Hoffer et al., 2006; Kirchstetter et al., 2004; Lewis et al., 2008; Reid et al., 2005; Sandradewi et al., 2008b; Schmid et al., 2006; Yang et al., 2009) for wood burning, and from 0.9 to 1.1 (Bond, 2001; Kirchstetter et al., 2004; Lewis et al., 2008) for fossil fuel burning. Values lower than 0.9 have not been discussed so far, but have been observed experimentally in India (Gadhavi and Jayaraman, 2010; Tiwari et al., 2014). Lack et al. (Lack et al., 2013) studied brown carbon emissions from a forest fire plume and found that the variations in the angstrom exponent of absorption correlated with the ratio of levoglucosan and CO_2- measured by the aerosol mass

spectrometer (AMS) as well as with the absolute levoglucosan mass. Levoglucosan (m60) is an organic molecule formed from the pyrolysis of cellulose. CO_2 (m44) is a proxy for the oxidized organic mass measured by AMS. Their data seems to suggest that only a subset of the particulate organic matter emitted from the fire is responsible for the excess absorption. Two recent studies reported real time measurements of the α_{abs} and combustion efficiency for biomass burning in traditional cooking stoves (Roden and Bond, 2006) and for wood fired heating systems (Martinsson et al., 2015) and found $\alpha_{abs}=1$ for flaming conditions, while $\alpha_{abs} >> 1$ (up to $\alpha_{abs} = 6$) was reported for the same fire under smoldering conditions. If the α_{abs} really varies as a function of the combustion efficiency within the flame of an individual cooking fire in traditional cook stoves, this has two implications. Firstly, it may be impossible to employ the two- component aethalometer model in South Asia, where domestic biofuel use is a major source of black carbon. Secondly, this behavior of α_{abs} may not be restricted to cooking fires but may extend to other combustion types (for example, open waste burning, wildfires and crop residue burning) which are equally affected by highly variable combustion efficiencies.

In this study, we use simultaneously collected high time resolution data from a 7-wavelength aethalometer (AE 42, Magee Scientific, USA) and a Proton Transfer Reaction- Quadrupole Mass Spectrometer (PTR-MS) installed at a sub-urban site in Mohali (Punjab), India to investigate whether the absorption angstrom exponent can be used as a specific tracer for biomass burning emissions or varies as a function of combustion efficiency within the same plume.

For this purpose, we identified biomass combustion plumes, during which BC_{eq} enhancements correlated strongly with an increase in acetonitrile mixing ratios (an excellent gaseous tracer for biomass burning (Bange and Williams, 2000; de Gouw et al., 2003; Holzinger et al., 1999, 2001)) and used emission ratios of aromatic compounds and oxygenated VOCs as well as auxiliary data (e.g., MODIS fire counts; meteorological data and mixing ratio of NO) to classify the events into four different types of biomass combustion, each of which is characterized by distinct emission ratios. The identified types of biomass combustion include two different types of crop residue burning (paddy and wheat), burning of leaf-litter, and garbage burning. Traffic (fossil-fuel burning) events were also selected for comparison. The results demonstrate that the absorption angstrom exponent cannot be used as a generic tracer for biomass combustion.

3.3 Experimental

3.3.1 Measurement site

Ambient BC_{eq} and VOC measurements were acquired at the Atmospheric Chemistry Facility (30.667◦ N–76.729◦ E, 310 m a.s.l.) of Indian Institute of Science Education and Research- Mohali, which is a sub- urban site in the N.W. Indo-Gangetic Plain. A detailed description of the site and the facility, along with the technical details for VOC measurements and data quality protocols followed can be found in Sinha and co-workers (Sinha et al., 2014). More recently, a detailed description of the meteorology of different seasons at this site has been provided in Pawar and co-workers (Pawar et al., 2015). Air masses reaching the facility can be classified according to their fetch region into urban, industrial and rural/agricultural (Sinha et al., 2014). Small slum colonies, several construction sites and vacant plots on which garbage collectors sort trash and burn the items that have no commercial value (Nandy et al., 2015), also exist in the urban/industrial sector. Therefore, the facility is ideal for contrasting emissions with a variety of source signatures. The data used for this study was obtained between April 2013 and April 2014. The campus had about 800 residents during the period 2013-14. Emission activity due to residents of the campus is minimal.

3.3.2 Instrumentation

Ambient mixing ratios of volatile Organic Compounds were measured in real time by a PTR-Quadrupole Mass spectrometer (HS Model 111-07HS-088, Ionicon Analytik Gesellschaft, Austria). The PTR-MS technique and its validation in ambient VOC identification and quantification studies using measurements of the corresponding protonated organic ions (m/z of the $VOCH^+$) in the mass spectrometer has been reviewed extensively elsewhere (Blake et al., 2009; de Gouw and Warneke, 2007). Briefly, VOCs present in ambient air, which have a proton affinity greater than that of water, undergo soft chemical ionization with the reagent hydronium ions in a drift tube to form the corresponding protonated organic ions ($VOCH^+$), which are then separated using a quadrupole mass analyzer and detected using a secondary electron multiplier. Mixing ratios of the following VOCs were quantified: methanol (m/z =33); acetonitrile (m/z = 42); acetone (m/z=59), acetic acid (m/z=61), benzene (m/z = 79), toluene (m/z = 93), sum of C-8 aromatics (m/z = 107) and sum of C-9 aromatics (m/z = 121). The sensitivity of certain compounds such as benzene can change if the ratio of hydrated hydronium ions to the primary hydronium ions is larger than 10% but for our instrumental conditions (~135 Townsend), this ratio was found to be always below 6%; hence, no corrections were required. Span calibrations by dynamic dilution of a custom

ordered gas standard (Apel Riemer et al; stated accuracy 5%) containing VOCs at ca.. 500 ppb were performed every six weeks, in addition to determining the instrumental background at frequent intervals. Detection limits (in nmol mol^{-1}) and total uncertainties were as follows: methanol (0.46, 12.3%); acetonitrile (0.05, 9.1%); acetone (0.06, 8.8%); acetic acid (0.2, 50%); benzene (0.07, 9.5%); toluene (0.08, 8.6%); sum of C-8 aromatics (0.10, 10.8%) and sum of C-9 aromatics (0.13, 11.1%).

Carbon monoxide, PM_{10}, and $PM_{2.5}$ and meteorological data were measured using gas filter correlation (GFC) non-dispersive infrared (NDIR) technique (Thermo Fischer Scientific 48i trace level enhanced analyser), beta attenuation (Thermo Fischer Scientific 5014i beta continuous ambient particulate monitors) and a meteorological station (Met One Instruments Inc., Rowlett, USA), respectively.

Data from a portable seven-wavelength aethalometer (AE 42, Magee Scientific, USA), that measures at wavelengths- 370 nm, 470 nm, 520 nm, 590 nm, 660 nm, 880 nm and 950 nm, was used to calculate absorption Angstrom exponent (α_{abs}) and BC_{eq} mass loadings. In the aethalometer, ambient air is sucked in at a flow rate of 4 litres per minute through a $PM_{2.5}$ cut-off impactor inlet, and the air is dried using two silica gel scrubbers - the first fitted outside and the second fitted inside the air conditioned container to remove moisture. The instrumental data is acquired at a temporal resolution of 5 minutes. Because the aethalometer collects the aerosol on a quartz filter and collects all $PM_{2.5}$ aerosol including all the light scattering components, data must be carefully corrected for the artifacts that include the filter- loading effect (Arnott et al., 2005; Collaud Coen et al., 2010; Schmid et al., 2006; Virkkula et al., 2007; Weingartner et al., 2003) and the light attenuation caused by scattering aerosol particles embedded in the filter (Arnott et al., 2005; Collaud Coen et al., 2010; Schmid et al., 2006). The Aethalometer data used in this work was corrected by applying Schmid correction procedure, the details of which are discussed in Chapter 2.

3.3.3 Data processing

Half-hour data averages of corrected BC_{eq} mass, $\alpha_{abs(370\text{-}880)}$, and PTR-MS VOC data (including acetonitrile, a biomass combustion tracer used during data analysis) were used. Schmid correction was applied to the 5- minute time resolution aethalometer raw data to calculate BC_{eq}.

$$BCeq = \frac{b_{abs,n}\,(880nm)}{MAC(880nm)} \tag{32}$$

Where, $b_{abs}(880)$ is absorption coefficient and MAC_{880} is mass absorption cross-section, both being measured at 880 nm wavelength.

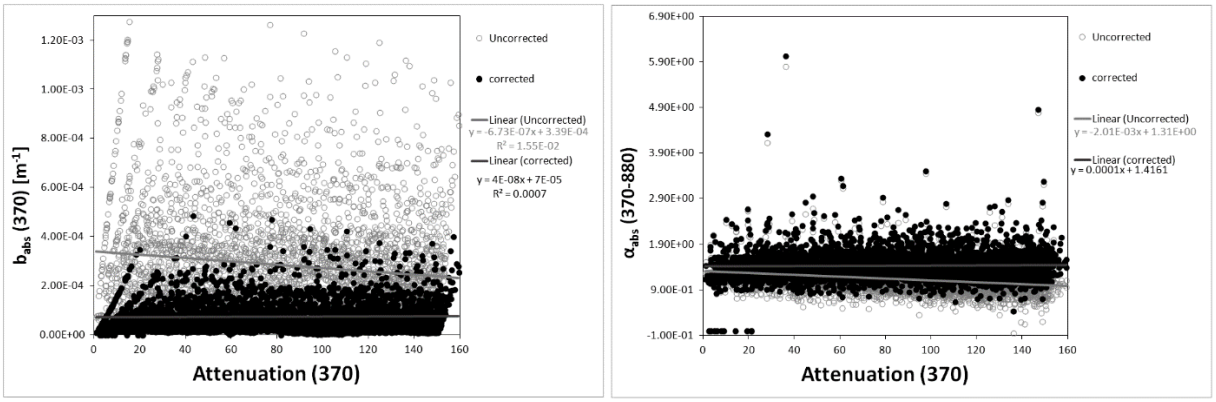

Figure 3.1: Left panel: absorption coefficient ($b_{abs}370$) values before applying correction (grey circles) and after applying correction (black dots) plotted against optical attenuation signal at 370 nm channel. Linear fit equations and R^2 values for b_{abs370} vs. ATN_{370} are shown in grey for uncorrected and in black for corrected. Right panel: angstrom exponent ($\alpha_{abs}370$-880) before applying correction (grey circles) and after applying correction (black dots) against optical attenuation signal of the 370 nm channel. Linear fit equations and R^2 values for $\alpha_{abs}370$-880 vs. attenuation 370 are shown in grey for uncorrected and in black for corrected. Corrected absorption coefficient values and corrected angstrom exponent values don't exhibit any dependence on the optical attenuation values, unlike the uncorrected ones.

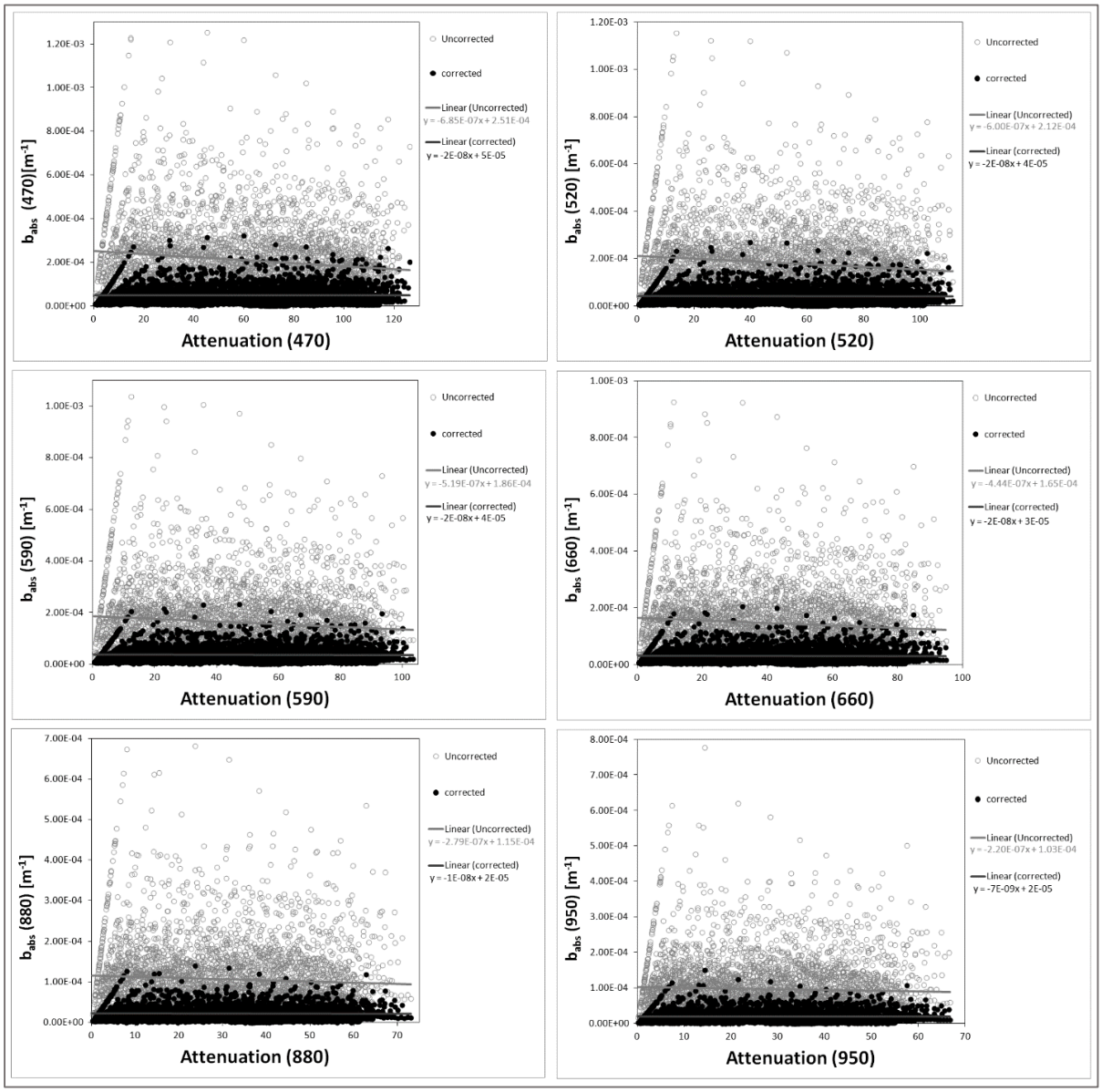

Figure 3.2: Scatter plots showing absorption coefficient (b_{abs}) values before applying correction (grey circles) and after applying correction (black dots) plotted against optical attenuation signal for 6 different wavelength channels- 470nm, 520nm, 590nm, 660nm, 880nm, 950nm . For each plot, linear fit equations and R2 values for b_{abs} vs. attenuation are shown in grey for uncorrected and in black for corrected.

We calculate $b_{abs,n}(\lambda)$ as:

$$b_{abs,n}(\lambda) = \frac{b_{ATN,n}}{(C_{ref}+C_{scat,n})\cdot R_{\omega,n}} = \frac{b_{ATN,n}}{\left(C_{ref}+a_n\cdot\frac{\omega_{0,n}}{1-\omega_{0,n}}\right)\cdot\left[\left(\frac{1}{m\cdot(1-\omega_{0,n})+1}-1\right)\cdot\frac{\ln(ATN_n)-\ln(10)}{\ln(50)-\ln(10)}+1\right]} \quad (33)$$

with

$$a_n = \beta_{scat,n}^{d-1} \cdot c \cdot \lambda^{-\alpha_{scat,n} \cdot (d-1)} \quad (34)$$

where, d=0.564, c = 0.32910−3 [m−1] and $\beta_{scat,n}^{d-1}$=0.4471-1 [m−1] were taken from Arnott and co-workers (Arnott et al., 2005), and m=0.92 and C_{ref} =5.2 were determined such that the slope of the corrected b_{abs} as a function of the ATN is in the range of 0 ± 2 x 10-8[m−1] for all wavelengths (Figure 3.1 left & Figure 3.2). Note that C_{ref} =5.2 is similar to the value reported by Schmid and co-workers (Schmid et al., 2006) for deforestation fires during the SMOCC campaign in the AMAZON basin. Figure 3.3 shows a sequence of filter spot changes at times of relatively stable BC_{eq} mass loadings for each of the biomass burning types to illustrate that the correction algorithm works well in all cases.

The angstrom exponent of the absorbing fraction, after filter loading and scattering correction, was calculated as:

$$\alpha_{abs(370-880)} = -\frac{ln\frac{babs\,(370nm)}{babs\,(880nm)}}{ln\frac{370}{880}} \quad (35)$$

After correction, the absorption angstrom exponent no longer varies as a function of filter loading (Figure 3.1 right). The absorption angstrom exponent calculated using the wavelength pair 370 and 880 nm ($\alpha_{abs(370-880)}$) correlates linearly with the absorption angstrom exponent calculated using the wavelength pairs 370 and 950 nm ($\alpha_{abs(370-950)}$), and 470 nm and 950 nm ($\alpha_{abs(470-950)}$), respectively, with a slope of 1.00 and 1.04 and R^2 of 0.8 and 0.6, respectively, indicating that there is no systematic bias introduced by any of the lamps.

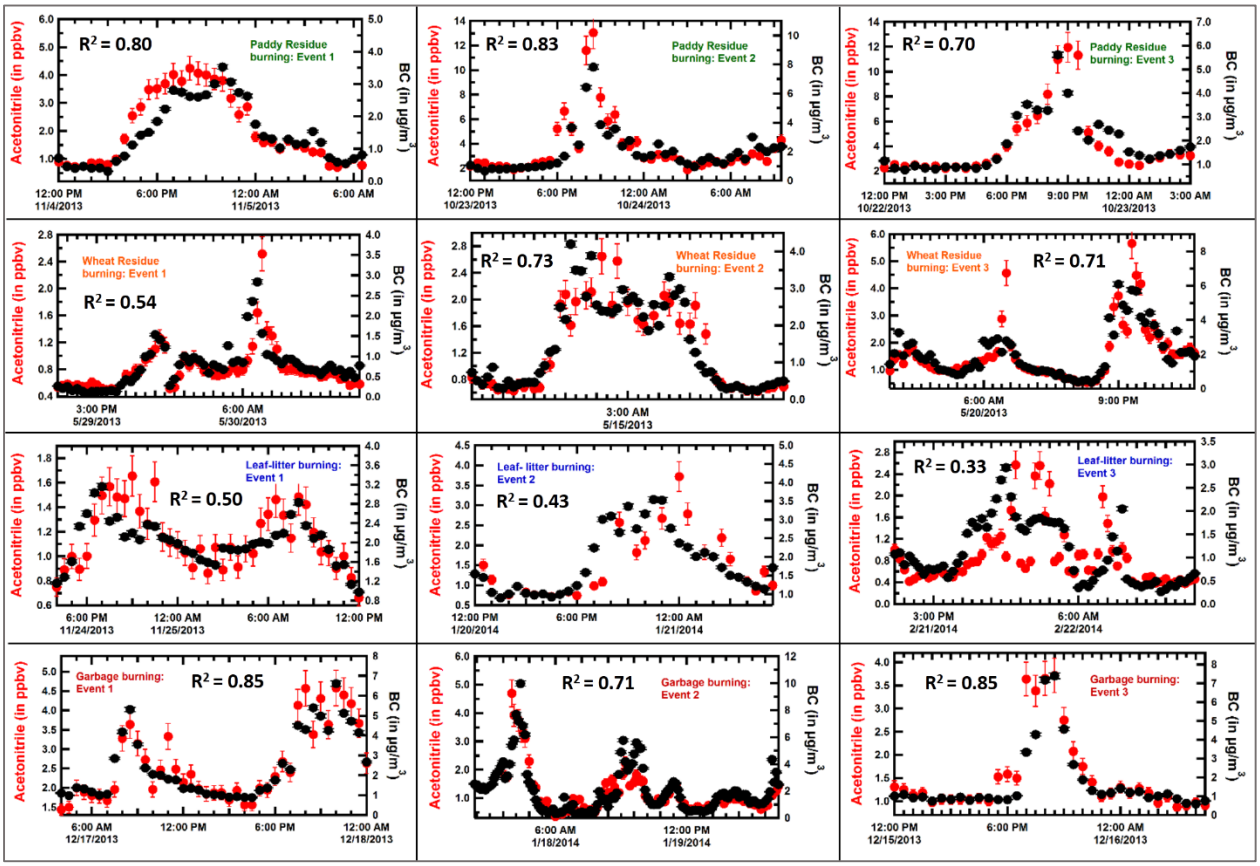

Figure 3.3: Time-profile plots of acetonitrile mixing ratio in ppbv (red dots, left axis) and BC_{eq} concentration in µg/m3 (black dots, right axis) for all biomass burning events. First row: paddy-residue-burning event 1, event 2, and event 3; second row: wheat-residue-burning event 1, event 2, and event 3; third row: leaf-litter-burning event 1, event 2, and event 3; fourth row: garbage-burning event 1, event 2, and event 3. Both the acetonitrile and BC_{eq} concentration mixing ratios are 30- min averaged values.

3.3.4 Selection of biomass burning events

Biomass burning (BB) events (Figure 3.3) were selected on the basis of several criteria. First, the increase of BC_{eq} should coincide with an increase in acetonitrile, which is a well-established biomass combustion tracer (de Gouw et al., 2003; Holzinger et al., 1999; Jost et al., 2003). Second, for the duration of the event, the emission ratio of all aromatic VOCs with respect to acetonitrile and CO should fall onto a single line, indicating that a single source dominates the event. Events caused by a mixture of sources were not considered. Third, for events traced to local sources, we selected only events with a stable wind direction. Moreover, we considered only events that could be attributed to a specific type of biomass combustion, and out of these, we selected three events with the longest continuous time series for each type of BB for this study. The BB events were

classified into different types of BB combustions on the basis of the fact that each type of combustion had unique VOC emission ratios. The identity of the crop residue burning events was confirmed using back- trajectory maps and fire counts (Figure 3.4), as described in Sarkar et al. (Sarkar et al., 2013). Garbage -burning events were identified based on meteorological data, NO measurements, and activity observations. Fresh garbage burning plumes were identified using NO (marker size in Figure 3.5) and originated from two types of sites in the vicinity: one, multiple sites where garbage collectors sort trash to recover recyclables and burn the non-recyclable fraction of waste (mainly kitchen waste (>60%), multi-layered (non-recyclable) plastic packaging, soiled cloth and soiled paper) (Nandy et al., 2015) and the other, a nearby construction site where wooden shelling planks and gunny bags are burned at the end of the business day. Fresh leaf litter burning plumes were observed from the urban sector (Marker size = NO mixing ratio in Figure 3.6), while aged plumes with identical emission ratios, were observed from the industrial and rural sectors. Apart from three events each of the four BB types, three traffic events (Figure 3.4) were also selected to compare the emission profiles of different biomass combustion with fossil fuel combustion. Traffic events (Marker size = NO mixing ratio in Figure 3.7) were selected on the basis of activity data (evening peak traffic hours), wind direction (urban/industrial sector) and emission ratios (weak correlation of BC_{eq} with acetonitrile and strong correlation with aromatic compounds) (Bon et al., 2011; Kourtidis et al., 2002; Kristensson et al., 2004).

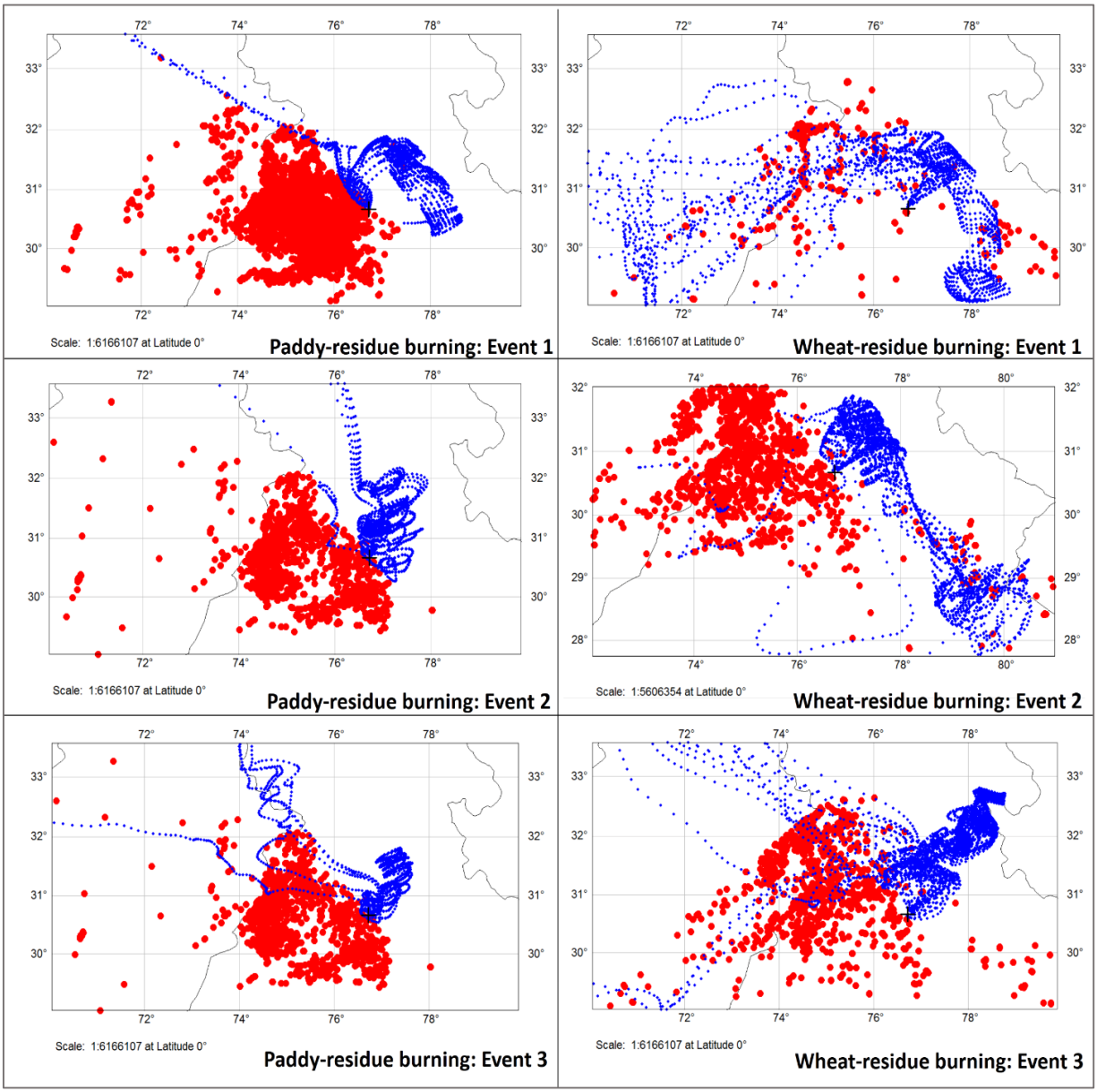

Figure 3.4: 120-hours (HYSPLIT- derived) back- trajectories of air masses (blue markers) that arrived at measurement site during peak of crop-residue burning events plotted along with NASA's MODIS fires (time of the event + previous 120 hours) in red markers. The measurement site in Mohali is marked by black vertical cross. Left stack shows trajectory and fire data for Paddy-residue burning events 1, 2 and 3. Right stack shows trajectory and fire data for Wheat- residue burning events 1, 2 and 3. It can be seen that in case of all the crop-residue burning events, air mass trajectories pass over fires, suggesting contribution of these fires to the composition of these air masses. We thank the NOAA Air Resources Laboratory (ARL) for the provision of the HYSPLIT transport and dispersion model used in this study. We acknowledge the use of FIRMS data from the Land, Atmosphere Near real- time Capability for EOS (LANCE) system operated

by the NASA/GSFC/Earth Science Data and Information System (ESDIS) with funding provided by NASA/HQ.

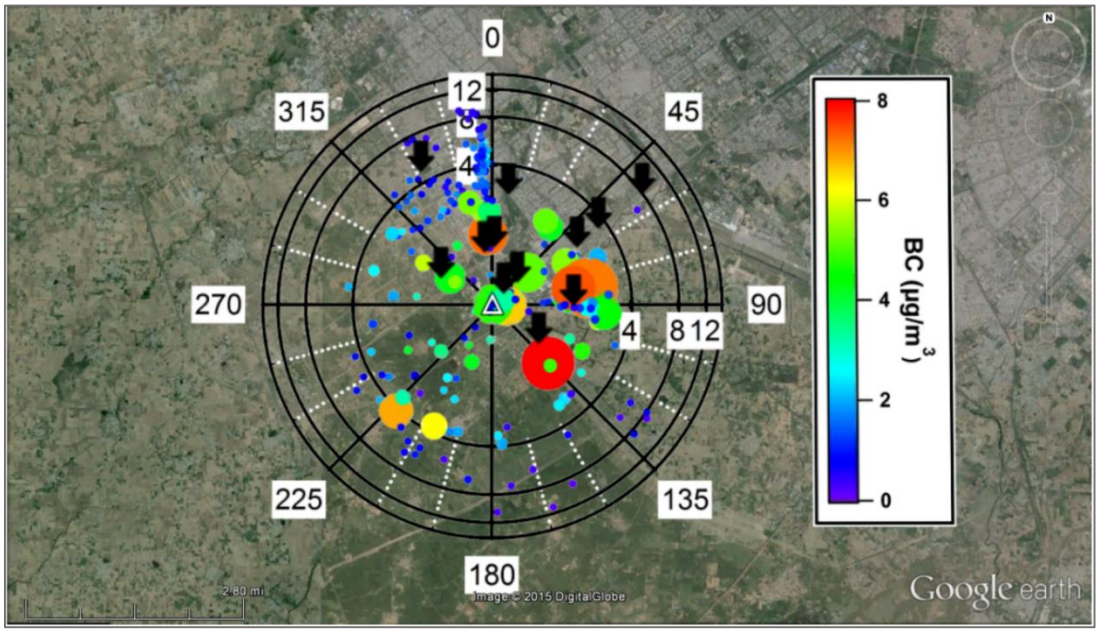

Figure 3.5: Wind rose plot for the three garbage burning events combined has wind speed marked on radius and wind direction marked on angle. Measurement site in the centre of the plot is marked with white triangle. Each marker is coloured with the corresponding BC_{eq} mass (in µg/m3) and is sized according to the associated NO mixing ratio in ppbv. Major garbage/ trash burning sites are marked in bold black arrows. Map image: ©2015 DigitalGlobe, Google earth.

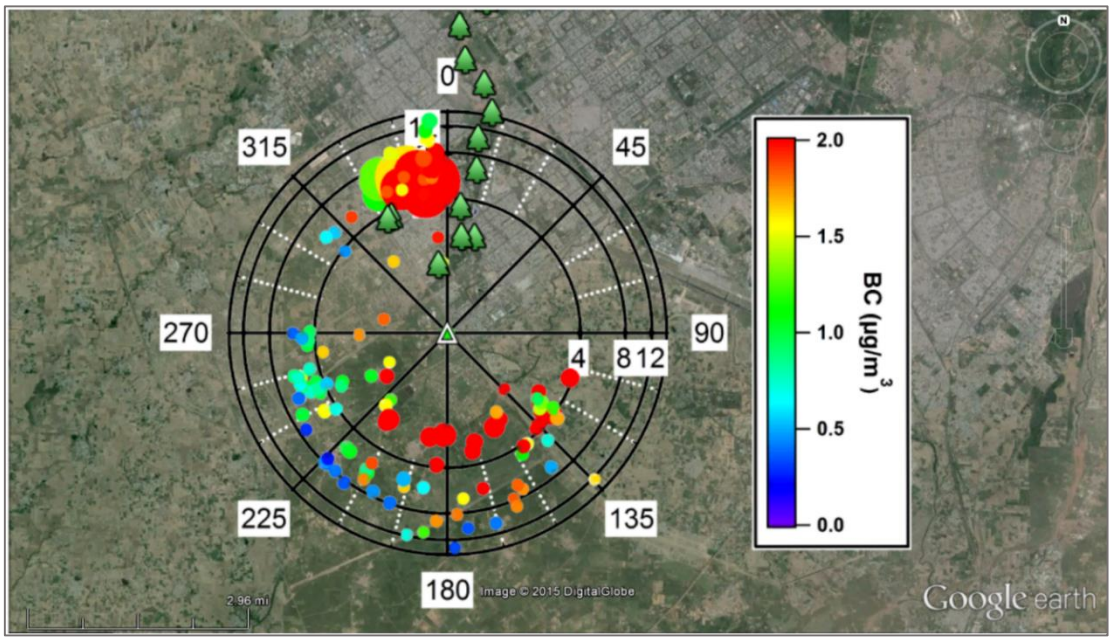

Figure 3.6: Wind rose plot for the three leaf- litter burning events combined has wind speed marked on radius and wind direction marked on angle. Measurement site in the centre of the plot is marked with white triangle. Each marker is coloured with the corresponding BC_{eq} mass (in μg/m3) and is sized according to the associated NO mixing ratio in ppbv. Major parks and gardens are marked with tree symbol. Map image: ©2015 DigitalGlobe, Google earth.

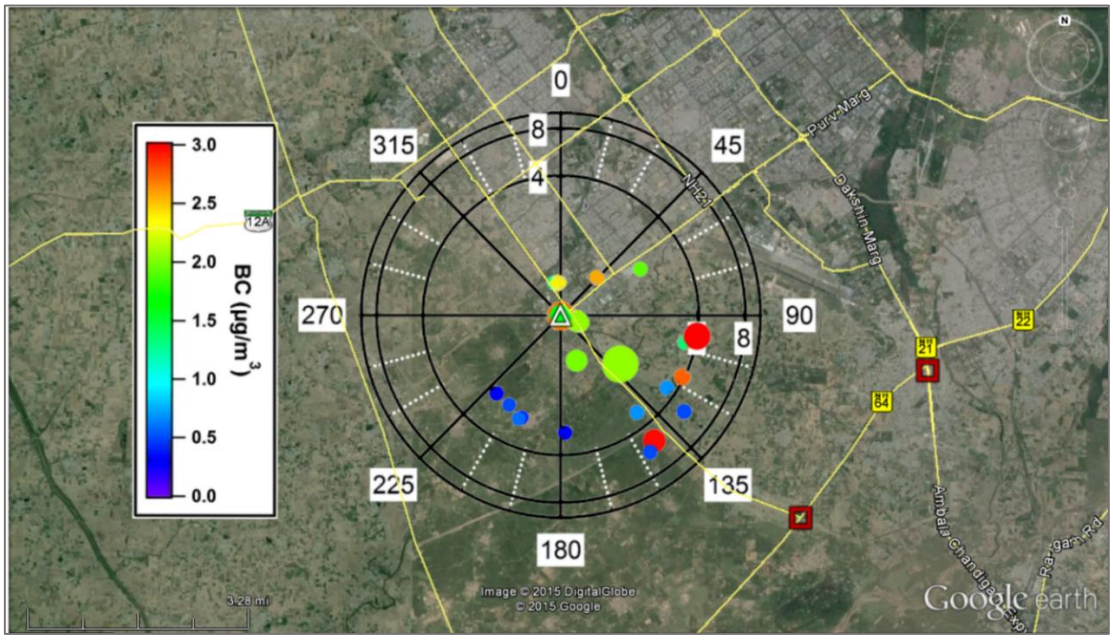

Figure 3.7: Wind rose plot for the three traffic (fossil fuel burning) events combined has wind speed marked on radius and wind direction marked on angle. Measurement site in the centre of the plot is marked with white triangle. Each marker is coloured with the corresponding BC_{eq} mass (in μg/m3) and is sized according to the associated NO mixing ratio in ppbv. Major roads with high-density traffic, including two national highways are marked in yellow lines. Two intersection points of major roads are marked with red squares. Map image: ©2015 DigitalGlobe, © 2015 Google

3.4 Results and Discussion

3.4.1 Correlation of BC_{eq} and Acetonitrile

In all the biomass burning events, BC_{eq} mass and acetonitrile mixing ratio increase simultaneously (Figure 3.3). Because acetonitrile is emitted primarily from biomass burning, this implies that most of the BC_{eq} being measured has the same biomass burning source as acetonitrile. The R^2 between the tracer acetonitrile and BC_{eq} is >0.3 for leaf litter burning, >0.7 for garbage burning, >0.5 for

wheat and >0.7 for paddy residue burning plumes, respectively. For all the traffic events, the increase of BC_{eq} mass coincides with an increase of toluene mixing ratios (R^2>0.8), while at the same time, there is only a weak increase in acetonitrile mixing ratios (Figure 3.8). This indicates that traffic is the main source of the black carbon during these events.

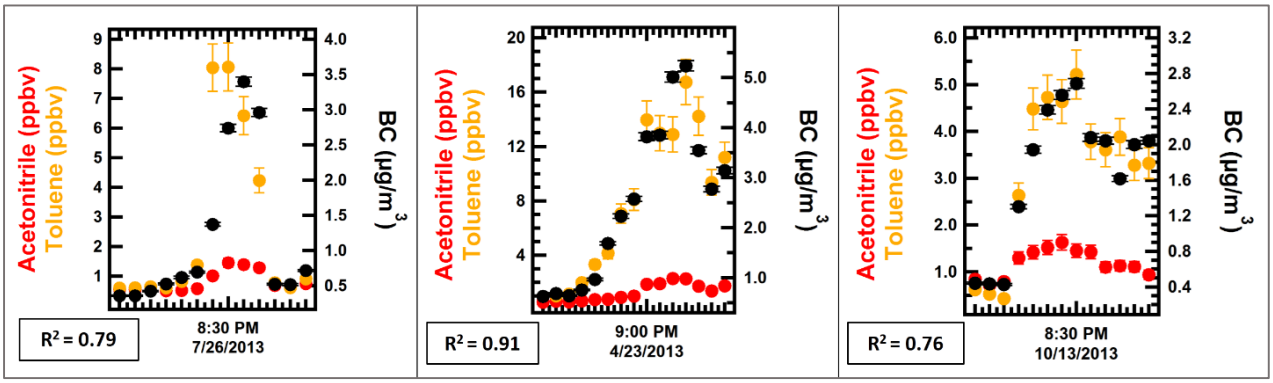

Figure 3.8: Time-profile plots of acetonitrile mixing ratio in ppbv (red dots, left axis), toluene mixing ratio in ppbv (yellow dots, left axis), and BC_{eq} mass-loading in µg/m3 (black dots, right axis) for traffic and fossil-fuel-burning events. From left to right: traffic event 1, traffic event 2, and traffic event 3. Acetonitrile and toluene mixing ratios and BC_{eq} mass loading are 30 min averaged values.

3.4.2 Emission signatures

Figure 3.9 shows the relationship between acetonitrile mixing ratios, the sum of the aromatic compounds and the sum of the OVOCs emitted from the five combustion types. Although no individual emission tracer is suitable to distinguish all combustion events in three dimensions, acetonitrile, aromatics (sum of C-8 aromatics, C-9 aromatics, benzene, toluene) and oxygenated VOCs (sum of methanol, acetone, acetic acid) allow to differentiate between the five sources' signatures. Triplicate events of each of the 5 combustion type show distinct emission signatures. Traffic plumes are characterized by low acetonitrile (<2 ppbv), high aromatics, and moderate OVOCs mixing ratios (Bon et al., 2011). Wheat residue burning plumes are characterized by moderate acetonitrile (typically < 5 ppbv), high aromatics and very high OVOCs mixing ratios (Sinha et al., 2014; Stockwell et al., 2014). Garbage burning plumes are characterized by moderate acetonitrile (typically < 5 ppbv) and moderate OVOCs mixing ratios and high aromatics mixing ratios. Leaf litter burning plumes can be clearly differentiated from these two types of combustions based on the lower mixing ratios of aromatic compounds and moderate OVOCs mixing ratios.

Paddy residue burning plumes are characterized by high mixing ratios of acetonitrile (up to 15 ppbv) and aromatic compounds (Sarkar et al., 2013; Stockwell et al., 2014) and comparatively low OVOCs mixing ratios.

3.4.3 Angstrom exponents for BB and traffic events

Figure 3.10 (top panel) shows absorption angstrom exponent calculated for all the biomass burning events plotted against the benzene/CO-ratio of the plume. Warneke et al. (Warneke et al., 2011) reported real time data for the VOC emissions of a biomass burning fire plume with variable combustion efficiency. Although the emission ratio of all higher- aromatic compounds (toluene, C-8 and C-9 aromatics) and several oxygenated compounds (methanol, acetone and acetic acid), with respect to acetonitrile, did not vary with combustion efficiency and can hence be considered as reliable tracers for the type of fuel burned, the benzene/CO emission ratio changed significantly from the flaming stage, >0.015, towards the smoldering stage, <0.003. In the absence of simultaneous CO_2 measurements, we use this ratio as a proxy for combustion efficiency.

We find that $\alpha_{abs} > 2$ is typical of smoldering conditions, while under flaming conditions, $\alpha_{abs} < 1.4$. This has been confirmed by several recent laboratory studies that reported similar variations of α_{abs} with combustion efficiency (Martinsson et al., 2015; Roden and Bond, 2006). In ambient plumes, α_{abs} is highly variable at the transition between flaming and smoldering combustion stage ($0.003<$Benzene/CO <0.015). As several recent studies reported that fuel moisture affects α_{abs} (Chakrabarty et al., 2015; Laskin et al., 2015), we propose that fuel moisture or variations of the combustion efficiency in different parts of the fire are responsible for modulating α_{abs} in this transition regime. Wheat residue burning plumes consistently show the lower α_{abs}. Wheat residue burning occurs in summer, when ambient temperatures are high (30-45ºC) and the fuel is typically dry and scattered on the field. Leaf litter, on the other hand, generally show higher α_{abs}. in this transition regime. Piles of leaf litter are typically burned in winter, when it is foggy. Garbage has very variable α_{abs} in this transition regime and tends to have an extremely variable composition and moisture content.

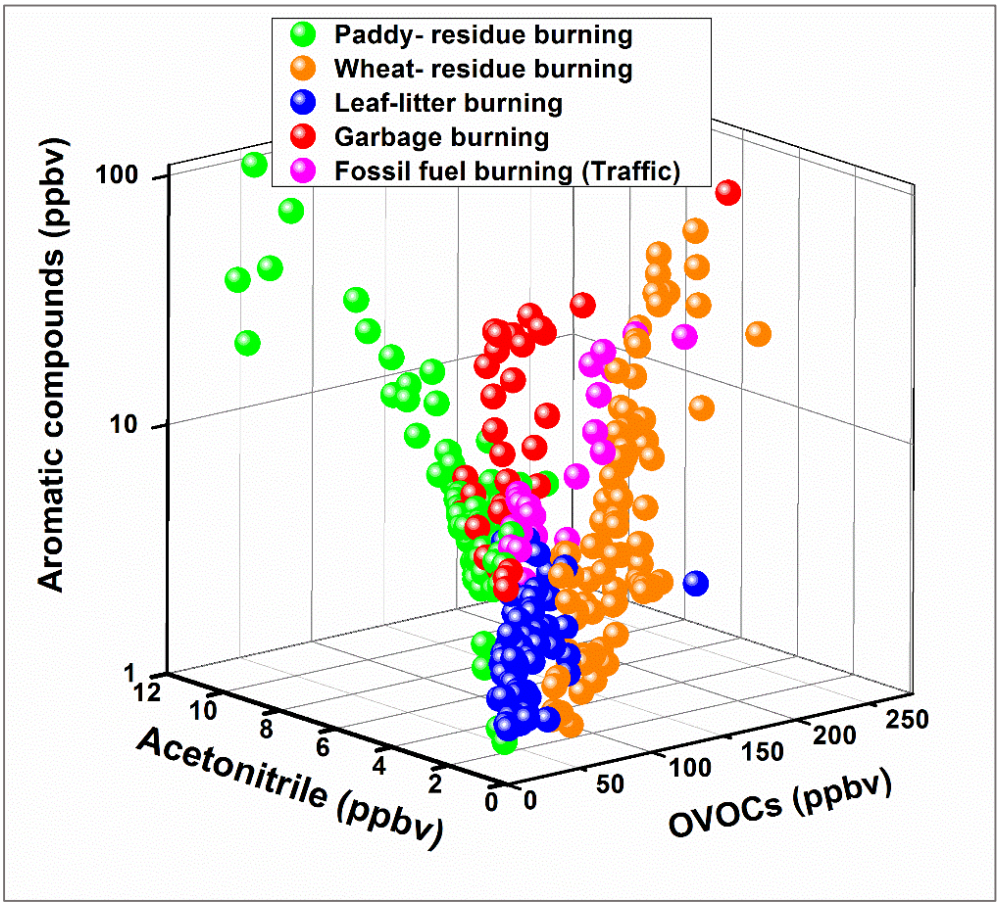

Figure 3.9: Scatter plot (3D) showing the difference in the mixing ratios of different plumes in terms of the mixing ratios of acetonitrile the sum of aromatic compounds and the sum of oxygenated VOCs. Only the data points for which BC_{eq} > +0.5 µg/m3 (the baseline value) are shown.

We find that α_{abs} >2 is typical of smoldering conditions, while under flaming conditions, α_{abs} <1.4. This has been confirmed by several recent laboratory studies that reported similar variations of α_{abs} with combustion efficiency (Martinsson et al., 2015; Roden and Bond, 2006). In ambient plumes, α_{abs} is highly variable at the transition between flaming and smoldering combustion stage (0.003 < Benzene/CO < 0.015). Because several recent studies reported that fuel moisture affects α_{abs} (Chakrabarty et al., 2015; Laskin et al., 2015), we propose that fuel moisture or variations of the combustion efficiency in different parts of the fire are responsible for modulating α_{abs} in this transition regime. Wheat residue burning plumes consistently show the lower α_{abs}. Wheat residue burning occurs in summer, when ambient temperatures are high (30-45ºC) and the fuel is typically dry and scattered on the field. Leaf litter, on the other hand, generally shows higher α_{abs} in this transition regime. Piles of leaf litter are typically burned in winter, when it is foggy. Garbage has

very variable α_{abs} in this transition regime and tends to have an extremely variable composition and moisture content.

Figure 3.10 (bottom panel) shows the absorption angstrom exponent as a function of the BC_{eq} mass fraction of the $PM_{2.5}$ aerosols. It is clear that most data points fall onto one line and that α_{abs} shows correlation with the BC_{eq} mass fraction in the sample. The line intercepts the y-axis at 1.2±0.1. This line demonstrates that the non-BC_{eq} mass fraction in most of plumes shows no strong wavelength dependence of the light absorption. The emission of light absorbing compounds from the fire is correlated with a decline in the combustion efficiencies and equals weakly correlated with an increase in the BC_{eq} mass fraction present in the $PM_{2.5}$ of the plume. Only points from smoldering combustions deviate strongly from the line fit.

Figure 3.10 conveys two crucial points: 1) traffic events and biomass burning events behave similarly with respect to the relationship of the combustion efficiency and the absorption angstrom exponent. 2) α_{abs} values can vary greatly amongst the different events of the same combustion type. This is most obvious for paddy burning events. Event 1 (smoldering combustion) shows α_{abs} values up to 2.5. For this event, α_{abs} correlates with acetonitrile mixing ratios (R^2=0.63) and combustion efficiency (R^2=0.62). Event 3 (transition between flaming and smoldering combustion) shows no correlation between α_{abs} and acetonitrile mixing ratios (R^2=0.02) and α_{abs} <1.5. In our ambient data set, we see that α_{absBB} values as low as 0.9-1.2 coincide with high acetonitrile mixing ratios (2-8 ppbv) in plumes that can be clearly attributed to a certain type of biomass combustion. Such values have previously been reported by Day and co-workers (Day et al., 2006) for pine and poplar wood, and by Lewis and co-workers (Lewis et al., 2008) for Juniper foliage and twigs. We find that the low α_{absBB} in ambient plumes is characteristic for flaming combustion conditions, a result that has been confirmed by several laboratory studies (Martinsson et al., 2015; Roden and Bond, 2006). However, α_{absFF} value should ideally not be greater than 1.1 but at our site, we observe values as high as 1.6 for traffic plumes.

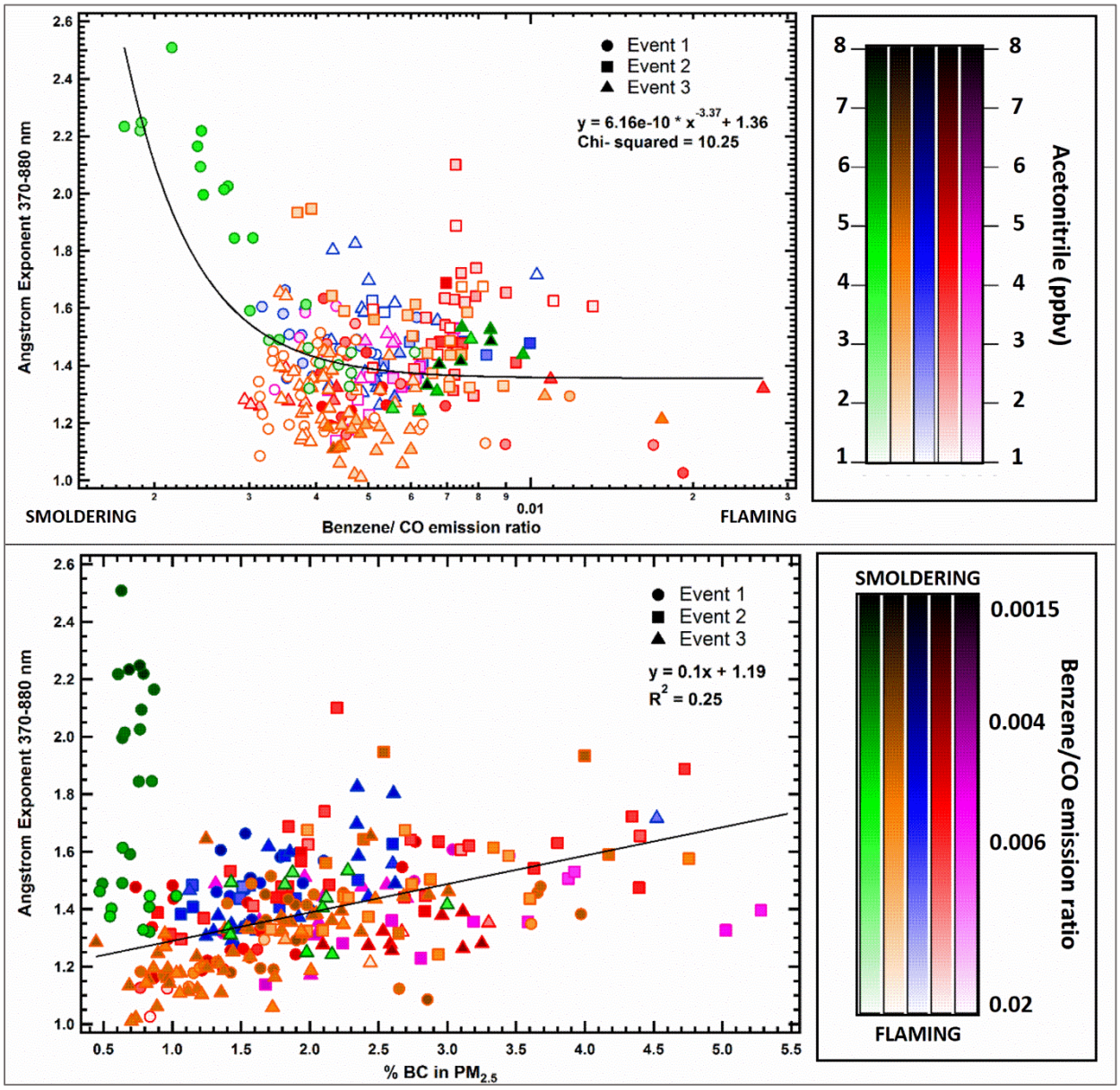

Figure 3.10: Scatter plots showing variation of Angstrom exponent (α370−880) with benzene/CO emission ratio (top) and percent of BC_{eq} in PM2.5 (bottom) for the selected events, with paddy-residue-burning events marked in green, wheat-residue-burning events in orange, leaf-litter-burning events in blue, garbage-burning-events in red, and traffic (fossil-fuel-burning) events in pink. For the top panel, data points are colored according to their corresponding acetonitrile mixing ratios in ppbv. For the bottom panel, data points are colored according to their corresponding benzene/CO emission ratios.

3.5 Conclusion and Outlook

We conclude that in complex environments, where several sources with highly variable combustion efficiencies and variable fuel moisture content contribute toward the black carbon emissions, the application of the two-component aethalometer model algorithm for constraining the contribution of biomass combustion to BC_{eq} mass loadings will yield erroneous results. The source apportionment model may work in a situation where a limited number of tightly regulated sources, with well constrained combustion efficiencies, contribute prominently to the overall BC_{eq} mass, as long as α_{abs} for both sources is determined using independent tracers.

This study is the first to combine real time measurements of gas- phase VOC combustion tracers with BC_{eq} measurements for more specific identification of ambient combustion plumes and seeks to address the validity of present generic approaches in constraining biomass burning sources of BC_{eq} that rely only on BC_{eq} measurements and the wavelength dependence of light absorption for fresh ambient plumes. It is the first to use high-time resolution observations of biomass burning tracers to identify biomass burning events and validate the approach. More research combining high time- resolution aethalometer measurements with combustion tracers, indicators of photochemical air mass age, meteorological parameters and single- particle observations are required to constrain what drives the observed variations of the angstrom exponent α_{abs}, because it is clear from our dataset that the type of BC_{eq} source is not the only factor.

In complex environments with multiple anthropogenic BC_{eq} sources with variable combustion efficiencies and at receptor sites that receive air masses of variable photochemical age, α_{abs} values are not representative of combustion type and therefore, cannot be used to constrain source contributions blindly. Methods that rely on the absorption angstrom exponent for source-apportionment of BC_{eq} at such sites will fail to produce robust results. Instead, more reliable indicators such as C-14 or co-emitted combustion tracers (as demonstrated in this study) should be used to perform source apportionment of BC_{eq}. We find that the currently used two-component aethalometer source-apportionment method cannot be extrapolated to all types of biomass combustion and α_{abs} of traffic plumes can be >1, at least in developing countries like India. The assumption of α_{abs} being a generic indicator for the source of BC_{eq} is not valid. Future research should focus on developing a better understanding of how combustion efficiency, fuel moisture content, photochemical aging and the mixing state of black carbon (in particular coatings acquired during aqueous phase processing) affect the α_{abs}.

Chapter 4

Determining the Contribution of Long-range Transport, Regional and Local Source Areas, to PM_{10} Mass Loading in Hessen, Germany Using a Novel Multi-Receptor Based Statistical Approach

4.1 Abstract

This study uses two newly developed statistical source apportionment models, MuSAM and MuReSAM, to perform quantitative statistical source apportionment of PM_{10} at multiple receptor sites in South Hessen. MuSAM uses multi-site back trajectory data to quantify the contribution of long-range transport, while MuReSAM uses wind speed and direction as proxy for regional transport and quantifies the contribution of regional source areas. On average, between 7.8 and 9.1 $\mu g/m^3$ of PM_{10} (~50%) at receptor sites in South Hessen is contributed by long-range transport. The dominant source regions are Eastern, South Eastern, and Southern Europe. 32% of the PM_{10} at receptor sites in South Hessen is contributed by regional source areas (2.8- 9.41 $\mu g/m^3$). This fraction varies from <20% at remote sites to >40% for urban stations. Sources located within a 2 km radius around the receptor site are responsible for 7% to 20% of the total PM_{10} mass (0.7- 4.4 $\mu g/m^3$). The perturbation study of the traffic flow due to the closing and reopening of the Schiersteiner Brücke revealed that the contribution of the bridge to PM_{10} mass loadings at two nearby receptor sites increased by approximately 120% after it reopened and became a bottleneck, although in absolute terms, the increase is small.

Highlights:

- Long-range transport contributed 50% of the PM_{10} mass at 7 sites in South Hessen

- Dominant source regions were Eastern, South Eastern and Southern Europe
- Regional source areas contributed on average 32% of the PM_{10} mass (2.8- 9.4 $\mu g/m^3$)
- Local source areas contributed 7% to 20% of the PM_{10} mass (0.7- 4.4 $\mu g/m^3$)
- Traffic flow perturbations led to increase in PM_{10} levels at nearby receptor sites

4.2 Introduction

Air pollution is a major public health concern, both in developed as well as developing nations. In most countries, National Air Quality Standards (NAQS) mandate 1 hr, 24 hr and annual exposure limits (Gemmer and Bo, 2013; Guerreiro et al., 2014) for species with health implications. These include particulate matter, carbon monoxide, ozone, oxides of nitrogen, sulphur dioxide, certain volatile organic compounds. Despite implementation of strict environmental laws, urban agglomerations throughout Europe often find it difficult to meet the European Union Air Quality Standard for PM_{10} (Engler et al., 2012; Escudero et al., 2007; Gemmer and Bo, 2013; Guerreiro et al., 2014; Rodriguez et al., 2001; Salvador et al., 2008; Viana et al., 2007), which is currently set at 24- hour average limit of 50 $\mu g/m^3$, which should not be exceeded on more than 35 days per year and an yearly average limit of 40 $\mu g/m^3$, (Anon, 2012; Wolff and Perry, 2010). When a receptor site exceeds the NAQS, the dominant sources (i.e., geographic areas with significant emissions of pollutants) affecting the receptor site need to be identified, in order to implement mitigation measures. This requires analysing the impact of air mass history on the observed pollutant concentration to quantitatively apportion the pollutant's mass at the receptor site to its distant, regional and local source areas.

Fleming and co-workers (Fleming et al., 2012) recently reviewed methods that are currently used to identify sources of air pollution. From their review, it is apparent that powerful statistical tools for identifying the geographical coordinates of distant sources of air pollution do exist. The contribution of specific distant source regions to the observed PM_{10} mass loading at a receptor site is quantified using air mass trajectory data, which can be modelled using meteorological fields (Zeng and Hopke, 1989) or obtained from online trajectory models like HYSPLIT, FLEXPART, etc. (Fleming et al., 2012; Lee and Ashbaugh, 2007; Vasconcelos et al., 1996; Pinxteren et al., 2010). Back-trajectory data is subsequently attributed to sectored geographical area (e.g., cells of a superimposed grid) based on potential source contribution function (PSCF) (Zeng and Hopke, 1989) or residence time analysis (RTA) (Lee and Ashbaugh, 2007; Stohl, 2002). Such RTA

includes the Concentration weighted trajectory (CWT) (Seibert et al., 1994) and residence time weighted concentration (RTWC) maps (Stohl, 1996). All these approaches seek to attribute all of the PM_{10} mass loading observed at a receptor site to spatially distant source areas under the assumption that each grid cell over which the air mass passed in the past 3-5 days prior to reaching the receptor site has an equal probability of being the source of the PM measured at the receptor site. It has been demonstrated that a model based on such an approach produces reliable results only when multiple receptor sites are used to drive the model (Keeler and Samson, 1989; Lee and Ashbaugh, 2007). Generally, the result is produced in the form of a contour map over a gridded array of cells and helps to identify the spatial location of source areas. However, since the meteorological grid of trajectory models is limited (typically the resolution is 0.5°or 1°), such tools are not suitable to identify local and regional source areas with a high spatial accuracy.

A review of the available literature shows that air-mass history- based source apportionment studies of PM_{10} aerosol within the EU throughout the past decades have often focussed on long range transport. As a consequence, PM_{10} exceedance events have frequently been attributed to transboundary air pollution. Several trajectory-analysis based studies concluded that African dust outbreaks were responsible for most of the PM_{10} and $PM_{2.5}$ exceedance events in Spain (Escudero et al., 2007; Rodriguez et al., 2001; Salvador et al., 2008), while high levels of PM_{10} over the UK were attributed to back-trajectory clusters arising over Eastern Europe (Beverland et al., 2000). Pawar et al. (Pawar et al., 2015), in a study on elevated PM mass loadings over the North-West Indo Gangetic basin, on the other hand, concluded that although long- range transport is frequently responsible for extreme exceedance events, it is not responsible for the significant fraction of the annual average PM mass concentration. Recent studies have adopted a more balanced approach and have highlighted that mitigation of local sources which contribute significantly to the baseline level, could very effectively reduce the number of exceedance events (Borrego et al., 2010; Masiol et al., 2010; Pawar et al., 2015), in particular, at sites where local meteorological conditions can amplify the effect of such sources (Engler et al., 2012).

Since the identification of regional or local sources of pollutants is extremely important in view of the intensity and sometimes, promptness of the impact of their emissions (Harrison et al., 1996), we develop and validate a novel statistical model which closes the gap, and identifies regional and local source areas with high spatial accuracy in our current study.

Regional source apportionment until now has mostly been attempted using optical properties (Sandradewi et al., 2008a) or models targeted at the analysis of multivariate chemical data, like Principal Component analysis (Beaver and Palazoglu, 2006; Chan and Mozurkewich, 2007; Hart

et al., 2006; Song et al., 2008), Positive Matrix Factorization (Cheng et al., 2011; Henry and Christensen, 2010; Poirot et al., 2001; Zauscher et al., 2013), EPA's Chemical Mass Balance model (Bhave et al., 2001; Maykut et al., 2003), and EPA's UNMIX model (Poirot et al., 2001; Song et al., 2008) for source- apportionment of measured species. While the former are unreliable in complex environments (Garg et al., 2016), the latter can attribute the PM_{10} mass to different sectors or chemical processes (e.g. transport, industry, windblown dust, gas-to-particle conversion). but are unable to identify the geographical coordinates of specific sources in a spatial context. The spatial information, however, is very crucial for policy makers to plan, implement and monitor the success of mitigation measures.

For individual tracers and sources identified through PMF modelling, wind rose plots and pollution roses have so far been used to attribute the observed mass concentration at the receptor site, to local sources. These plots provide the wind direction in which a strong local source is located upwind of the receptor; however, the distance of the pollution source remains unknown. Bivariate polar plots (Carslaw et al., 2006; Tomlin et al., 2009; Westmoreland et al., 2007) prepared using wind speed- wind direction relationships, could in principle be converted to a distance vector, provided multiple receptors are analyzed jointly. However, till date even those studies that used several pollution roses from multiple stations, did not produce a single coherent map (Carslaw et al., 2006).

In this study, we use our novel modelling approach that employs multi-site datasets containing an air pollutant, wind speed and wind direction from several receptor sites in a constrained region, to demonstrate that we can produce coherent and plausible regional maps. The model output provides maps furnishing the spatial coordinates of local and regional sources within a confined region with a dense ambient air quality network. We named the model- **Mu**lti-receptor **Re**gional **S**ource **A**pportionment **M**odel (MuReSAM) and propose to use the model in combination with the large scale **Mu**lti-receptor **S**ource **A**pportionment **M**odel (MuSAM), which uses back trajectory data to evaluate the large scale air mass transport (Seibert et al., 1994; Stohl, 1996).

We demonstrate the power of our integrated approach towards identifying distant as well as regional and local source areas within a spatial context, using the example of PM_{10} loading measured by the ambient air quality monitoring network: Hessian Agency for Nature Conservation, Environment and Geology of Hessen, a federal state of the Federal Republic of Germany. We quantitatively apportion the PM_{10} mass loadings to distant and regional source areas for seven receptor sites located in South-Hessen. We chose the period from Nov 2014 – July 2015 for the study, as an interesting perturbation event took place when an important bridge called

Schiersteiner Brücke, one of the three important highway crossings of the Rhine River in the densely populated Rhine-Main area, was closed for repair and so the pattern of road traffic changed.

4.3 Experimental

4.3.1 Study area

Hessen is a federal state of the Federal Republic of Germany, located in west-central Germany and has an area of 21,100 km^2, slightly over six million inhabitants and a GDP of 292 billion Euro. Our study is focused on the Rhine-Main Region encompassing South Hessen and part of the neighboring state, Rhineland-Palatine. This is one of the most densely populated and economically active regions in Germany and has the second largest industrial density after the Ruhr area. Hessen's largest city, Frankfurt, is the home of the European Central Bank, the Frankfurt Stock Exchange and a major airport. Figure 4.1 shows that most of the sites used to run the MuReSAM and assess the contributions of regional source areas to PM_{10} in Hessen, are urban stations (11 of 14) located in Hessen's capital, Wiesbaden, the economic centre, Frankfurt and several smaller cities and towns in Hessen (Darmstadt, Fulda, Limburg, Marburg, Michelstadt, Raunheim, Riedstadt, and Wetzlar). Only three remote high- altitude station were available to drive the model in this region: Fürth Odenwald, Kleiner Feldberg (the highest elevation of the Taunus mountain range), and Wasserkuppe (the highest elevation of the Rhön mountain range). The stations used to validate the output of the MuReSAM model, too, are urban stations located in Hessen's capital, Wiesbaden (2), the capital of the neighboring state of Rhineland–Palatine, Mainz (3), which is separated from Wiesbaden only by the Rhine River, Hessen's economic center, Frankfurt (3), an industrial town in Rhineland–Palatine, Ludwigshafen (3), and several smaller cities and towns in Hessen and the neighboring state of Rhineland -Palatine (Darmstadt, Giessen, Heppenheim, Worms and Koblenz).

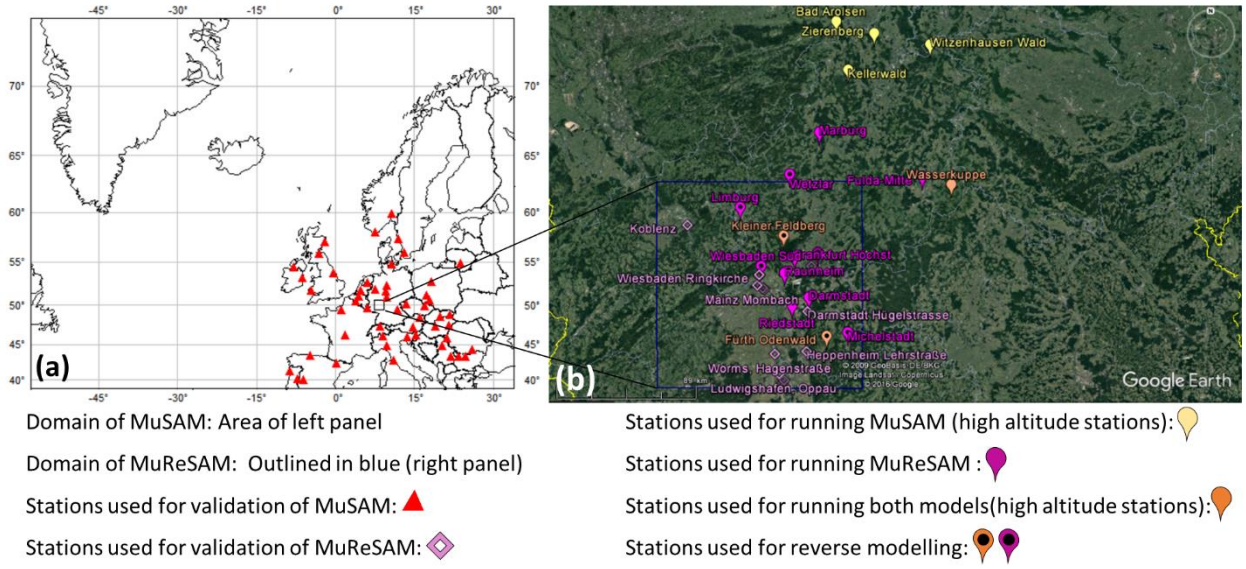

Figure 4.1: (a) MuSAM domain and location of the MuSAM validation stations. (b) MuReSAM domain (blue square) and location of the stations used to drive the MuSAM model (yellow and orange) and MuReSAM model (pink). Stations used to validate the MuReSAM model are marked with light pink diamonds. Stations with a dot within the marker were run in reverse mode.

Hessen also has 42% forest cover, which is concentrated primarily in mountain ranges that are part of the Central German Uplands. Figure 4.1 shows that the remote background sites used to run the MuSAM model and assess the contribution of long- range transport to PM_{10} in Hessen, are all located in the Central German Uplands. These sites include Fürth (Odenwald), Kleiner Feldberg (Taunus), Wasserkuppe (Rhön), Kellerwald, Zierenberg (Habichtswald), Bad Aarolsen and Witzenhausen Wald (Kaufungen Forest).

4.3.2 Meteorological and air quality monitoring data

PM_{10} concentration (in $\mu g/m^3$), wind speed (in m/s), wind direction for different measurement sites (Table 4.1), were taken from the archive data repository of Hessiches Landesamt für Naturschutz, Umwelt and Geologie (HLUG, 2016) to drive the MuReSAM and MuSAM models. In addition, PM_{10} concentration (in $\mu g/m^3$) from the archive data repository of the ZIMEN network of the Landesamt für Umwelt Rheinland-Pfalz (ZIMEN, 2016) were used for model validation purposes.

4.3.3 Trajectory calculation

72 hour back-trajectories arriving at 12o'clock local time at 100 m above ground level (agl) at 12 different receptor sites in Hessen (Fürth Odenwald, Kleiner Feldberg, Wasserkuppe, Kellerwald,

Zierenberg, Bad Arolsen, Witzenhausen Wald, Michelstadt, Limburg, Wetzlar, Wiesbaden Süd and Frankfurt Ost) were obtained from Hybrid Single Particle Lagrangian Integrated Trajectory Model (HYSPLIT) (Draxler and Taylor, 1982; Rolph, 2013; Stein et al., 2015) for the time period: 1 November 2014 to 20 July 2015. One-degree global archive data from Global Data Assimilation System (GDAS) model (2006- present) was used to obtain back– trajectories in the form of hourly trajectory endpoints for 72 hours. The model- derived vertical velocity field was used as the vertical motion method to run HYSPLIT. The details of the sites have been provided in Table 4.1. In Figure 4.1, all sites for which back-trajectories were run, are marked with a black dot inside the site marker; however, only the remote altitude sites that are marked with yellow and orange markers, were used to drive the MuSAM model in the forward mode, as described in section 4.3.4. The back- trajectory runs started above urban stations (pink markers) were used only for the reverse modelling described in section 4.3.7.

Station name	Latitude	Longitude	Altitude (m)	Station type	Data used for:
Darmstadt	49°52'18.61"N	8°39'52.52"E	157	- Urban; commercial, residential	- Running MuReSAM
Frankfurt Höchst	50°6'6.83"N	8°32'31.23"E	101	- Urban; industrial, commercial, residential	- Running MuReSAM
Frankfurt Ost	50°7'29.46"N	8°44'43.05"E	102	- Urban; industrial, commercial	- Running MuReSAM - Determining contribution of long-range transport, regional and local sources
Fulda Mitte	50°32'46.18"N	9°40'48.05"E	285	- Urban; commercial, residential	- Running MuReSAM
Fürth Odenwald	49°39'12.64"N	8°49'2.10"E	475	- Rural; forestry, agriculture	- Running MuReSAM, MuSAM - Determining contribution of long-range transport, regional and local sources
Kleiner Feldberg	50°13'18.77"N	8°26'49.95"E	810	- Rural; forestry, agriculture	- Running MuReSAM, MuSAM - Determining contribution of long-range transport, regional and local sources
Limburg	50°22'58.94"N	8° 3'39.21"E	131	- Urban; commercial, residential	- Running MuReSAM - Determining contribution of long-range transport, regional and local sources
Marburg	50°48'15.34"N	8°46'9.60"E	202	- Urban; commercial, residential	- Running MuReSAM
Michelstadt	49°40'21.02"N	9° 0'7.24"E	205	- Urban; commercial, residential	- Running MuReSAM - Determining contribution of long-range transport, regional and local sources
Raunheim	50°00'37.26"N	8°27'09.73"E	90	- Urban; commercial, residential	- Running MuReSAM - Determining contribution of regional and local sources
Riedstadt	49°49'30.66"N	8°31'0.58"E	89	- Rural; agriculture	- Running MuReSAM
Wasserkuppe	50°29'51.78"N	9°56'9.17"E	938	- Rural; agriculture, forestry	- Running MuReSAM, MuSAM
Wetzlar	50°34'2.10"N	8°30'2.18"E	150	- Urban; industrial, commercial, residential	- Running MuReSAM - Determining contribution of long-range transport, regional and local sources
Wiesbaden Süd	50° 3'1.34"N	8°14'41.68"E	130	- Urban; commercial, residential	- Running MuReSAM - Determining contribution of long-range transport, regional and local sources
Bad Arolsen	51°25'51.23"N	8°55'41.43"E	360	- Rural; agriculture	- Running MuSAM
Kellerwald	51°9'17.44"N	9°1'54.34"E	460	- Rural; recreation	- Running MuSAM
Witzenhausen Wald	51°17'30.34"N	9°46'28.51"E	600	- Rural; forestry, agriculture	- Running MuSAM
Zierenberg	51°21'38.73"N	9°16'16.42"E	489	- Rural; forestry, agriculture	- Running MuSAM
Darmstadt Hügelstrasse	49°52'10.04"N	8°39'13.51"E	158	- Urban; trade, business, living	- Validation of MuReSAM
Franfurt Friedberger Landstrasse	50°7'28.53"N	8°41'30.88"E	119	- Urban; trade, business, living	- Validation of MuReSAM
Giessen Westenlage	50°35'2.80"N	8°40'6.91"E	162	- Urban; trade, business, living	- Validation of MuReSAM
Heppenheim Lehrstrasse	49°38'35.65"N	8°38'31.18"E	110	- Urban; trade, business, living	- Validation of MuReSAM
Wiesbaden Ringkirche	50°4'37.88"N	8°13'49.12"E	145	- Urban; trade, business, living	- Validation of MuReSAM
Wiesbaden Schierstein	50°04'19.63"N	8°13'43.91"E	140	- Urban; business, living	- Validation of MuReSAM

Mainz Mombach	50° 1'2.98"N	8°12'48.79"E	-	- Urban; industrial, commercial, residential	- Validation of MuReSAM
Mainz Citadel	49°59'42.14"N	8°16'25.98"E	-	- Urban; commercial, residential	- Validation of MuReSAM
Mainz Parcustrasse	50° 0'3.75"N	8°15'40.32"E	-	- Urban; commercial, residential	- Validation of MuReSAM
Worms Hagenstrasse	49°37'43.43"N	8°21'53.73"E	-	- Town centre, residential area, close to traffic	- Validation of MuReSAM
Ludwigshafen Oppau	49°30'53.81"N	8°24'8.40"E	-	- Outskirts, industrial area	- Validation of MuReSAM
Ludwigshafen Mundenheim	49°27'19.85"N	8°25'33.25"E	-	- Outskirts, residential area, industrial area	- Validation of MuReSAM
Ludwigshafen Heinigstrasse	49°28'43.32"N	8°26'36.97"E	-	- City centre, residential area, close to traffic	- Validation of MuReSAM
Koblenz Hohenfelder Strasse	50°21'22.12"N	7°35'28.53"E	-	- Town centre, residential area, close to traffic	- Validation of MuReSAM

Table 4.1: List of receptor stations, their site type and GPS coordinates, which were used in the study of regional PM_{10} sources in Hessen. Stations marked with asterisk (*) were used for cluster analysis. High altitude stations are marked with hash (#).

4.3.4 Development, deployment and validation of the Multi-receptor Source Apportionment Model (MuSAM)

We use data from multiple receptor sites in Hessen to demonstrate that by using a novel statistical tool with improved spatial accuracy, the Multi-receptor Source Apportionment Model (MuSAM), it is possible to quantify the impact of distant source regions on the air quality in a receptor region, without relying on pre-existing knowledge such as accurate emission inventories.

To initiate the MuSAM model, the total study area spanning from 38° N to 74° N and from 58° W to 34° E (Figure 4.1) is first divided into grid cells of equal size (1° by 1° each), a subset of the grid (light grey) can be seen in the top panel of Figure 4.2. For every grid cell, the pollutant concentration measured at the receptor when air masses, which previously resided in the grid cell, arrived at any of the receptor sites is summed up (Sum_i), and a count ($Count_i$) of the total number of trajectory segments falling into the cell is maintained. A concentration-weighted average (CWA_i) is calculated for each cell as:

$$\mathrm{CWA}_i = \frac{Sum_i}{Count_i} \tag{36}$$

A separate counter is maintained to count the number of receptor sites that contributed to the CWA_i value of each cell and for the purpose of maintaining spatial accuracy (Lee and Ashbaugh, 2007), only grid cells to which a minimum of three receptor sites contributed, are retained in the final maps. We used HYSPLIT back-trajectory data (see sections 4.3.2 and 4.3.3) and in-situ measured

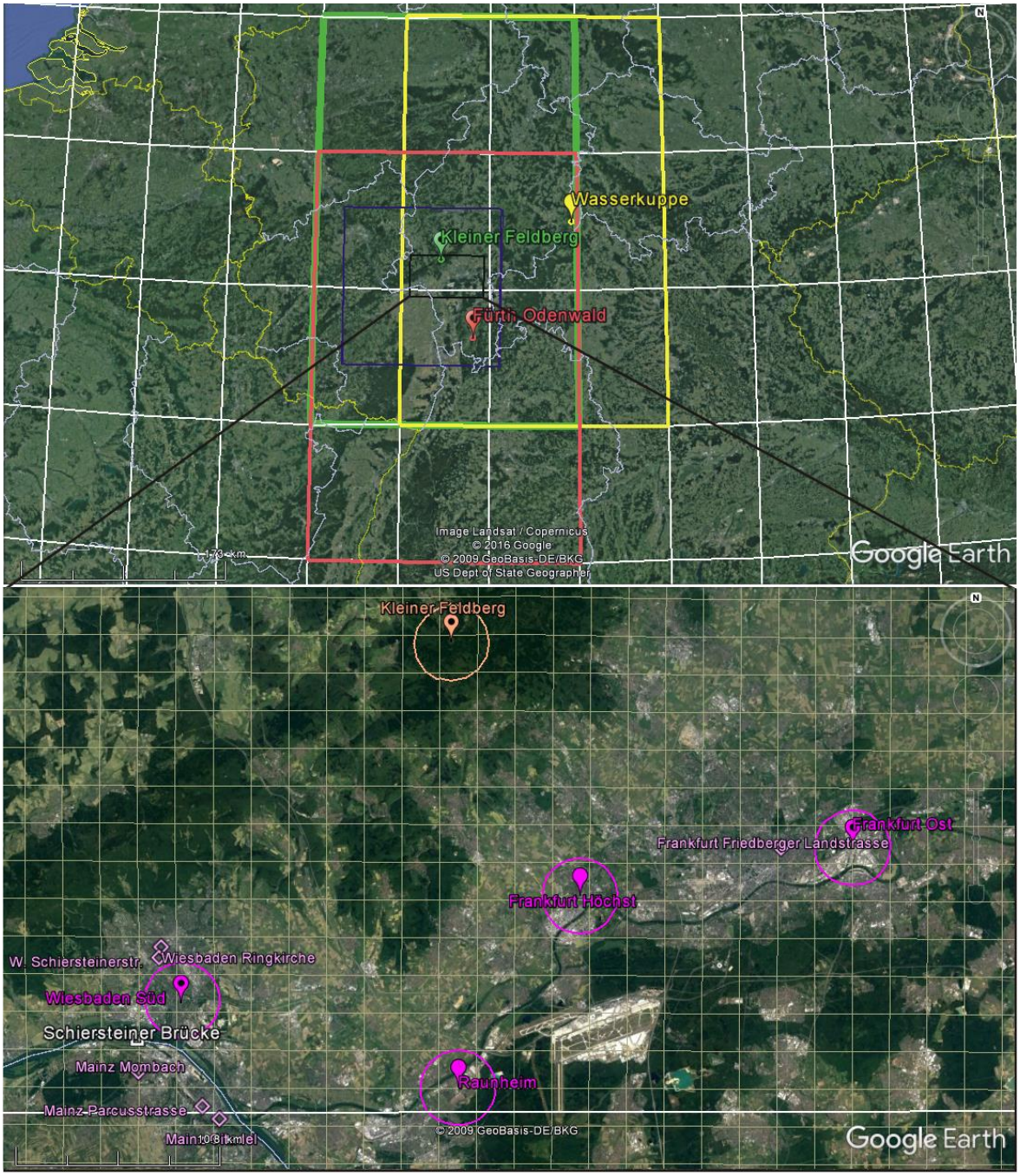

Figure 4.2: The top panel, shows a sub section of the 1°x 1° modelling grid of the MuSAM model (white gridlines), three of the stations used to drive the model and the local domain (small circle around the marker) and regional 3°x3° domain of the same stations (coloured square). The bottom panel shows a sub section of the MuReSAM domain (blue square) which is marked by a black rectangle in the top panel of the figure. The grey gridlines represent the 2 x 2 km grid cells of the MuReSAM model. Stations used to drive the model are indicated by pink (urban) and orange (remote) markers and the local domain of each station is marked with a circle of 2 km radius around each site. Validation stations within this domain (light pink diamonds) and the

Schiersteiner Brücke, (location of our perturbation study indicated by a white square), are also shown.

daily average PM_{10} data from 7 remote measurement sites in Hessen (Kleiner Feldberg, Wasserkuppe, Fürth Odenwald, Bad Arolsen, Kellerwald, Witzenhausen Wald and Zierenberg). We run the model for the time Period 1 November 2014 to 20 July 2015 (excluding 1 January 2015 to avoid bias due to New Year fireworks). Since the focus of large-scale trajectory modelling, is the identification of distant sources, we subtract the likely contribution of regional sources, located within 3°x3° of each of the 7 receptors sites as illustrated in supplementary Figure 4.2 using the following equation:

$$\mathrm{PM}_{10Regional} = PM_{10receptor}\frac{P_{Regional}}{P_{Total}} \quad (37)$$

Where $PM_{10Regional}$ is the PM_{10} mass contributed by regional source areas, $PM_{10receptor}$ is the PM_{10} mass measured at the receptor site and $P_{Regional}$ refers to the number of trajectory endpoints that fall within the 3°x3° box around receptor and P_{Total} is the total trajectory endpoints, respectively. As a consequence of this correction, more than 90% of the observed PM_{10} on days with stagnant conditions and slow transport are attributed to regional sources, while on days with rapid transport, more than 98% of the measured PM_{10} is attributed to sources outside the regional domain. Source apportionment of regional source areas is conducted using a separate high-resolution model (Section 4.3.5).

For validating the model output, we compare the MuSAM output to in-situ measured PM_{10} data from EEA's Airbase stations taken from EEA's website (Anon, n.d.; Horalek et al., 2016). 51 stations classified as background stations by Airbase, were selected across the whole model domain and are shown as red triangles in Figure 4.1. All selected stations had at least 75% data coverage and reported to airbase in the year 2013 (Table 4.2).

Station Name	Country	Station Type	Long, Lat	Altitude (m asl)	Observed annual PM_{10} ($\mu g/m^3$) avg.	Model- predicted avg. PM_{10} ($\mu g/m^3$) transported
Tallaght MPS	Ireland	Background	-6.36, 53.28	99	16.72	8.25
Lough Navar	Ireland	Background	-7.9, 54.44	130	11.32	9.70
Aberdeen	Scotland	Background	-2.09, 57.16	5	13.48	8.34

Edinburgh St Leonards	Scotland	Background	-3.18, 55.95	81	13.54	8.68
Narberth	England	Background	-4.69, 51.78	169	15.65	7.26
Hull Freetown	England	Background	-0.34, 53.75	4	14.26	7.89
Barsbeek-De Veenen	Netherlands	Background	6.02, 52.66	1	18.7	12.62
Dordrecht-Bamendaweg	Netherlands	Background	4.71, 51.8	1	24.06	10.71
43N070-MONS	Belgium	Background	3.94, 50.47	30	27.94	8.30
42R834-BOOM	Belgium	Background	4.38, 51.09	5	25.01	9.63
Walferdange	Luxembourg	Background	6.13, 49.66	230	21.14	8.95
Rouen	France	Background	1.09, 49.44	17	21.97	7.85
Gueret- nicolas	France	Background	1.87, 46.17	437	16.61	6.41
Llanes	Spain	Background	-4.85, 43.44	134	15.39	6.89
ES18883A-Torrelisa	Spain	Background	0.18, 42.46	1005	6.6	14.69
ES1997A-Plasencia	Spain	Background	-6.15, 40.08	181	10.35	9.56
Conde	Portugal	Background	-8.72, 41.31	25	23.8	4.69
Fundao	Portugal	Background	-7.18, 40.14	473	11.41	14.31
gr urss 905301	Italy	Background	11.12, 42.78	10	17.22	29.37
Lugagnano 803306	Italy	Background	9.83, 44.82	210	21.47	18.09
Magadina-Cadenazzo	Switzerland	Background	8.93, 46.16	203	18.56	22.20
Zurich-Kaserne	Switzerland	Background	8.53, 47.38	409	18.62	10.79
Sulzbach-Rosenberg/Lohe	Germany	Background	11.79, 49.49	393	20.88	16.52
Hannover	Germany	Background	9.71, 52.36	85	16.15	9.66
Solling-Sud	Germany	Background	9.55, 51.71	295	13.48	9.66
Bebra	Germany	Background	9.8, 50.97	204	20	12.97
Munster-Geist	Germany	Background	7.61, 51.94	63	22.26	11.19
Keldsnor/9054	Denmark	Background	10.74, 54.75	3	15.99	13.28
Stener Heyerdahl	Norway	Background	7.59, 58.09	12	13.78	9.04
Skoyen	Norway	Background	10.73, 59.92	10	20.08	7.98
Vavihill	Sweden	Background	13.15, 56.03	163	12.99	12.73
Rao	Sweden	Background	11.91, 57.39	10	13.34	12.90
Montana	Bulgaria	Background	23.33, 43.41	160	52.46	27.04
AMS Pleven	Bulgaria	Background	24.62, 43.41	97	41.66	22.88
Celje	Slovenia	Background	15.27, 46.24	240	29.48	19.43
Nova Gorica	Slovenia	Background	13.66, 45.96	113	21.74	12.52
Belgrade	Serbia	Background	20.2, 44.8	74	24.94	15.57
Nis-IJZ	Serbia	Background	21.91, 43.32	224	31.19	26.84
Szazhalombatta	Hungary	Background	18.92, 47.31	99	22.65	20.88
Debrecen Kalotaszeg	Hungary	Background	21.62, 47.51	111	26.74	17.53
TM-3	Romania	Background	21.15, 45.91	119	19.28	20.70
B7 Magurele	Romania	Background	26.03, 44.35	30	31.44	20.14

Vranov nad Toplou- M.R. Stefanika	Slovakia	Background	21.69, 48.89	133	25.37	21.81
Hnusta-Hlavna	Slovakia	Background	19.95, 48.58	320	26.03	25.02
DsOlesnicaPM	Poland	Background	17.39, 51.22	150	31.11	18.35
KpAirplnowr	Poland	Background	18.24, 52.79	85	10.25	9.33
OpOpole3a	Poland	Background	17.92, 50.67	134	29.37	18.35
Dolni Studenky	Czech Republic	Background	16.96, 49.93	298	24.45	23.94
Strojetice	Czech Republic	Background	13.48, 50.17	360	22.71	16.86
Judenburg	Austria	Background	14.68, 47.18	715	17.11	17.91
Ziersdorf	Austria	Background	15.94, 48.53	230	20.54	22.43

Table 4.2: Comparison of average annual PM_{10} concentration in µg/m3 measured in 2013 at European Environment Agency's Airbase stations with PM_{10} concentration in µg/m3 transported from these locations (long-range transport), predicted by MuSAM.

4.3.5 Development, deployment and validation of the Multi-receptor site Regional Source Apportionment Model (MuReSAM)

To identify PM_{10} source areas with a high spatial accuracy, we consider the wind speed and wind direction measured at a receptor site, to be representative of the history of the air mass transport within the region (Fleming et al., 2012) and extend the statistical approach to the regional scale. Using this new statistical tool, the Multi-receptor site Regional Source Apportionment Model (MuReSAM), we identify PM_{10} source areas in South Hessen and quantify the impact of a perturbation of traffic flows on the PM_{10} levels at nearby receptor sites. To initialize the model, our study region, an area of 128 km x 128 km over South Hessen (Figure 4.1), is divided into a 2 km x 2 km grid. In-situ measured half-hourly averaged wind speed (in m/s), wind direction (in degrees) and PM_{10} concentration (in $\mu g/m^3$) data from 14 different measurement stations in Hessen, Germany (marked using pink (urban) and orange (remote background sites) markers in Figure 4.1) for the period November 2014 to July 2015 (excluding the night of Sylvester) were used to drive the model. The air mass is linearly traced back in time for 3 hours, using 3-minute time steps and for every grid cell, a concentration-weighted average (CWA_i) is calculated as described in equation (36).

Each PM_{10} concentration data point ($PM_{10receptor}$) was corrected for the PM_{10} contributed from local sources (PM_{10L}) using residence time analysis, prior to initializing the model. For this correction, the ratio between the number of time steps required to exit the local domain, defined as the area

within a 2 km radius around the site (indicated by a circle around the site in Figure 4.2), and the total number of time steps (N_T) was multiplied with the concentration measured at the receptor site to compute the contribution of local sources to the measured PM_{10}:

$$\mathrm{PM}_{10L} = PM_{10receptor} \frac{N_{SL}}{N_T} \tag{38}$$

The number of time-steps spent by the air mass within the local domain was determined using the measured wind speed according to the equation:

$$\mathrm{N}_{SL} = \frac{r_1}{ws \times t_s} \tag{39}$$

where N_{SL} is the number of time steps required to exit the local domain, r_l is the radius of the local domain [m], ws is the wind speed [m s^{-1}] associated with the air mass and t_S is the duration of one time-step [s].For validating the output of the MuReSAM model, PM_{10} concentration data from a set of 6 stations in Hessen and 8 stations in Rhineland Pfalz (Table 4.1) was obtained from archive data repository of Hessiches Landesamt fur Naturschulz, Umwelt and Geologie, and of Landesamt für Umwelt Rheinland-Pfalz (ZIMEN 2016), respectively. These validation stations were not used for running the model. The PM_{10} concentrations measured at each of these 14 stations over the complete study period were averaged and compared to the model-calculated concentration-weighted average value for the respective station's cell, for the same time period.

4.3.6 Evaluation of the impact of the perturbation of traffic flows on PM_{10} mass loading nearby receptor sites

An important highway bridge for crossing the Rhine River, Schiersteiner Brücke, was closed for repair suddenly on 10 February 2015, forcing commuters to take alternate routes. Before this period, traffic movement was possible, but subjected to speed limits. After 12 April 2015, a single lane of the bridge was re-opened for light and medium weight vehicles, resulting in frequent traffic jams on the bridge and the approach routes. Based on these perturbations in the traffic movement, we divided our dataset into three periods: Period 1 (1 November 2014- 9 February 2015), Period 2 (10 February- 12 April 2015 and Period 3 (13 April – 20 July 2015) and evaluated the impact of the perturbations in the traffic flow on the PM_{10} mass loadings contributed by this source, to the total PM_{10} mass of two nearby receptor sites, Wiesbaden Süd and Raunheim, using MuReSAM reverse modelling.

4.3.7 Reverse modelling using MuSAM and MuReSAM to quantify the contribution of long-range transport, regional sources and local sources

In the technique of reverse modelling, the contribution of each grid cell to the PM_{10} at the receptor site is determined by looking at the air mass history and weighing the PM_{10} mass associated with the respective grid-cell (CWA_i) with the residence time of the air mass over the grid cell, which is proportional to the number of trajectory endpoints in the grid cell (P_i) to compute the contribution of the grid cells to the receptor site.

$$PM_{10}\ transported\ to\ Station\ k = \frac{\Sigma(CWA_i \times P_i)}{P} \quad (40)$$

This allows to quantify the contribution of specific source areas to the observed pollutant concentrations at the receptor sites. Reverse-modelling is applied for each desired receptor station, separately and for regional (MuReSAM) and long range transport (MuSAM), separately.

4.4 Results and Discussion

4.4.1 Quantifying the contribution of long-range transport using MuSAM

The MuSAM map in Figure 4.3a highlights the major source areas of PM_{10} and the relative strengths of their impact on receptor sites in Hessen. Overall, the Eastern and South- Eastern Europe and the Po valley in Italy emerge as source regions of PM_{10} enhancements in Hessen, a fact that is well supported by high PM_{10} mass loadings from in-situ measurements reported to the airbase database of the European Union (Horalek et al., 2016) (Figure 4.3b) and by previous studies using back-trajectory analysis (Beverland et al., 2000; Riuttanen et al., 2013; Salvador et al., 2010). In addition, air masses with a significant residence time over the North Sea and the coast of Norway, are associated with higher PM_{10} mass loadings at receptor sites in Hessen, as compared to air masses originating over pristine regions of the Atlantic Ocean. Enhancements of PM_{10} can also be seen downwind of Iceland, where the Bardabunga volcano erupted from August 2014 till February 2015 and emitted large amounts of SO_2 into the atmosphere. The fact that the PM enhancement occurs downwind rather than at the volcano itself, is indicative of secondary sulfate rather than volcanic ash being the main contributors to PM_{10} mass after the eruption.

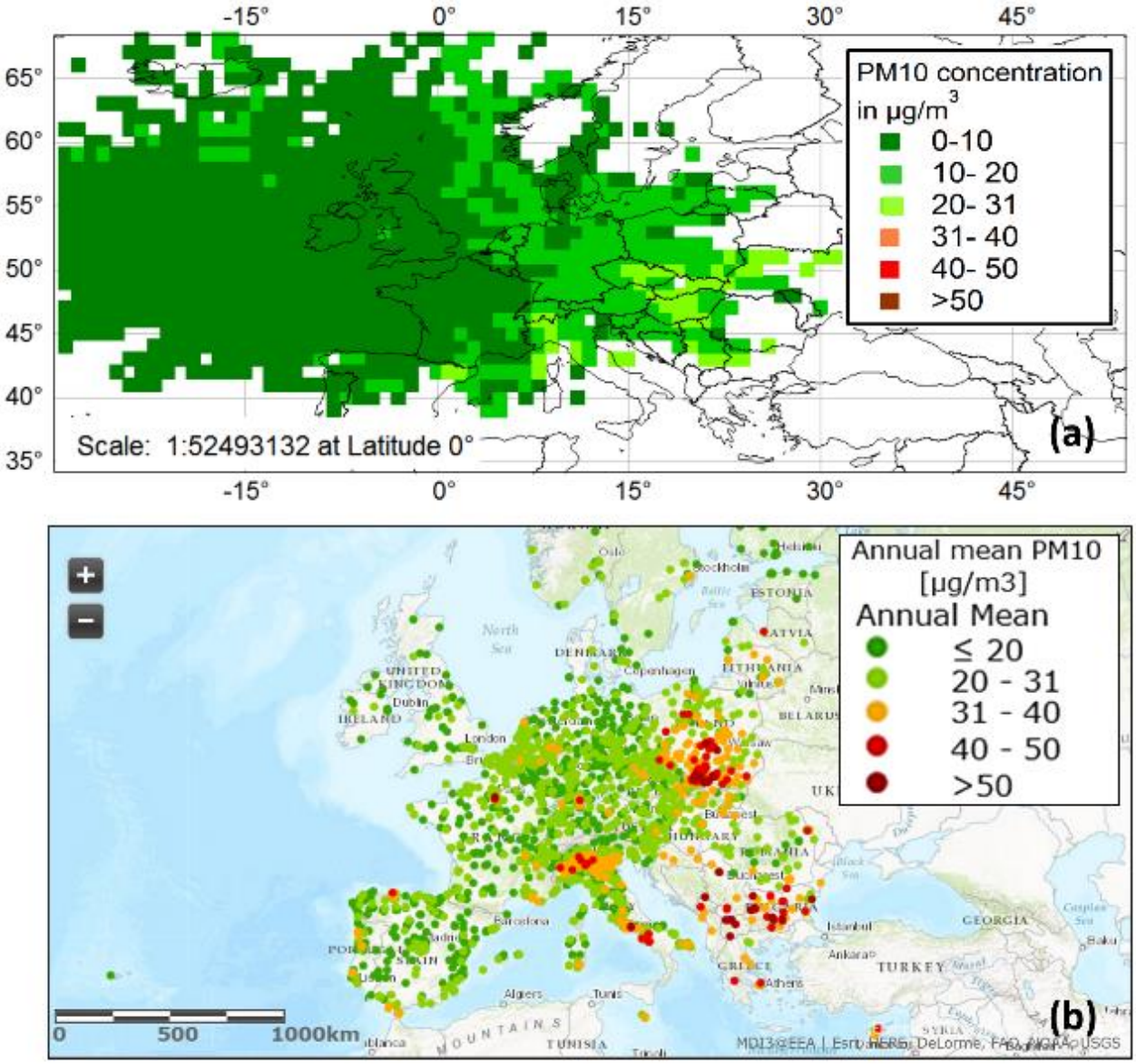

Figure 4.3: (a) MuSAM concentration weighted average map showing PM_{10} (in µg/m3) transported from different regions for the full period of study (b) PM_{10} data (in µg/m3) for the year 2013, measured at European Environment Agency's Airbase stations, taken from EEA's website.

4.4.2 Validation of MuSAM

Comparison of the CWA value of individual pixels of the MuSAM map with the annual average PM_{10} data for the year 2013 for 51 Airbase remote/ background stations with >75% data coverage (Figure 4.4a, Table 4.2) shows that MuSAM under-predicts the in-situ measured PM_{10} mass loading for most sites (slope 0.42, intercept 5.67, R^2=0.29, Figure 4.4b). A similar, but lower under-prediction of the measured values was also observed for maps generated from measurement stations via kriging, i.e. geospatial interpolation of the measured data (Horalek et al., 2016) (slope

of 0.7 and 0.75, and intercept of 5.7 and 6.1 for rural and urban stations, respectively). It can be seen that for many sites in Northern, Eastern and South- Eastern Europe, model- predicted and measured PM_{10} mass loadings agree within ±20%. Most of the stations located West of the receptor site have predicted PM_{10}/observed PM_{10}-ratio of less than 0.8 and severe under-prediction of in-situ measurements (<0.4) can be seen, in particular for coastal sites in Belgium and France.

The likely cause of the under-prediction is that PM_{10} from source regions in Western Europe is frequently washed-out due to rain, prior to the arrival of the air mass at the receptor sites in Germany. Low pressure systems generally originate over the Atlantic and approach the receptor site from the West, North West or South West (Grosswetterlage NWZ,WZ, SWZ, WA TrM according to the Hess-Brezowsky classification (Hess and Brezowsky, 1999; Planchon et al., 2009)) and are frequently associated with rain. On the contrary, air masses originating in North-East, East and Southeast Europe, most frequently reach the receptor sites when there is a high pressure system over North- Eastern, South- Eastern or Eastern Europe (Grosswetterlage SEA, SA, NEA, HFA or HNFA according to the Hess-Brezowsky classification (Hess and Brezowsky, 1999; Planchon et al., 2009)) and are, rarely affected by rainout. It must, therefore, be understood that MuSAM maps quantify the impact of a distant source upon the receptor, rather than the actual concentration present at the distant source.

Over-predictions of in-situ measurements due to the MuSAM model are rare. In-situ measurements are over-predicted by more than 20%, only for 4 out of 51 stations mostly stations in Southern Europe. This could be an indication that transport across the Alps and across the Pyrenees might be associated with a specific synoptic scale transport situation and air masses frequently carry above- average PM_{10} mass loadings due to Saharan dust outbreaks (Salvador et al., 2010). It is also possible that mountain wind systems, which reach wind speeds up to 200 km/h inside the mountain valleys on the Lee side, could be responsible for disproportionate mobilization of legacy sediments by these hot and dry winds in the affected mountain valleys, which might be falsely attributed to source areas on the Luv side of the mountain. In both cases, the apparent impact of the Iberian Peninsula and Italy on receptor sites in Hessen would be overestimated. As a consequence, the model must be used cautiously employed, if transport across a large mountain ranges is involved. In all other cases, the MuSAM model reliably identifies potential source regions of PM_{10} and quantifies their impact on the receptor site.

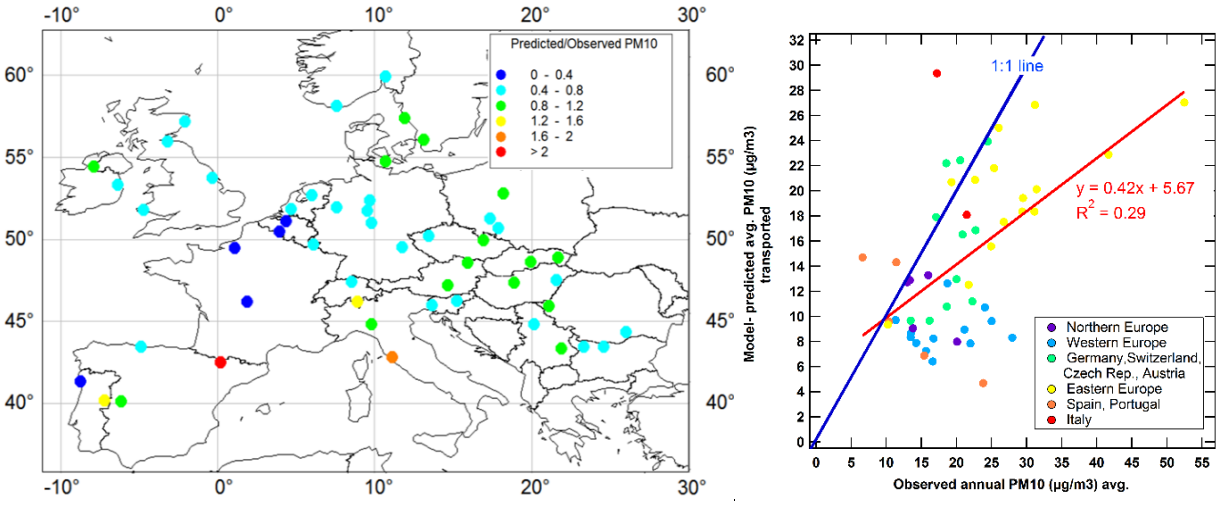

Figure 4.4: (a) Ratio of model-predicted avg. PM_{10} (µg/m3) and observed annual average PM_{10} concentration (µg/m3) measured in 2013 at select European Environment Agency's Airbase stations classified as "background" sites. (b): Predicted vs. observed PM_{10} for the same sites.

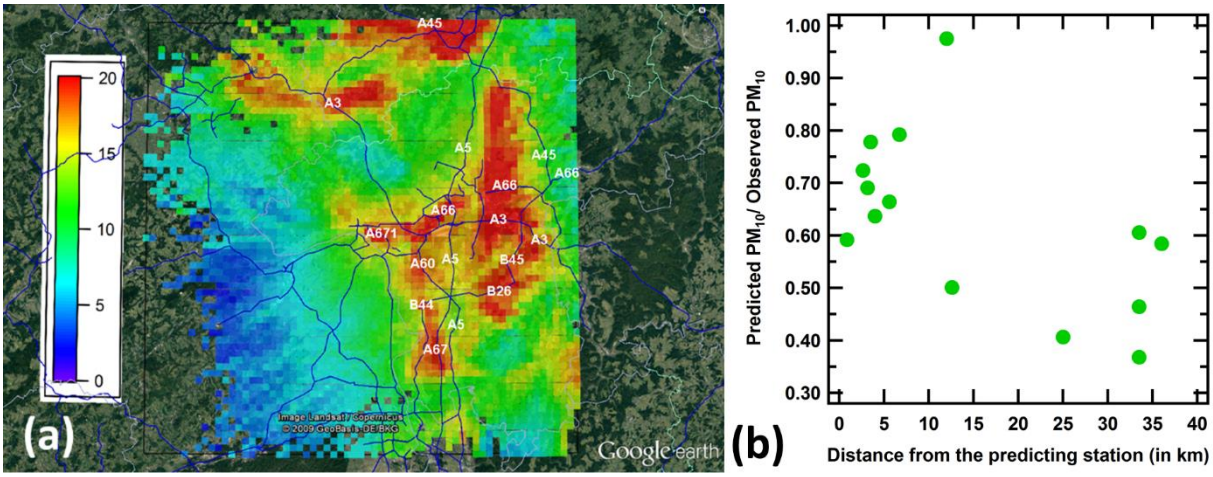

Figure 4.5: (a) MuReSAM-obtained CWA maps for the complete period. Roads are marked in blue. Colorscale on the left shows the PM_{10} concentration attributed to the respective pixel on the map. (b) Ratio of the MuReSAM model-predicted PM_{10} and observed PM_{10} as a function of the distance to the closest predicting station for 14 validation stations in Hessen and Rhineland Pfalz for the complete study period.

4.4.3 Regional and local sources: MuReSAM

The regional map from the MuReSAM model (Figure 4.5a) highlights major highways, highway intersection points, urban areas and forest located in the vicinity of major highways, as the most potent regional source areas of PM_{10}. Highways and major roads are marked with blue lines in Figure 4.5a. Several segments that seem to be potent source areas of PM_{10} were plagued by frequent traffic jams and which in some cases, were worse than usual due to the presence of construction sites during the period of our study. This applies to the A67 between Mannheim and Pfungstadt, the A671 near Wiesbaden Schierstein, the A3 between Hanau and Frankfurt, and the A66 in and around Frankfurt. High PM_{10} values along the B45 and B26 could be an indication that vehicles on long- distance journeys from central Germany towards Southern Germany may have tried to bypass the traffic jams on the highways A3 and A5 in the Rhine-Main Region by exiting the highway A3 ahead of Hanau, heading South on less well- developed regional roads, and catching the highway A5 south of Darmstadt. However, the highest CWA values of PM_{10} coincide with valleys which facilitate trapping of PM_{10} emissions due to a nocturnal inversion (the Lahn valley in which Limburg and Wetzlar, respectively are located, the Wetterau, the Rhine, and the Main valley). Since multiple sources located inside the valleys including combustion sources, traffic, legacy sediments mobilized during springtime ploughing, primary biological aerosol and secondary aerosol, could be responsible for the elevated aerosol burden within the valleys, targeted sampling and chemical analysis of the aerosol and a suitable source receptor model for the analysis of multivariate chemical data would be required to pinpoint the sources of the enhanced aerosol burden. It should be noted that the effect of long-range transport in the form of linear streaks emerging from the boundary of the model domain, can be seen in the model output, indicating that it might be preferable to subtract the contribution of long- range transport from the observed PM_{10} mass, prior to initiating the regional modelling.

4.4.4 Validation of MuReSAM

Figure 4.5b shows the ratio of the MuReSAM-predicted PM_{10} to the observed PM_{10} as a function of the distance to the closest predicting station for 14 validation stations in Hessen and Rhineland Pfalz, which were not used for running the model. In all cases, the model-calculated PM_{10} concentration weighted averages were under-predicted or were close to the observed PM_{10} averages. The model- predicted PM_{10} mass loading was better (within 40% of the actual mass loadings) if the closest predicting station was within 5 km of the predicted station. When the closest predicting station is >20 km from the predicted station, a much smaller fraction (30-60%) of the

in-situ measured PM_{10} is predicted by the MuReSAM model. Overall, MuReSAM did not over predict in-situ measurements for any of the validation station and can therefore be used to constrain the potential impact of specific regional PM_{10} source areas upon the air quality at a receptor site.

Bridge (Source)	Station (Receptor)	Distance b/w station and Bridge [km]	% contribution by bridge to the observed PM_{10} at station		
			Period 1	Period 2	Period 3
Schiersteiner Brücke	Wiesbaden Süd	3.38	14.9	10.9	29.0
	Raunheim	17.23	0.1	0.1	0.2

Table 4.3: Contribution of the pixels in which the bridge is located, to the PM_{10} mass loading measured at two nearby stations.

4.4.5 Evaluation of the impact of the perturbation of traffic flows on PM_{10} mass loading nearby receptor sites

Table 4.3 shows the percentage contribution of Schiersteiner Brücke, to the regional PM_{10} mass loading at 2 near-by receptor sites- Wiesbaden Süd (3.38 km from the bridge) and Raunheim (17.23 km from bridge). The change in traffic movement on and around the bridge over the three periods is directly reflected by the contribution of the pixels in which the bridge is located, to the PM_{10} mass measured at Wiesbaden Süd, which is close to the bridge. In Period 1, before the bridge had to be closed down for repair, Wiesbaden Süd was receiving ~17% of the total measured PM_{10} mass due to traffic movement, construction activities and other sources around the bridge. When the bridge closed down in Period 2, all the traffic was diverted to other channels and only repair work and other sources within the same pixels remained, resulting in a slight decrease of the contribution of this area to the receptor site, to ~12% of the total PM_{10} mass. In Period 3, the bridge opened again, allowing only light weight vehicles to cross the bridge on a single lane and Wiesbaden Süd received 27% of its total PM_{10} from the bridge as the bridge became a bottleneck, obstructing the traffic flow. Compared to Period 2, the relative contribution of the bridge to PM_{10} mass loading of the receptor site- Wiesbaden Süd during Period 3, increased by approximately 120%. However, in absolute terms, the increase in the PM_{10} contributed by this source, to the receptors amounted to ~0.5 $\mu g/m^3$ and <0.1 $\mu g/m^3$, respectively. This case study of a perturbation clearly demonstrates that the impact of changes in ground level emissions on a ground based receptor site is inversely proportional to the distance from the source, and that constricted traffic flow severely increases transport sector emissions.

4.4.6 Reverse modelling and quantification of the contribution of local, regional and distant sources to PM_{10} mass loadings

Figure 4.6 and Table 4.4 summarize the contribution of long-range transport, regional source areas and local sources, to the PM_{10} mass loadings at different measurement stations, estimated by reverse modelling.

Residence time analysis was used for determining contribution from local sources. Residence time analysis indicates that between 0.7 and 4.4 µg/m^3 i.e., 7- 26% of the total measured PM_{10} comes from local sources located within a radius of 2 km around the receptor site. This result is supported by analysis presented above, regarding strong perturbation in the source strength for pixel adjacent to the local domain (distance 3.4 km from the receptor site), producing changes of the same order of magnitude (~0.5 µg/m^3) at a nearby receptor. When the simple subtractive Lenschow approach (Baltensperger, 2016; Lenschow et al., 2001) is applied to the same data set, the estimated traffic-related PM_{10} enhancement within the street canyon at the kerbside location- Frankfurt Ost is estimated to be only 1.1 µg/m^3, while our approach attributes 3.2 µg/m^3 to all sources (including cooking, construction activities and industrial emissions) occurring within a radius of 2 km around the site.

HYSPLIT-derived back- trajectory based modelling attributes between 7.8 and 9.1 µg/m^3 of PM_{10} amounting to 34-83% of the total PM_{10} measured at the receptor to distant source areas. While the absolute numbers are almost equal for all receptor sites as large scale air mass transport typically impacts sites within the same region in a similar manner, the fractional contribution is highest for the remote high altitude stations (66-83%) and lowest for urban stations (34-52%). The fraction of PM_{10} at urban stations attributed to long range transport is comparable to what has been reported in earlier studies for urban stations across Europe (30-80%, (Querol et al., 2004)) and more recently for Leipzig (24 % for $PM_{3.5-10}$ - 71 % for $PM_{0.14-0.42}$, (Pinxteren et al., 2016)), Berlin (50%, (Lenschow et al., 2001)) and Paris (70% of the urban background fine particulate, (Beekmann et al., 2015)). The impact of regional source areas on source apportionment to distant sources was carefully minimized by choosing only remote high altitude sites which have only a small contribution from local and regional source areas, to calculate the concentration field for distant source regions. In addition, residence time analysis was used to subtract the likely impact of regional source areas on the measured PM_{10} from the observed concentration, prior to initiating the model. The Lenschow approach would predict a higher contribution of long-range transport to nearby urban receptors (10 µg/m^3 instead of 8.2 µg/m^3 at Frankfurt Ost), as it attributes all the PM_{10} measured at remote receptor sites like Kleiner Feldberg, to long-range transport. Our

methodology attributes a small fraction of the PM_{10} measured at Kleiner Feldberg to local sources (0.7 µg/m^3 for Kleiner Feldberg), which seems plausible, considering that at the same site, nucleation events were observed almost daily during the FACE-2005 campaign (Dusek et al., 2010) and primary biological aerosol was found to contribute significantly to the water insoluble aerosol inside cloud droplets during FELDEX 95 (Matthias-Maser et al., 2000). Transport of pollution from the nearby urban centers towards the remote receptor (which is predicted to contribute 3.5 µg/m^3 to the average aerosol loadings at Kleiner Felberg by the MuReSAM model) is another aspect that the simple Lenschow approach neglects, although fresh pollution plumes from the nearby Rhine-Main area have been observed at the site (Dusek et al., 2006).

The reverse modelling attributes between 11.9 and 17.6 µg/m^3 of PM_{10} to regional source areas. This amounts to 70-118 % of the total PM_{10} measured at the receptor. As MuReSAM reverse modelling predicts more than the measured PM_{10} for a remote high altitude receptor site located in a forest, and the combination of reverse- modelled PM_{10} contributed by local, regional and distant sources to the PM_{10} measured at the receptor amounts to 130-210% of the total mass, it is likely that the impact of regional source areas on the receptor sites is overestimated. At the present, no correction for the impact of long- range transport has been introduced into the regional model and hence, it very likely overestimates the PM_{10} mass attributed to regional source areas. If the average contribution of long- range transport is subtracted from the estimated contribution of regional source areas, regional source areas contribute between 20% and 44% of the total PM_{10} mass (2.8- 9.4 µg/m^3) to receptor sites in Hessen and the long-range transport corrected reverse modelling explains the observed PM_{10} mass within an uncertainty of less than ±30% for all the receptor sites used for reverse modelling (slope = 0.96, R^2 = 0.8). Two sites deviate significantly from the 1:1 line: Wiesbaden Süd, where only 87% of the PM_{10} mass is accounted for and Kleiner Feldberg where the reverse modelled PM_{10} amounts to 125% of the measured PM_{10}. The former had a significant change in the source strength of a source close to the local domain due to the perturbations caused by the construction site at Schiersteiner Brücke, while the latter is a remote high altitude site. These deviations from the 1:1 line could potentially be reduced by introducing inverse distance weighing into the model. For Frankfurt Ost, the long- range transport- corrected MuReSAM attributes almost the same amount of PM_{10} to regional source areas (9.4 µg/m^3) as the

Lenschow approach attributes to the urban background aerosol (10.1 µg/m^3), indicating that overall, the technique works well.

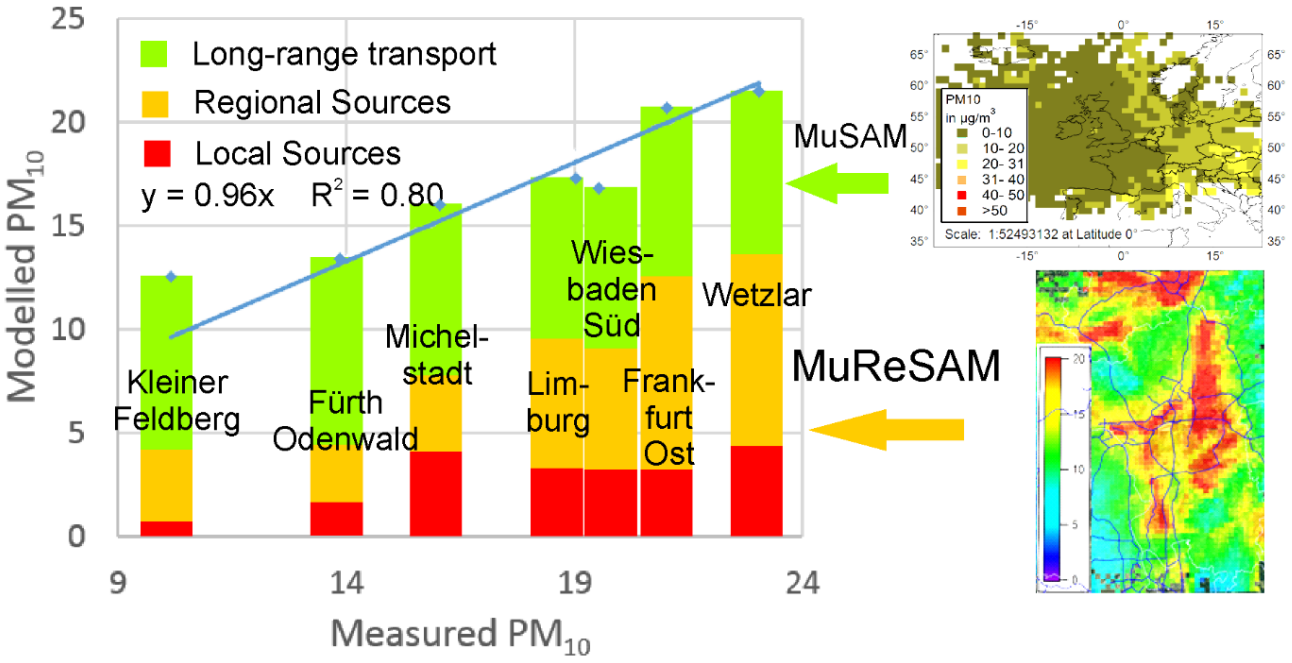

Figure 4.6: Contribution of long-range transport, regional sources and local sources, to total PM10 loading observed at 7 measurement stations in Hessen, calculated using reverse modelling.

		From Reverse modelling			From Residence Time Analysis
Station	**Total PM_{10}**	**Long-range transport (LRT)**	**Regional sources + LRT**	**Regional sources**	**Local sources**
Frank Ost	21.0	8.2	17.6	9.4	3.2
Fürth Odenwald*	13.8	9.1	11.9	2.8	1.6
Kleiner Feldberg*	10.1	8.4	11.9	3.5	0.7
Limburg	19.0	7.8	14.1	6.3	3.3
Michelstadt	16.0	8.3	12.0	3.7	4.1
Wetzlar	23.0	7.9	17.2	9.3	4.4
Wiesbaden Süd	19.5	7.8	13.7	5.9	3.2

Table 4.4: Contribution of long-range transport, regional sources and local sources, to total PM_{10} loading observed at 7 measurement stations in Hessen, calculated using reverse modelling. High altitude stations are marked with asterisk (*).

4.5 Conclusion and Outlook

To our knowledge, this is the first study that uses real-time ambient data from multiple receptor sites, for quantitative statistical source apportionment of PM_{10} to both, distant and regional source areas. Our study provides valuable insights into the strengths and weaknesses of statistical source apportionment modelling. The strength is that such techniques can be deployed even in regions where accurate emission inventories are not available; however, their weakness is that statistical models will always explain all the data used to initiate the model within the statistical framework of the model.

Our case study demonstrates that the derived concentration maps look plausible and rarely over predict the in-situ measured concentrations at distant source regions. A statistical model which seeks to explain measured concentrations only within the frame work of large scale air mass transport, will do so. Overall, this can potentially lead to the misguided conclusion that all the air pollution at the receptor can be blamed on distant source regions alone and local sources have a negligible impact on the air quality at the receptor site. When the same measured time series from the same set of receptors is used to initiate a regional model, the resulting map will look equally plausible and will again rarely overestimate in-situ measurements for the proposed source regions within the regional domain. Ultimately, the measured mass is then explained twice. Once, entirely as a result of regional source areas and the other time, entirely as a result of long range transport. Careful correction for the impact of local and regional source areas can result in accurate source apportionment to distant source areas. A correction for the long range transport component in the regional model helps to accurately attribute regional emissions to their source areas.

Our study shows that on average 51% of the PM_{10} at receptor sites in Hessen is contributed by long range transport and that the contribution of long range transport to the measured PM_{10} varies from >80% at remote sites to ~40% at kerbside stations. Transport of air masses from Eastern, South Eastern and Southern Europe is associated with above average PM_{10} mass loadings at receptor sites in Hessen, while air masses originating over the Atlantic are associated with below average PM_{10} mass loadings. On average, 32% of the PM_{10} at receptor sites in Hessen is contributed by sources within the regional domain. This fraction varies from <20% at remote sites to >40% for urban stations. Densely populated valleys and highways, in particular those under construction, are identified as source regions of elevated PM_{10} at receptor sites. Local sources within 2 km of the receptor site are responsible for 7% to 20% of the total PM_{10} mass.

The perturbation study about Schiersteiner Brücke demonstrates that traffic congestion impacts PM_{10} mass loadings at nearby receptor sites. Mitigation of air pollution due to PM_{10} must involve targeting the design of road and traffic systems such that traffic congestion is avoided and traffic movement remains smooth. Overall, the results indicate that both the models (MuSAM for long-range transport and MuReSAM for regional and local sources) perform well and are useful for source apportionment studies.

Chapter 5

Conclusions: Major findings and Outlook

This thesis presents important findings pertaining to methods for effective source- apportionment of aerosol particles. In Chapter 3, it has been shown clearly that the absorption angstrom exponent is unsuitable for source apportionment of black carbon. The study concludes that in complex environments, where several sources with highly variable combustion efficiencies and variable fuel moisture content contribute toward the black carbon emissions, the application of the widely used source- apportionment method, the two-component aethalometer model algorithm, for constraining the contribution of biomass combustion to BC_{eq} mass loadings will yield erroneous results. The source apportionment model may work in a situation where a limited number of tightly regulated sources, with well constrained combustion efficiencies, contribute prominently to the overall BC_{eq} mass, as long as α_{abs} for both sources is determined using independent tracers.

This study is the first to combine real time measurements of gas- phase VOC combustion tracers with BC_{eq} measurements for more specific identification of ambient combustion plumes and seeks to address the validity of present generic approaches in constraining biomass burning sources of BC_{eq} that rely only on BC_{eq} measurements and the wavelength dependence of light absorption for fresh ambient plumes. It is the first to use high-time resolution observations of biomass burning tracers to identify biomass burning events and validate the approach. More research combining high time- resolution aethalometer measurements with combustion tracers, indicators of photochemical air mass age, meteorological parameters and single- particle observations are required to constrain what drives the observed variations of the angstrom exponent α_{abs}, because it is clear from our dataset that the type of BC_{eq} source is not the only factor.

Moreover, in complex environments with multiple anthropogenic BC_{eq} sources with variable combustion efficiencies and at receptor sites that receive air masses of variable photochemical age, α_{abs} values are not representative of combustion type and therefore, cannot be used to constrain source contributions blindly. Methods that rely on the absorption angstrom exponent for source-apportionment of BC_{eq} at such sites will fail to produce robust results. Instead, more reliable indicators such as C-14 or co-emitted combustion tracers (as demonstrated in this study) should be used to perform source apportionment of BC_{eq}. Findings of the study suggest that the currently used two-component aethalometer source-apportionment method cannot be extrapolated to all

types of biomass combustion and α_{abs} of traffic plumes can be >1, at least in developing countries like India. The assumption of α_{abs} being a generic indicator for the source of BC_{eq} is not valid. Future research should focus on developing a better understanding of how combustion efficiency, fuel moisture content, photochemical aging and the mixing state of black carbon (in particular coatings acquired during aqueous phase processing) affect the α_{abs}.

However, it is clear that elaborate techniques such as C-14 are relatively costly and work only with off-line samples and hence can be only applied for short time periods and in view environments. Likewise, simultaneous observations of BC and elaborate time resolved VOC datasets have been acquired only in few measurement campaigns and have rarely been interpreted jointly. BC measurements and $PM_{2.5}$ or PM_{10} measurements, on the other hand, are relatively easy to execute and can be available in real-time from multiple stations within a constrained region. I therefore, developed a statistical approach to retrieve quantitative source apportionment within a spatial context from high time resolution datasets of PM observations and meteorological data. Chapter 4 presents the study that uses the newly- developed multi- receptor based statistical approach to determine the contribution of long-range transport, regional and, local sources, to PM_{10} mass loading in Hessen, Germany, is the first study that uses real-time ambient data from multiple receptor sites, for quantitative statistical source apportionment of PM_{10} to both, distant and regional sources. This study provides valuable insights into the strengths and weaknesses of statistical source apportionment modelling. The strength is that such techniques can be deployed even in regions where accurate emission inventories are not available; however, their weakness is that statistical models will always explain all the data used to initiate the model within the statistical framework of the model.

The case study presented in this work demonstrates that the derived concentration maps look plausible and rarely over predict the in-situ measured concentrations at distant source regions. A statistical model which seeks to explain measured concentrations only within the frame work of large scale air mass transport, will do so. Overall, this can potentially lead to the misguided conclusion that all the air pollution at the receptor can be blamed on distant source regions alone and local sources have a negligible impact on the air quality at the receptor site. When the same measured time series from the same set of receptors is used to initiate a regional model, the resulting map will look equally plausible and will again rarely overestimate in-situ measurements for the proposed source regions within the regional domain. Ultimately, the measured mass is then explained twice. Once, entirely as a result of regional sources and the other time, entirely as a result of long range transport. Careful correction for the impact of local and regional sources can

result in accurate source apportionment to distant sources. A correction for the long range transport component helps to accurately attribute regional emissions to their source.

This study shows that on average 51% of the PM_{10} at receptor sites in Hessen is contributed by long range transport and that the contribution of long range transport to the measured PM_{10} varies from >80% at remote sites to ~40% at kerbside stations. Transport of air masses from Eastern, South Eastern and Southern Europe is associated with above average PM_{10} mass loadings at receptor sites in Hessen, while air masses originating over the Atlantic are associated with below average PM_{10} mass loadings. On average, 32% of the PM_{10} at receptor sites in Hessen is contributed by sources within the regional domain. This fraction varies from <20% at remote sites to >40% for urban stations. Densely populated valleys and highways, in particular those under construction, are identified as source regions of elevated PM_{10} at receptor sites. Local sources within 2 km of the receptor site are responsible for 7% to 20% of the total PM_{10} mass.

The perturbation study about Schiersteiner Brücke demonstrates that traffic congestion has a profound impact on PM_{10} mass loadings at nearby receptor sites. Mitigation of air pollution due to PM_{10} must involve targeting the design of road and traffic systems such that traffic congestion is avoided and traffic movement remains smooth. Overall, the results indicate that both the models (MuSAM for long-range transport and MuReSAM for regional and local sources) perform well and are useful for source apportionment studies.

List of figures

List of tables

Bibliography

Alexander, D. T. L., Crozier, P. a and Anderson, J. R.: Brown Carbon Spheres in East Asian Outflow and Their Optical Properties, Science (80-.)., 321(5890), 833–836, doi:10.1126/science.1155296, 2008.

Anderson, J. O., Thundiyil, J. G. and Stolbach, A.: Clearing the Air : A Review of the Effects of Particulate Matter Air Pollution on Human Health, J. Med. Toxicol., 8, 166–175, doi:10.1007/s13181-011-0203-1, 2012.

Andreae, M. O.: Correlation between cloud condensation nuclei concentration and aerosol optical thickness in remote and polluted regions, Atmos. Chem. Phys., 9, 543–556, 2009.

Andreae, M. O. and Gelencser, A.: Black carbon or brown carbon ? The nature of light-absorbing carbonaceous aerosols, Atmos. Chem. Phys., 6(10), 3131–3148, 2006.

Anon: IPCC Second Assessment Climate Change 1995., 1995.

Anon: EEA, 2012: Air quality in Europe. Technical Report 4., 2012.

Anon: European Environment Agency's map for Particulate Matter (PM10): annual mean concentrations in Europe in the year 2013, [online] Available from: http://www.eea.europa.eu/themes/air/interactive/pm10, n.d.

Anon: Purdue University- Radiological and Environmental Management: Scanning Electron Micrsoscope, Purdue Mark. Media [online] Available from: https://www.purdue.edu/ehps/rem/rs/sem.htm, n.d.

Arnott, W. P., Hamasha, K., Moosmüller, H., Sheridan, P. J. and Ogren, J. a.: Towards Aerosol Light-Absorption Measurements with a 7-Wavelength Aethalometer: Evaluation with a Photoacoustic Instrument and 3-Wavelength Nephelometer, Aerosol Sci. Technol., 39, 17–29, doi:10.1080/027868290901972, 2005.

Bai, Y., Brugha, R. E., Jacobs, L., Grigg, J., Nawrot, T. S. and Nemery, B.: Carbon loading in airway macrophages as a biomarker for individual exposure to particulate matter air pollution — A critical review, Environ. Int., 74, 32–41, doi:10.1016/j.envint.2014.09.010, 2015.

Baker, J.: A cluster analysis of long range air transport pathways and associated pollutant

concentrations within the UK, Atmos. Environ., 44(4), 563–571, doi:10.1016/j.atmosenv.2009.10.030, 2010.

Baltensperger, U.: Spiers Memorial Lecture, Faraday Discuss., 189, 9–29, doi:10.1039/C6FD00065G, 2016.

Bange, H. W. and Williams, J.: New directions: Acetonitrile in atmospheric and biogeochemical cycles, Atmos. Environ., 34(28), 4959–4960, 2000.

Beaver, S. and Palazoglu, A.: Cluster Analysis of Hourly Wind Measurements to Reveal Synoptic Regimes Affecting Air Quality, J. Appl. Meteorol. Climatol., 45(12), 1710–1726, doi:10.1175/JAM2437.1, 2006.

Beekmann, M., Prévôt, A. S., Drewnick, F., Sciare, J., Pandis, S. N., Denier Van Der Gon, H. A., Crippa, M., Freutel, F., Poulain, L., Ghersi, V. and Rodriguez, E.: In situ, satellite measurement and model evidence on the dominant regional contribution to fine particulate matter levels in the Paris megacity, Atmos. Chem. Phys., 15(March), 9577–9591, doi:10.5194/acp-15-9577-2015, 2015.

Bergstrom, R. W., Russell, P. B. and Hignett, P.: On the Wavelength Dependence of the Absorption of Black Carbon Particles : Predictions and Results from the TARFOX Experiment and Implications for the Aerosol Single Scattering Albedo, J. Atmos. Sci., 59(3), 567–577, 2002.

Beverland, I. J., Tunes, T., Sozanska, M., Elton, R. A., Agius, R. M. and Heal, M. R.: Effect of long-range transport on local PM10 concentrations in the UK, Int. J. Environ. Health Res., 10(3), 229–238, doi:10.1080/09603120050127176, 2000.

Bhave, P. V, Prather, K. A. and Cass, G. R.: Source Apportionment of Fine Particulate Matter by Clustering Single-Particle Data : Tests of Receptor Model Accuracy, Environ. Sci. Technol., 35(10), 2060–2072, 2001.

Blake, R. S., Monks, P. S. and Ellis, A. M.: Proton Transfer Reaction Mass Spectrometry, J. Chem. Rev., 109(3), 861–896, doi:10.1021/cr800364q, 2009.

Boersema, J. J. . and Reijnders, L., Eds.: Principles of Environmental Sciences, Edward Elgar Publishing., 2009.

Bon, D. M., Ulbrich, I. M., de Gouw, J. A., Warneke, C., Kuster, W. C., Alexander, M. L., Baker,

A., Beyersdorf, A., Blake, D. R., Fall, R., Jimenez, J. L., Hermdon, S., Huey, L. G., Knighton, W. D., Ortega, J., Springston, S. and Vargas, O.: Measurements of volatile organic compounds at a suburban ground site (T1) in Mexico City during the MILAGRO 2006 campaign: measurement comparison, emission ratios, and source attribution, Atmos. Chem. Phys., 11(6), 2399–2421, 2011.

Bond, T. C.: Spectral dependence of visible light absorption by carbonaceous particles emitted from coal combustion, Geophys. Res. Lett., 28(21), 4075–4078, doi:10.1029/2001GL013652, 2001.

Bond, T. C. and Bergstrom, R. W.: Light Absorption by Carbonaceous Particles: An Investigative Review, Aerosol Sci. Technol., 40(1), 27–67, doi:10.1080/02786820500421521, 2006.

Bond, T. C., Doherty, S. J., Fahey, D. W., Forster, P. M., Berntsen, T., Deangelo, B. J., Flanner, M. G., Ghan, S., Kärcher, B., Koch, D., Kinne, S., Kondo, Y., Quinn, P. K., Sarofim, M. C., Schultz, M. G., Schulz, M., Venkataraman, C., Zhang, H., Zhang, S., Bellouin, N., Guttikunda, S. K., Hopke, P. K., Jacobson, M. Z., Kaiser, J. W., Klimont, Z., Lohmann, U., Schwarz, J. P., Shindell, D., Storelvmo, T., Warren, S. G. and Zender, C. S.: Bounding the role of black carbon in the climate system: A scientific assessment, J. Geophys. Res. Atmos., 118(11), 5380–5552, doi:10.1002/jgrd.50171, 2013.

Borghesi, A. and Guizetti, G.: Graphite (C), in Handbook of Optical Constants of Solids, Volume II, edited by E. D. Palik, pp. 449–460, Academic Press, Boston, MA., 1991.

Borrego, C., Valente, J., Carvalho, A., Sa, E., Lopes, M. and Miranda, A. I.: Contribution of residential wood combustion to PM10 levels in Portugal, Atmos. Environ., 44(5), 642–651, doi:10.1016/j.atmosenv.2009.11.020, 2010.

Boucher, O., Randall, D., Artaxo, P., Bretherton, C., Feingold, G., Forster, P., Kerminen, V.-M., Kondo, Y., Liao, H., Lohmann, U., Rasch, P., Satheesh, S. K., Sherwood, S., Stevens, B. and Zhang, X.-Y.: Clouds and Aerosols, in Climate Change 2013: The Physical Science Basis. Contribution of Working Group I to the Fifth Assessment Report of the Intergovernmental Panel on Climate Change, edited by T. F. Stocker, D. Qin, G.-K. Plattner, M. Tignor, S. K. Allen, J. Boschung, A. Nauels, Y. Xia, V. Bex, and P. M. Midgley, Cambridge University Press, Cambridge, United Kingdom and New york, NY, USA., 2013.

Brown, J. S., Zeman, K. L. and Bennett, W. D.: Ultrafine Particle Deposition and Clearance in the Healthy and Obstructed Lung, Am. J. Respir. Crit. Care Med., 116, 1240–1247,

doi:10.1164/rccm.200205-399OC, 2002.

Carslaw, D. C., Beevers, S. D., Ropkins, K. and Bell, M. C.: Detecting and quantifying the contribution made by aircraft emissions to ambient concentrations of nitrogen oxides in the vicinity of a large international airport, Atmos. Environ., 40(28), 5424–5434, 2006.

Chakrabarty, R. K., Moosmüller, H., Chen, L. W. a, Lewis, K., Arnott, W. P., Mazzoleni, C., Dubey, M. K., Wold, C. E., Hao, W. M. and Kreidenweis, S. M.: Brown carbon in tar balls from smoldering biomass combustion, Atmos. Chem. Phys., 10(13), 6363–6370, doi:10.5194/acp-10-6363-2010, 2010.

Chakrabarty, R. K., Gyawali, M., Yatavelli, R. L. N., Pandey, A. and Watts, A. C.: Dominance of brown carbon in aerosol emissions from burning of boreal peatlands, Atmos. Chem. Phys. Discuss., 15, 28793–28813, doi:10.5194/acpd-15-28793-2015, 2015.

Chan, T. W. and Mozurkewich, M.: Application of absolute principal component analysis to size distribution data : identification of particle origins, Atmos. Chem. Phys., 7(3), 887–897, 2007.

Cheng, Y., He, K. B., Zheng, M., Duan, F. K., Du, Z. Y., Ma, Y. L., Tan, J. H., Yang, F. M., Liu, J. M., Zhang, X. L., Weber, R. J., Bergin, M. H. and Russell, a. G.: Mass absorption efficiency of elemental carbon and water-soluble organic carbon in Beijing, China, Atmos. Chem. Phys., 11(22), 11497–11510, doi:10.5194/acp-11-11497-2011, 2011.

Clarke, A., McNaughton, C., Kapustin, V., Shinozuka, Y., Howell, S., Dibb, J., Zhou, J., Anderson, B. E., Brekhovskikh, V., Turner, H. and Pinkerton, M.: Biomass burning and pollution aerosol over North America: Organic components and their influence on spectral optical properties and humidification response, J. Geophys. Res. Atmos., 112(D12), doi:10.1029/2006JD007777, 2007.

Clayton, G. D., Arnold, J. R. and Patty, F. A.: Determination of sources of particulate atmospheric carbon, Science (80-.)., 122(3173), 751–753, 1955.

Collaud Coen, M., Weingartner, E., Apituley, a., Ceburnis, D., Fierz-Schmidhauser, R., Flentje, H., Henzing, J. S., Jennings, S. G., Moerman, M., Petzold, a., Schmid, O. and Baltensperger, U.: Minimizing light absorption measurement artifacts of the Aethalometer: evaluation of five correction algorithms, Atmos. Meas. Tech., 3(2), 457–474, doi:10.5194/amt-3-457-2010, 2010.

Crilley, L. R., Bloss, W. J., Yin, J., Beddows, D. C. S., Harrison, R. M., Allan, J. D., Young, D.

E., Flynn, M., Williams, P., Zotter, P., H. Prevot, a. S., Heal, M. R., Barlow, J. F., Halios, C. H., Lee, J. D., Szidat, S. and Mohr, C.: Sources and contributions of wood smoke during winter in London: assessing local and regional influences, Atmos. Chem. Phys. Discuss., 14(19), 27459–27530, doi:10.5194/acpd-14-27459-2014, 2014.

Currie, L. A.: EVOLUTION AND MULTIDISCIPLINARY FRONTIERS OF C-14 AEROSOL SCIENCE, Radiocarbon, 42(1), 115–126, 2000.

Currie, L. A., Eglinton, T. I., Benner, B. A. and Pearson, A.: Radiocarbon " ' dating ' " of individual chemical compounds in atmospheric aerosol : First results comparing direct isotopic and multivariate statistical apportionment of specific polycyclic aromatic hydrocarbons, Nucl. Instruments Methods Phys. Res., 123, 475–486, 1997.

Day, D. E., Hand, J. L., Carrico, C. M., Engling, G. and Malm, W. C.: Humidification factors from laboratory studies of fresh smoke from biomass fuels, J. Geophys. Res. Atmos., 111(D22), doi:10.1029/2006JD007221, 2006.

Dickerson, R. R., Andreae, M. O., Campos, T., Mayol-Bracero, O. L., Neususess, C. and Streets, D. G.: Analysis of black carbon and carbon monoxide observed over the Indian Ocean: Implications for emissions and photochemistry, J. Geophys. Res. Atmos., 107(D19), doi:10.1029/2001JD000501, 2002.

Dockery, D. W. and Pope, C. A.: Acute respiratory effects of particulate air pollution, Annu. Rev. Public Health, 15, 107–132, 1994.

Draxler, R. R. and Taylor, A. D.: Horizontal Dispersion Parameters for Long-Range Transport Modeling, J. Appl. Meteorol., 21(3), 367–372, 1982.

Drinovec, L., Močnik, G., Zotter, P., Prévôt, a. S. H., Ruckstuhl, C., Coz, E., Rupakheti, M., Sciare, J., Müller, T., Wiedensohler, a. and Hansen, a. D. a.: The "dual-spot" Aethalometer: an improved measurement of aerosol black carbon with real-time loading compensation, Atmos. Meas. Tech., 8(5), 1965–1979, doi:10.5194/amt-8-1965-2015, 2015.

Dusek, U., Frank, G. P., Hildebrandt, L., Curtius, J., Schneider, J., Walter, S., Chand, D., Drewnick, F., Hings, S. and Jung, D.: Size matters more than chemistry for cloud-nucleating ability of aerosol particles, Science (80-.)., 312(5778), 1375–1378, 2006.

Dusek, U., Frank, G. P., Curtius, J., Drewnick, F., Schneider, J., Kurten, A., Rose, D., Andreae,

M. O., Borrmann, S. and Poschl, U.: Enhanced organic mass fraction and decreased hygroscopicity of cloud condensation nuclei (CCN) during new particle formation events, Geophys. Res. Lett., 37(L03804), 1–5, doi:10.1029/2009GL040930, 2010.

Ebert, M., Weinbruch, S., Hoffmann, P. and Ortner, H. M.: Chemical characterization of North Sea Aerosol Particles, J. Aerosol Sci., 31(5), 613–632, 2000.

Engler, C., Birmili, W., Spindler, G. and Wiedensohler, A.: Analysis of exceedances in the daily PM10 mass concentration (50 ug m-3) at a roadside station in Leipzig, Germany, Atmos. Chem. Phys., 12(21), 10107–10123, doi:10.5194/acp-12-10107-2012, 2012.

Escudero, M., Querol, X., Avila, A. and Cuevas, E.: Origin of the exceedances of the European daily PM limit value in regional background areas of Spain, Atmos. Environ., 41(4), 730–744, doi:10.1016/j.atmosenv.2006.09.014, 2007.

Favez, O., El Haddad, I., Piot, C., Boréave, a., Abidi, E., Marchand, N., Jaffrezo, J.-L., Besombes, J.-L., Personnaz, M.-B., Sciare, J., Wortham, H., George, C. and D'Anna, B.: Inter-comparison of source apportionment models for the estimation of wood burning aerosols during wintertime in an Alpine city (Grenoble, France), Atmos. Chem. Phys., 10(12), 5295–5314, doi:10.5194/acp-10-5295-2010, 2010.

Finlayson-Pitts, B. J. and Pitts Jr., J. N.: Chemistry of the Upper and Lower Atmosphere, Academic Press., 2000.

Fleming, Z. L., Monks, P. S. and Manning, A. J.: Review: Untangling the influence of air-mass history in interpreting observed atmospheric composition, Atmos. Res., 104, 1–39, doi:10.1016/j.atmosres.2011.09.009, 2012.

Friedlander, S. K.: Smoke,Dust, and Haze-Fundamentals of Aerosol Dynamics, Second., Oxford University Press., 2000.

Gadhavi, H. and Jayaraman, a.: Absorbing aerosols: Contribution of biomass burning and implications for radiative forcing, Ann. Geophys., 28(1), 103–111, doi:10.5194/angeo-28-103-2010, 2010.

Garg, S., Chandra, B. P., Sinha, V., Sarda-Esteve, R., Gros, V. and Sinha, B.: Limitation of the Use of the Absorption Angstrom Exponent for Source Apportionment of Equivalent Black Carbon: a Case Study from the North West Indo-Gangetic Plain, Environ. Sci. Technol., 50(2), 814–824,

doi:10.1021/acs.est.5b03868, 2016.

Gauderman, W. J., Avol, E., Gillilard, F., Vora, H., Thomas, D., Berhane, K., McConnell, R., Kuenzli, N., Lurmann, F., Rappaport, E., Margolis, H., Bates, D. and Peters, J.: The Effect of Air Pollution on Lung Development from 10 to 18 Years of Age, N. Engl. J. Med., 351(11), 1057–1067, 2004.

Geiser, M., Rothen-rutishauser, B., Kapp, N., Schürch, S., Kreyling, W., Schulz, H., Semmler, M., Hof, V. I., Heyder, J. and Gehr, P.: Ultrafine Particles Cross Cellular Membranes by Nonphagocytic Mechanisms in Lungs and in Cultured Cells, Environ. Health Perspect., 113(11), 1555–1560, doi:10.1289/ehp.8006, 2005.

Gelencser, A., May, B., Simpson, D., Sanchez- Ochoa, A., Kasper-giebl, A., Puxbaum, H., Caseiro, A., Pio, C. and Legrand, M.: Source apportionment of PM2 . 5 organic aerosol over Europe : Primary/secondary , natural/anthropogenic , and fossil/biogenic origin, J. Geophys. Res., 112, 1–12, doi:10.1029/2006JD008094, 2007.

Gemmer, M. and Bo, X.: Air Quality Legislation and Standards in the European Union : Background , Status and Public Participation, Adv. Clim. Chang. Res., 4(1), 50–59, doi:10.3724/SP.J.1248.2013.050, 2013.

de Gouw, J. a, Warneke, C., Parrish, D. D., Holloway, J. S., Trainer, M. and Fehsenfeld, F. C.: Emission sources and ocean uptake of acetonitrile (CH3CN) in the atmosphere, J. Geophys. Res. Atmos., 108(D11), doi:10.1029/2002jd002897, 2003.

de Gouw, J. and Warneke, C.: Measurements of volatile organic compounds in the Earth's atmosphere using Proton- Transfer- Reaction mass spectrometry, Mass Spectrom. Rev., 26(2), 223–257, doi:10.1002/mas, 2007.

Grahame, T. J. and Schelsinger, R. B.: Health Effects of Airborne Particulate Matter: Do We Know Enough to Consider Regulating Specific Particle Types or Sources?, Inhal. Toxicol., 19(6–7), 457–481 [online] Available from: http://informahealthcare.com/doi/abs/10.1080/08958370701382220, 2007.

Guerreiro, C. B. B., Foltescu, V. and Leeuw, F. De: Air quality status and trends in Europe, Atmos. Environ., 98, 376–384, doi:10.1016/j.atmosenv.2014.09.017, 2014.

Gunthe, S. S., King, S. M., Rose, D., Chen, Q., Roldin, P., Farmer, D. K., Jimenez, J. L., Artaxo,

P. and Andreae, M. O.: Cloud condensation nuclei in pristine tropical rainforest air of Amazonia : size-resolved measurements and modeling of atmospheric aerosol composition and CCN activity, Atmos. Chem. Phys., 9, 7551–7575, 2009.

Gustafsson, O., Kruså, M., Zencak, Z., Sheesley, R. J., Granat, L., Engström, E., Praveen, P. S., Rao, P. S. P., Leck, C. and Rodhe, H.: Brown clouds over South Asia: biomass or fossil fuel combustion?, Science (80-.)., 323(5913), 495–498, doi:10.1126/science.1164857, 2009.

Hand, J. L., Malm, W. C., Laskin, A., Day, D., Lee, T., Wang, C., Carrico, C., Carrillo, J., Cowin, J. P., Collett, J. and Iedema, M. J.: Optical, physical, and chemical properties of tar balls observed during the Yosemite Aerosol Characterization Study, J. Geophys. Res. Atmos., 110(D21), doi:10.1029/2004JD005728, 2005.

Harris, E., Sinha, B., Pinxteren, D. van, Tilgner, A., Fomba, K. W., Schneider, J., Roth, A., Gnauk, T., Fahlbusch, B., Mertes, S., Lee, T., Collett, J., Foley, S., Borrmann, S., Hoppe, P. and Hermann, H.: Enhanced Role of Transition Metal Ion Catalysis During In-Cloud Oxidation of SO2, Science (80-.)., 340, 727–730, doi:10.1126/science.1230911, 2013.

Harrison, R. M., Smith, D. and Luhana, L.: Source Apportionment of Atmospheric Polycyclic Aromatic Hydrocarbons Collected from an Urban Location in Birmingham, U.K., Environ. Sci. Technol., 30(3), 825–832, 1996.

Hart, M., de Dear, R. and Hyde, R.: A synoptic climatology of tropospheric ozone episodes in Sydney, Australia, Int. J. Climatol., 26(12), 1635–1649, doi:10.1002/joc.1332, 2006.

Henning, S., Dieckmann, K., Ignatius, K., Schäfer, M., Zedler, P., Harris, E., Sinha, B., Pinxteren, D. Van, Mertes, S., Birmili, W., Merkel, M., Wu, Z., Wiedensohler, A., Wex, H., Herrmann, H. and Stratmann, F.: Influence of cloud processing on CCN activation behaviour in the Thuringian Forest , Germany during HCCT-2010, Atmos. Chem. Phys., 14, 7859–7868, doi:10.5194/acp-14-7859-2014, 2014.

Henry, R. C. and Christensen, E. R.: Selecting an Appropriate Multivariate Source Apportionment Model Result, Environ. Sci. Technol., 44(7), 2474–2481, 2010.

Herich, H., Hueglin, C. and Buchmann, B.: A 2.5 year's source apportionment study of black carbon from wood burning and fossil fuel combustion at urban and rural sites in Switzerland, Atmos. Meas. Tech., 4(7), 1409–1420, doi:10.5194/amt-4-1409-2011, 2011.

Herich, H., Gianini, M. F. D., Piot, C., Močnik, G., Jaffrezo, J. L., Besombes, J. L., PrévÔt, a. S. H. and Hueglin, C.: Overview of the impact of wood burning emissions on carbonaceous aerosols and PM in large parts of the Alpine region, Atmos. Environ., 89, 64–75, doi:10.1016/j.atmosenv.2014.02.008, 2014.

Hess, N. P. and Brezowsky, H.: Katalog der Großwetterlagen Europas (1881-1998)., 1999.

HLUG: Archive data repository of Hessiches Landesamt für Naturschuzt, Umwelt and Geologie, Hessiches Landesamt für Naturschuzt, Umwelt Geol., 2016.

Hodzic, A., Jimenez, J. L., Prévôt, a. S. H., Szidat, S., Fast, J. D. and Madronich, S.: Can 3-D models explain the observed fractions of fossil and non-fossil carbon in and near Mexico City?, Atmos. Chem. Phys., 10(22), 10997–11016, doi:10.5194/acp-10-10997-2010, 2010.

Hoffer, A., Gelencs, A., Guyon, P., Kiss, G., Schmid, O., Frank, G. P., Artaxo, P. and Andreae, M. O.: Optical properties of humic-like substances (HULIS) in biomass-burning aerosols, Atmos. Chem. Phys., 6(11), 3563–3570, 2006.

Holzinger, R., Warneke, C., Hansel, A., Jordan, A., Lindinger, W., Scharffe, D. H., Schade, G. and Crutzen, P. J.: Biomass burning as a source of formaldehyde, acetaldehyde, methanol, acetone, acetonitrile, and hydrogen cyanide, Geophys. Res. Lett., 26(8), 1161–1164, doi:10.1029/1999GL900156, 1999.

Holzinger, R., Jordan, A., Hansel, A. and Lindinger, W.: Automobile emissions of acetonitrile: Assessment of its contribution to the global source, J. Atmos. Chem., 38(2), 187–193, 2001.

Hoppel, W. A., Fitzgerald, J. W., Frick, G. M., Larson, R. E. and Mack, E. J.: Aerosol Size Distributions and Properties Found in the Marine Boundary Layer Over the Atlantic Ocean, Washington, DC., 1989.

Hoppel, W. A., Frick, G. M. and Fitzgerald, J. W.: Marine boundary layer measurements of new particle formation and the effects nonprecipitating clouds have on aerosol size distribution, J. Geophys. Res., 99, 14443–14459, 1994.

Horalek, J., Smet, P. De, Corbet, L., Kurfurst, P., Leeuw, F. De and Benesova, N.: European air quality maps of PM and ozone for 2013 and their uncertainty, ETC/ACM Tech. Pap. 2015/5, (March), 1–75 [online] Available from: http://acm.eionet.europa.eu/reports/ETCACM_TP_2015_5_AQMaps2013, 2016.

Hsu, Y., Holsen, T. M. and Hopke, P. K.: Comparison of hybrid receptor models to locate PCB sources in Chicago, Atmos. Environ., 37(4), 545–562, 2003.

Jacob, D. J.: Introduction to Atmospheric Chemistry and Physics, Princeton University Press., 1999.

Jacobson, M. Z.: Strong radiative heating due to the mixing state of black carbon in atmospheric aerosols, Nature, 409, 695–697, 2001.

Jacobson, M. Z.: Investigating cloud absorption effects: Global absorption properties of black carbon, tar balls, and soil dust in clouds and aerosols, J. Geophys. Res. Atmos., 117(6), 1–25, doi:10.1029/2011JD017218, 2012.

Janssen, N. A. H., Hoek, G., Simic-lawson, M., Fischer, P., Bree, L. Van, Brink, H., Keuken, M., Atkinson, R. W., Anderson, H. R., Brunekreef, B. and Cassee, F. R.: Review Black Carbon as an Additional Indicator of the Adverse Health Effects of Airborne Particles Compared with PM 10 and PM 2.5, Environ. Health Perspect., 119(12), 1691–1699, 2011.

Jolliffe, I. T.: Principal Component Analysis, Second., John Wiley and Sons, Ltd., 2002.

Jost, C., Trentmann, J., Sprung, D. and Andreae, M. O.: Trace gas chemistry in a young biomass burning plume over Namibia: Observations and model simulations, J. Geophys. Res. Atmos., 108(D13), doi:10.1029/2002JD002431, 2003.

Junninen, H., Pullinen, I., Springer, M., Rubach, F., Tillmann, R., Lee, B., Lopez-hilfiker, F., Andres, S., Acir, I., Rissanen, M., Wahner, A., Kerminen, V., Kulmala, M., Worsnop, D. R. and Mentel, T. F.: A large source of low-volatility secondary organic aerosol, Nature, 506, 476–479, doi:10.1038/nature13032, 2014.

Keeler, G. J. and Samson, P. J.: Spatial Representativeness of Trace Element Ratios, Environ. Sci. Technol., 23(11), 1358–1364, doi:10.1021/es00069a005, 1989.

Kirchstetter, T. W., Novakov, T. and Hobbs, P. V.: Evidence that the spectral dependence of light absorption by aerosols is affected by organic carbon, J. Geophys. Res. Atmos., 109(D21), doi:10.1029/2004JD004999, 2004.

Koch, D., Schulz, M., Kinne, S., McNaughton, C., Spackman, J. R., Balkanski, Y., Bauer, S., Berntsen, T., Bond, T. C., Boucher, O., Chin, M., Clarke, A., De Luca, N., Dentener, F., Diehl, T.,

Dubovik, O., Easter, R., Fahey, D. W., Feichter, J., Fillmore, D., Freitag, S., Ghan, S., Ginoux, P., Gong, S., Horowitz, L., Iversen, T., Kirkevåg, A., Klimont, Z., Kondo, Y., Krol, M., Liu, X., Miller, R., Montanaro, V., Moteki, N., Myhre, G., Penner, J. E., Perlwitz, J., Pitari, G., Reddy, S., Sahu, L., Sakamoto, H., Schuster, G., Schwarz, J. P., Seland, Ø., Stier, P., Takegawa, N., Takemura, T., Textor, C., van Aardenne, J. a. and Zhao, Y.: Evaluation of black carbon estimations in global aerosol models, Atmos. Chem. Phys., 9(22), 9001–9026, doi:10.5194/acp-9-9001-2009, 2009.

Kondratyev, K. Y., Ivlev, L. S., Krapivin, V. F. and Varotsos, C. A.: Atmospheric Aerosol Prooperties: Formation, Processes and Impacts, Praxis Publishing Ltd., 2006.

Kourtidis, K. a., Ziomas, I., Zerefos, C., Kosmidis, E., Symeonidis, P., Christophilopoulos, E., Karathanassis, S. and Mploutsos, A.: Benzene, toluene, ozone, NO2 and SO2 measurements in an urban street canyon in Thessaloniki, Greece, Atmos. Environ., 36(34), 5355–5364, doi:10.1016/S1352-2310(02)00580-0, 2002.

Kristensson, A., Johansson, C., Westerholm, R., Swietlicki, E., Gidhagen, L., Wideqvist, U. and Vesely, V.: Real-world traffic emission factors of gases and particles measured in a road tunnel in Stockholm, Sweden, Atmos. Environ., 38(5), 657–673, doi:10.1016/j.atmosenv.2003.10.030, 2004.

Kulkarni, P., Baron, P. A. and Willeke, K., Eds.: Aerosol measurement: Principles, Techniques, and Applications, Third., A John Wiley and Sons Inc Publication., 2011.

Lack, D. A., Bahreni, R., Langridge, J. M., Gilman, J. B. and Middlebrook, A. M.: Brown carbon absorption linked to organic mass tracers in biomass burning particles, Atmos. Chem. Phys., 13, 2415–2422, doi:10.5194/acp-13-2415-2013, 2013.

Laskin, A., Laskin, J. and Nizkorodov, S. A.: Chemistry of Atmospheric Brown Carbon, Chem. Rev., 115(10), 4335–4382, 2015.

Lee, S. and Ashbaugh, L.: Comparison of multi-receptor and single-receptor trajectory source apportionment (TSA) methods using artificial sources, Atmos. Environ., 41(6), 1119–1127, doi:10.1016/j.atmosenv.2006.10.019, 2007.

Lenschow, P., Abraham, H.-J., Kutzner, K., Lutz, M., Preuss, J.-D. and Reichenbacher, W.: Some ideas about the sources of PM10, Atmos. Environ., 35(1), 23–33, doi:10.1016/S1352-2310(01)00122-4, 2001.

Lewis, C. W., Klouda, G. A. and Ellenson, W. D.: Radiocarbon measurement of the biogenic contribution to summertime PM-2 . 5 ambient aerosol in Nashville , TN, Atmos. Environ., 38, 6053–6061, doi:10.1016/j.atmosenv.2004.06.011, 2004.

Lewis, K., Arnott, W. P., Moosmüller, H. and Wold, C. E.: Strong spectral variation of biomass smoke light absorption and single scattering albedo observed with a novel dual-wavelength photoacoustic instrument, J. Geophys. Res. Atmos., 113(D16), doi:10.1029/2007JD009699, 2008.

Li, M., Huang, X., Zhu, L., Li, J., Song, Y., Cai, X. and Xie, S.: Analysis of the transport pathways and potential sources of PM10 in Shanghai based on three methods, Sci. Total Environ., 414, 525–534, doi:10.1016/j.scitotenv.2011.10.054, 2012.

Libby, W. F.: History of Radiocarbon Dating, in Radioactive dating and methods of low level counting, pp. 3–25., 1967.

Luderer, G., Trentmann, J., Winterrath, T., Textor, C., Herzog, M., Graf, H. F. and Andreae, M. O.: Modeling of biomass smoke injection into the lower stratosphere by a large forest fire (Part II): sensitivity studies, Atmos. Chem. Phys., 6, 5261–5277, 2006.

Mao, Y. H., Li, Q. B., Chen, D., Zhang, L., Hao, W.-M. and Liou, K.-N.: Top-down estimates of biomass burning emissions of black carbon in the Western United States, Atmos. Chem. Phys., 14(14), 7195–7211, doi:10.5194/acp-14-7195-2014, 2014.

Martinsson, J., Eriksson, A. C., Nielson, I. E., Malmborg, V. B., Ahlberg, E., Andersen, C., Lindgren, R., Nystrom, R., Nordin, E. Z., Brune, W. H., Svenningsson, B., Swierlicki, E., Boman, C. and Pagels, J.: Impacts of combustion conditions and photchemical processing on the light absorption of biomass combustion aerosol, Environ. Sci. Technol. Just Accept. Manuscr., doi:10.1021/acs.est.5b03205, 2015.

Masiol, M., Rampazzo, G., Ceccato, D., Squizzato, S. and Pavoni, B.: Characterization of PM10 sources in a coastal area near Venice (Italy): An application of factor-cluster analysis, Chemosphere, 80(7), 771–778, doi:10.1016/j.chemosphere.2010.05.008, 2010.

Matthias-maser, S., Bogs, B. and Jaenicke, R.: The size distribution of primary biological aerosol particles in cloud water on the mountain Kleiner Feldberg / Taunus (FRG), Atmos. Res., 54, 1–13, doi:10.1016/S0169-8095(00)00039-9, 2000.

Maykut, N. N., Orchard, P., Kim, E. and Larson, T. V: Source Apportionment of PM2.5 at an

Urban IMPROVE Site in Seattle, Washington, Environ. Sci. Technol., 37(22), 5135–5142, 2003.

Menon, S., Hansen, J., Nazarenko, L. and Luo, Y.: Climate effects of black carbon aerosols in China and India, Science (80-.)., 297(5590), 2250–2253, doi:10.1126/science.1075159, 2002.

Moise, T., Flores, J. M. and Rudich, Y.: Optical Properties of Secondary Organic Aerosols and Their Changes by Chemical Processes, Chem. Rev., 115, 4400–4439, doi:10.1021/cr5005259, 2015.

Moosmüller, H., Chakrabarty, R. K. and Arnott, W. P.: Aerosol light absorption and its measurement: A review, J. Quant. Spectrosc. Radiat. Transf., 110(11), 844–878, doi:10.1016/j.jqsrt.2009.02.035, 2009.

Moosmüller, H., Chakrabarty, R. K., Ehlers, K. M. and Arnott, W. P.: Absorption Ångström coefficient, brown carbon, and aerosols: basic concepts, bulk matter, and spherical particles, Atmos. Chem. Phys., 11(3), 1217–1225, doi:10.5194/acp-11-1217-2011, 2011.

Nandy, B., Sharma, G., Garg, S., Kumari, S., George, T., Sunanda, Y. and Sinha, B.: Recovery of consumer waste in India – A mass flow analysis for paper, plastic and glass and the contribution of households and the informal sector, Resour. Conserv. Recycl., 101, 167–181, doi:10.1016/j.resconrec.2015.05.012, 2015.

Nemmar, A., Hoet, P. H. M., Vanquickenborne, B., Dinsdale, D., Thomeer, M., Hoylaerts, M. F., Vanbilloen, H., Mortelmans, L. and Nemery, B.: Passage of Inhaled Particles Into the Blood Circulation in Humans, Circulation, 105, 411–414, doi:10.1161/hc0402.104118, 2002.

Paatero, P. and Tapper, U.: Positive matrix factorizaion: A non-negative factor model with optimal utilization of error estimates of data values, Environmetrics, 5(111–126), doi:10.1002/env.3170050203, 1994.

Pawar, H., Garg, S., Kumar, V., Sachan, H., Arya, R., Sarkar, C., Chandra, B. P. and Sinha, B.: Quantifying the contribution of long-range transport to particulate matter (PM) mass loadings at a suburban site in the north-western Indo-Gangetic Plain (NW-IGP), Atmos. Chem. Phys., 15(16), 9501–9520, doi:10.5194/acp-15-9501-2015, 2015.

Penner, J. E., Andreae, M., Annegarn, H., Barrie, L., Feichter, J., Hegg, D., Jayaraman, A., Leaitch, R., Murphy, D., Nganga, J. and Pitari, G.: Aerosols, their Direct and Indirect Effects, in IPCC Third Assessment Report on Climate Change, edited by B. Nyenzi and J. Prospero., 2001.

Peters, A., Liu, E., Verrier, R. L., Schwartz, J., Gold, D. R., Mittleman, M., Baliff, J., Oh, J. A., Allen, G., Monahan, K. and Dockery, D. W.: Air Pollution and Incidence of Cardiac Arrhythmia, Epidemiology, 11(1), 11–17, 2000.

Petzold, A., Ogren, J. A., Fiebig, M., Laj, P., Li, S.-M., Baltensperger, U., Holzer-Popp, T., Kinne, S., Pappalardo, G., Sugimoto, N., Wehrli, C., Wiedensohler, A. and Zhang, X.-Y.: Recommendations for reporting " black carbon " measurements, Atmos. Chem. Phys., 13(16), 8365–8379, doi:10.5194/acp-13-8365-2013, 2013.

Pinxteren, D. van, Brüggemann, E., Gnauk, T., Muller, K., Thiel, C. and Herrmann, H.: A GIS based approach to back trajectory analysis for the source apportionment of aerosol constituents and its first application, J. Atmos. Chem., 67(1), 1–28, doi:10.1007/s10874-011-9199-9, 2010.

Pinxteren, D. Van, Fomba, K. W., Spindler, G., Muller, K., Poulain, L., Iinuma, Y., Loschau, G., Hausmann, A. and Herrmann, H.: Regional air quality in Leipzig , Germany: Detailed source apportionment of size-resolved aerosol particles and comparison with the year 2000, Faraday Discuss., 189, 291–315, doi:10.1039/C5FD00228A, 2016.

Planchon, O., Quenol, H., Dupont, N. and Corgne, S.: Application of the Hess-Brezowsky classification to the identification of weather patterns causing heavy winter rainfall in Brittany (France), Nat. Hazards Earth Syst. Sci, 9, 1161–1173, doi:10.5194/nhess-9-1161-2009, 2009.

Pöhlker, C., Wiedemann, K. T., Sinha, B., Shiraiwa, M., Gunthe, S. S., Smith, M., Su, H., Artaxo, P., Chen, Q., Elbert, W., Gilles, M. K., Kilcoyne, A. L. D., Moffet, R. C., Weigand, M., Martin, S. T., Pöschl, U. and Andreae, M. O.: Biogenic Potassium Salt Particles as Seeds for Secondary Organic Aeorsol in the Amazon, Science (80-.)., 337, 1075, doi:10.1126/science.1123264, 2012.

Poirot, R. L., Wishinski, P. R., Hopke, P. K. and Polissar, A. V.: Comparative Application of Multiple Receptor Methods To Identify Aerosol Sources in Northern Vermont, Environ. Sci. Technol., 35(23), 4622–4636, 2001.

Pope, C. A., Ezzati, M. and Dockery, D. W.: Fine-Particulate Air Pollution and Life Expectancy in the United States, N. Engl. J. Med., 360(4), 376–386, 2009.

Pöschl, U., Martin, S. T., Sinha, B., Chen, Q., Gunthe, S. S., Huffman, J. A., Borrmann, S., Farmer, D. K., Garland, R. M., Helas, G., Jimenez, J. L., King, S. M., Manzi, A., Mikhailov, E., Pauliquevus, T., Petter, M. D., Prenni, A. J., Roldin, R., Rose, D., Schneider, J., Su, H., Zorn, S. R., Artaxo, P. and Andreae, M. O.: Rainforest Aerosols as Biogenic Nuclei of Cloud and

Precipitation in the Amazon, Science (80-.)., 329, 1513–1516, doi:10.1126/science.1191056, 2010.

Pósfai, M. and Buseck, P. R.: Nature and Climate Effects of Individual Tropospheric Aerosol Particles, Annu. Rev. Earth Planet. Sci., 38(1), 17–43, doi:10.1146/annurev.earth.031208.100032, 2010.

Pósfai, M., Simonics, R., Li, J., Hobbs, P. V. and Buseck, P. R.: Individual aerosol particles from biomass burning in southern Africa: 1. Compositions and size distributions of carbonaceous particles, J. Geophys. Res. Atmos., 108(D13), doi:10.1029/2002JD002291, 2003.

Querol, X., Alastuey, A., Ruiz, C. R., Artin, B., Hansson, H. C., Straehl, P. and Schneider, J.: Speciation and origin of PM10 and PM2 . 5 in selected European cities, Atmos. Environ., 38, 6547–6555, doi:10.1016/j.atmosenv.2004.08.037, 2004.

Quinn, P. K., Bates, T. S., Baum, E., Doubleday, N., Fiore, A. M., Flanner, M., Fridlind, A., Garrett, T. J., Koch, D., Menon, S., Shindell, D., Stohl, A. and Warren, S. G.: Short-lived pollutants in the Arctic : their climate impact and possible mitigation strategies, Atmos. Chem. Phys., 8(6), 1723–1735, 2008.

Raaschou-nielsen, O., Beelen, R., Wang, M., Hoek, G., Andersen, Z. J., Hoffmann, B., Stafoggia, M., Samoli, E., Weinmayr, G., Dimakopoulou, K., Nieuwenhuijsen, M., Xun, W. W., Fischer, P., Eriksen, K. T., Pedersen, N., Östenson, C., Pershagen, G., Fratiglioni, L., Concin, H., Nagel, G., Jaensch, A., Ineichen, A., Naccarati, A., Katsoulis, M., Trichpoulou, A., Keuken, M., Jedynska, A., Kooter, I. M., Kukkonen, J., Brunekreef, B., Sokhi, R. S., Katsouyanni, K. and Vineis, P.: Particulate matter air pollution components and risk for lung cancer, Environ. Int., 87, 66–73, doi:10.1016/j.envint.2015.11.007, 2016.

Ramanathan, V. and Ramana, M. V.: Persistent, Widespread, and Strongly Absorbing Haze Over the Himalayan Foothills and the Indo-Gangetic Plains, Pure Appl. Geophys., 162(8–9), 1609–1626, 2005.

Ramanathan, V., Crutzen, P. J., Kiehl, J. T. and Rosenfeld, D.: Aerosols, Climate, and the Hydrological Cycle, Science (80-.)., 294(5549), 2119–2124, doi:10.1126/science.1064034, 2001.

Randel, W. J., Park, M., Emmons, L., Kinnison, D., Bernath, P., Walker, K., Boone, C. and Pumphrey, H.: Asian monsoon transport of pollution to the stratosphere, Science (80-.)., 328(5978), 611–613, doi:10.1126/science.1182274, 2010.

Reddy, M. S. and Venkataraman, C.: Inventory of aerosol and sulphur dioxide emissions from India: I—Fossil fuel combustion, Atmos. Environ., 36(4), 677–697, doi:10.1016/S1352-2310(01)00463-0, 2002a.

Reddy, M. S. and Venkataraman, C.: Inventory of aerosol and sulphur dioxide emissions from India. Part II—biomass combustion, Atmos. Environ., 36(4), 699–712, doi:10.1016/S1352-2310(01)00464-2, 2002b.

Rehman, I. H., Ahmed, T., Praveen, P. S., Kar, a. and Ramanathan, V.: Black carbon emissions from biomass and fossil fuels in rural India, Atmos. Chem. Phys., 11(14), 7289–7299, doi:10.5194/acp-11-7289-2011, 2011.

Reid, J. S., Eck, T. F., Christopher, S. a., Koppmann, R., Dubovik, O., Eleuterio, D. P., Holben, B. N., Reid, E. a. and Zhang, J.: A review of biomass burning emissions part III: intensive optical properties of biomass burning particles, Atmos. Chem. Phys., 5(3), 827–849, doi:10.5194/acpd-4-5201-2004, 2005.

Riuttanen, L., Hulkkonen, M., Dal Maso, M., Junninen, H. and Kulmala, M.: Trajectory analysis of atmospheric transport of fine particles, SO 2, NOx and O3 to the SMEAR II station in Finland in 1996-2008, Atmos. Chem. Phys., 13(4), 2153–2164, doi:10.5194/acp-13-2153-2013, 2013.

Roden, C. A. and Bond, T. C.: Emission Factors and Real-Time Optical Properties of Particles Emitted from Traditional Wood Burning Cookstoves, Environ. Sci. Technol., 40(21), 6750–6757, 2006.

Rodriguez, S., Querol, X., Alastuey, A., Kallos, G. and Kakaliagou, O.: Saharan dust contributions to PM10 and TSP levels in Southern and Eastern Spain, Atmos. Environ., 35(14), 2433–2447, doi:10.1016/S1352-2310(00)00496-9, 2001.

Rolph, G. D.: HYSPLIT4 User's Guide., 2013.

Rosen, H., Hansen, A. D. A., Gundel, L. and Novakov, T.: Identification of the graphitic carbon component of source and ambient particulates by Raman spectroscopy and an optical attenuation technique, in Carbonaceous Particles in the Atmosphere, pp. 229–232, Lawrence Berkeley Laboratory, Berkeley, CA., 1979.

Rosenfeld, D., Sherwood, S., Wood, R. and Donner, L.: Climate Effects of Aerosol- Cloud Interactions, Science (80-.)., 343, 379–380, doi:10.1126/science.1247490, 2014.

Russell, A. G. and Brunekereef, B.: A Focus on Particulate Matter and Health, Environ. Sci. Technol., 43(13), 4620–4625, 2009.

Salby, M. L.: Fundamentals of Atmospheric Physics, edited by R. Dmowska and J. R. Holton, Academic Press., 1995.

Salvador, P., Artinano, B., Querol, X. and Alastuey, A.: A combined analysis of backward trajectories and aerosol chemistry to characterise long-range transport episodes of particulate matter : The Madrid air basin , a case study, Sci. Total Environ., 390(2), 495–506, doi:10.1016/j.scitotenv.2007.10.052, 2008.

Salvador, P., Artinano, B., Pio, C., Afonso, J., Legrand, M., Puxbaum, H. and Hammer, S.: Evaluation of aerosol sources at European high altitude background sites with trajectory statistical methods, Atmos. Environ., 44(19), 2316–2329, doi:10.1016/j.atmosenv.2010.03.042, 2010.

Sandradewi, J., Prévôt, a. S. H., Weingartner, E., Schmidhauser, R., Gysel, M. and Baltensperger, U.: A study of wood burning and traffic aerosols in an Alpine valley using a multi-wavelength Aethalometer, Atmos. Environ., 42(1), 101–112, doi:10.1016/j.atmosenv.2007.09.034, 2008a.

Sandradewi, J., Prévôt, a. S. H., Alfarra, M. R., Szidat, S., Wehrli, M. N., Ruff, M., Weimer, S., Lanz, V. a., Weingartner, E., Perron, N., Caseiro, a., Kasper-Giebl, a., Puxbaum, H., Wacker, L. and Baltensperger, U.: Comparison of several wood smoke markers and source apportionment methods for wood burning particulate mass, Atmos. Chem. Phys. Discuss., 8(2), 8091–8118, doi:10.5194/acpd-8-8091-2008, 2008b.

Sandradewi, J., Prévôt, A. S. H., Szidat, S., Perron, N., Alfarra, M. R., Lanz, V. a, Weingartner, E. and Baltensperger, U.: Using aerosol light absorption measurements for the quantitative determination of wood burning and traffic emission contributions to particulate matter, Environ. Sci. Technol., 42(9), 3316–23 [online] Available from: http://www.ncbi.nlm.nih.gov/pubmed/18522112, 2008c.

Sarkar, C., Kumar, V. and Sinha, V.: Massive emissions of carcinogenic benzenoids from paddy residue burning in North India, Curr. Sci., 104, 1703–1709, 2013.

Schmid, O., Artaxo, P., Arnott, W. P., Chand, D., Gatti, L. V, Frank, G. P., Hoffer, A., Schnaiter, M. and Andreae, M. O.: Spectral light absorption by ambient aerosols influenced by biomass burning in the Amazon Basin . I : Comparison and field calibration of absorption measurement techniques, Atmos. Chem. Phys., 6(11), 3443–3462, 2006.

Seibert, P., Kromp-Kolb, H., Baltensperger, U., Jost, D. T., Schwikowski, M., Kasper, A. and Puxbaum, H.: Trajectory analysis of aerosol measurements at high alpine sites. In: Transport and Transformation of Pollutants in the Troposphere, . Academic Publishing, Den Haag., 1994.

Seinfeld, J. P. and Pandis, S. N.: Atmospheric Chemistry and Physics: From Air Pollution to Climate Change, Second., John Wiley and Sons, Inc., 2006.

Shindell, D. and Faluvegi, G.: Climate response to regional radiative forcing during the twentieth century, Nat. Geosci., 2(4), 294–300, doi:10.1038/ngeo473, 2009.

Simoneit, B. R. T.: Biomass burning - A review of organic tracers for smoke from incomplete combustion., 2002.

Sinha, V., Kumar, V. and Sarkar, C.: Chemical composition of pre-monsoon air in the Indo-Gangetic Plain measured using a new air quality facility and PTR-MS: high surface ozone and strong influence of biomass burning, Atmos. Chem. Phys., 14(12), 5921–5941, doi:10.5194/acp-14-5921-2014, 2014.

Solomon, S., Qin, D., Manning, M., Chen, Z., Marqui, M., Averyt, K. B., Tignor, M. and Miller, H. L., Eds.: Summary for Policymakers, in Climate Change 2007: The Physical Science Basis. Contribution of Working Group I to the Fourth Assessment Report of the Intergovernmental Panel on Climate Change, Cambridge University Press, Cambridge, United Kingdom and New york, NY, USA., 2007.

Song, Y., Dai, W., Shao, M., Liu, Y., Lu, S., Kuster, W. and Goldan, P.: Comparison of receptor models for source apportionment of volatile organic compounds in Beijing , China, Environ. Pollut., 156(1), 174–183, doi:10.1016/j.envpol.2007.12.014, 2008.

Spracklen, D. V, Carslaw, K. S., Kulmala, M., Kerminen, V., Sihto, S., Riipinen, I., Merikanto, J., Mann, G. W., Chipperfield, M. P., Wiedensohler, A., Birmili, W. and Lihavainen, H.: Contribution of particle formation to global cloud condensation nuclei concentrations, Geophys. Res. Lett., 35, 1–5, doi:10.1029/2007GL033038, 2008.

Stein, A. F., Draxler, R. R., Rolph, G. D., Stunder, B. J. B., Cohen, M. D. and Ngan, F.: NOAA's HYSPLIT atmospheric transport ad dispersion modeling system, Bull. Am. Meteorol. Soc., 96, 2059–2077, 2015.

Stocker, T. F., Qin, D., Plattner, G. K., Tignor, M., Allen, S. K., Boschung, J., Nauels, Y., Xia, Y.,

Bex, V. and Midgley, P. M.: IPCC,2013: Summary for Policymakers. In: Climate Change 2013: The Physical Science Basis. Contribution of Working Group I to the Fifth assessment Report of the Intergovernmental Panel on climate Change. [online] Available from: http://www.climatechange2013.org/images/report/WG1AR5_ALL_FINAL.pdf, 2013.

Stockwell, C. E., Veres, P. R., Williams, J. and Yokelson, R. J.: Characterization of biomass burning smoke from cooking fires, peat, crop residue and other fuels with high resolution proton-transfer-reaction time-of-flight mass spectrometry, Atmos. Chem. Phys. Discuss., 14(15), 22163–22216, doi:10.5194/acpd-14-22163-2014, 2014.

Stohl, A.: Trajectory Statistics- A new method to establish source-receptor relationships of air pollutants and its application to Particulate Sulfate in Europe, Atmos. Environ., 30(4), 579–587, 1996.

Stohl, A.: Computation, accuracy and applications of trajectories—A review and bibliography, Atmos. Environ., 32(6), 947–966, doi:10.1016/S1352-2310(97)00457-3, 1998.

Stohl, A.: Chapter 21 Computation, accuracy and applications of trajectories- a review and bibliography, Dev. Environ. Sci., 1(C), 615–654, doi:10.1016/S1474-8177(02)80024-9, 2002.

Strak, M., Janssen, N. A. H., Godri, K. J., Gosens, I., Mudway, ian S., Cassee, F. R., Lebret, E., Kelly, F. J., Harrison, R. M., Brunekreef, B., Steenhof, M. and Hoek, G.: Respiratory Health Effects of Airborne Particulate Matter: The Role of Particle Size, Composition, and Oxidative Potential—The RAPTES Project, Environ. Health Perspect., 120(8), 1183–1189, 2012.

Stull, R. B.: An Introduction to Boundary Layer Meteorology, 1988.

Tang, D., Wang, C., Nie, J., Chen, R., Niu, Q., Kan, H., Chen, B., Perera, F. and CDC, T.: Health benefits of improving air quality in Taiyuan, China, Environ. Int., 73, 235–242, doi:10.1016/j.envint.2014.07.016, 2014.

Tiwari, S., Pipal, a S., Srivastava, a K., Bisht, D. S. and Pandithurai, G.: Determination of wood burning and fossil fuel contribution of black carbon at Delhi, India using aerosol light absorption technique, Environ. Sci. Pollut. Res. Int., 22(4), 2846–2855, doi:10.1007/s11356-014-3531-2, 2014.

Tomlin, A. S., Smalley, R. J., Tate, J. E., Barlow, J. F., Belcher, S. E., Arnold, S. J., Dobre, A. and Robins, A.: A field study of factors influencing the concentrations of a traffic- related pollutant in

the vicinity of a complex urban junction, Atmos. Environ., 43(32), 5027–5037, doi:10.1016/j.atmosenv.2009.06.047, 2009.

Vasconcelos, L. A. de P., Kahl, J. D. W., Liu, D., Macias, E. S. and White, W. H.: Spatial resolution of a transport inversion technique, J. Geophys. Res., 101(D14), 19337–19342, doi:10.1029/96JD01659, 1996.

Venkataraman, C., Habib, G., Eiguren-Fernandez, A., Miguel, a H. and Friedlander, S. K.: Residential biofuels in South Asia: Carbonaceous aerosol emissions and climate impacts, Science (80-.)., 307(5714), 1454–1456, doi:10.1126/science.1104359, 2005.

Viana, M., Maenhaut, W., Chi, X., Querol, X. and Alastuey, A.: Comparative chemical mass closure of fine and coarse aerosols at two sites in south and west Europe: Implications for EU air pollution policies, Atmos. Environ., 41(2), 315–326, doi:10.1016/j.atmosenv.2006.08.010, 2007.

Virkkula, A., Mäkelä, T., Hillamo, R., Yli-tuomi, T., Hirsikko, A., Hämeri, K. and Koponen, I. K.: A Simple Procedure for Correcting Loading Effects of Aethalometer Data, J. air waste Manag. Assoc., 57(10), 1214–1222, doi:10.3155/1047-3289.57.10.1214, 2007.

Wallace, J. M. and Hobbs, P. V.: Atmospheric Science, Second., edited by R. Dmowska, D. Hartmen, and H. T. Rossby, Academic Press., 2006.

Warneke, C., Roberts, J. M., Veres, P., Gilman, J., Kuster, W. C., Burling, I., Yokelson, R. and de Gouw, J. a.: VOC identification and inter-comparison from laboratory biomass burning using PTR-MS and PIT-MS, Int. J. Mass Spectrom., 303(1), 6–14, doi:10.1016/j.ijms.2010.12.002, 2011.

Weber, R. J., Sullivan, A. P., Peltier, R. E., Russell, A., Yan, B., Zheng, M., Gouw, J. De, Warneke, C., Brock, C., Holloway, J. S., Atlas, E. L. and Edgerton, E.: A study of secondary organic aerosol formation in the anthropogenic-influenced southeastern United States, J. Geophys. Res., 112, 1–13, doi:10.1029/2007JD008408, 2007.

Weingartner, E., Saathoff, H., Schnaiter, M., Streit, N., Bitnar, B. and Baltensperger, U.: Absorption of light by soot particles: determination of the absorption coefficient by means of aethalometers, J. Aerosol Sci., 34(10), 1445–1463, doi:10.1016/S0021-8502(03)00359-8, 2003.

Westmoreland, E. J., Carslaw, N., Carslaw, D. C., Gillah, A. and Bates, E.: Analysis of air quality within a street canyon using statistical and dispersion modelling techniques, Atmos. Environ.,

41(39), 9195–9205, doi:10.1016/j.atmosenv.2007.07.057, 2007.

Wild, M.: Global dimming and brightening : A review, J. Geophys. Res., 114(March), 1–31, doi:10.1029/2008JD011470, 2009.

Wolff, H. and Perry, L.: Trends in Clean Air Legislation in Europe : Particulate Matter and Low Emission Zones 1, Reveiw Environ. Econ. Policy, 4(2), 293–308, doi:10.1093/reep/req008, 2010.

Xie, S., Zhang, J. and Ho, Y.-S.: Assessment of world aerosol research trends by bibliometric analysis, Scientometris, 77(1), 113–130, doi:10.1007/s11192-007-1928-0, 2008.

Yang, M., Howell, S. G., Zhuang, J. and Huebert, B. J.: Attribution of aerosol light absorption to black carbon, brown carbon, and dust in China - interpretations of atmospheric measurements during EAST-AIRE, Atmos. Chem. Phys., 9(6), 2035–2050, doi:10.5194/acpd-8-10913-2008, 2009.

Zauscher, M. D., Wang, Y., Moore, M. J. K., Gaston, C. J. and Prather, K. A.: Air Quality Impact and Physicochemical Aging of Biomass Burning Aerosols during the 2007 San Diego Wildfires, Environ. Sci. Technol., 47, 7633–7643, 2013.

Zeng, Y. and Hopke, P. K.: A study of the sources of acid precipitation in Ontario, Canada, Atmos. Environ., 23(7), 1499–1509, 1989.

ZIMEN 2016: Archive data repository of Rheinland-Pfalz Landesamt fur Umwelt, Landesamt für Umwelt Rheinland-Pfalz, http://www.luft-rlp.de/aktuell/stationswerte/pm10/index.php, 2016.